ISSN: 2153-1196 Vol. 5, No. 13, July 2014

Scientific Research

Journal of Modern Physics

Special Issue on Nondestructive Testing

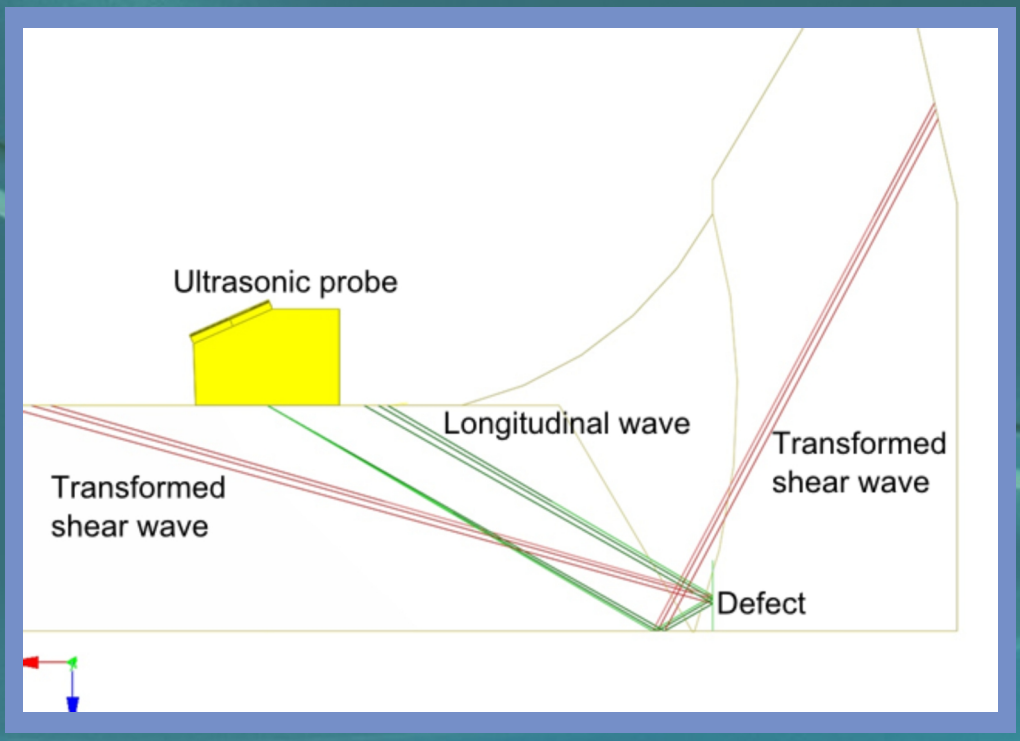

ISSN: 2153-1196
9 772153 119007 13

www.scirp.org/journal/jmp

Journal Editorial Board

ISSN: 2153-1196 (Print) ISSN: 2153-120X (Online)
http://www.scirp.org/journal/jmp

Journal of Modern Physics, 2014, 5, 1167-1222
Published Online July 2014 in SciRes. http://www.scirp.org/journal/jmp

Table of Contents

Volume 5 Number 13 July 2014

The figure on the front cover is from the article published in Journal of Modern Physics, 2014, Vol. 5, No. 13, pp. 1167-1172 by Pavel Mares.

Journal of Modern Physics (JMP)

Journal Information

SUBSCRIPTIONS

The *Journal of Modern Physics* (Online at Scientific Research Publishing, www.SciRP.org) is published monthly by Scientific Research Publishing, Inc., USA.

Subscription rates:

Print: $89 per issue.
To subscribe, please contact Journals Subscriptions Department, E-mail: sub@scirp.org

SERVICES

Advertisements
Advertisement Sales Department, E-mail: service@scirp.org

Reprints (minimum quantity 100 copies)
Reprints Co-ordinator, Scientific Research Publishing, Inc., USA.
E-mail: sub@scirp.org

COPYRIGHT

PRODUCTION INFORMATION

For manuscripts that have been accepted for publication, please contact:
E-mail: jmp@scirp.org

Journal of Modern Physics, 2014, 5, 1167-1172
Published Online July 2014 in SciRes. http://www.scirp.org/journal/jmp
http://dx.doi.org/10.4236/jmp.2014.513118

Scientific Research

Simulation as a Support for Ultrasonic Testing

Pavel Mares

Structural and System Diagnostics, Research Centre Rez Ltd., Husinec-Rez, Czech Republic
Email: Pavel.Mares@cvrez.cz

Received 6 May 2014; revised 2 June 2014; accepted 27 June 2014

Abstract

Ultrasonic testing is a very important non-destructive method for testing components for safety of nuclear power plants and other security and delicate parts in other industries. Nowadays, thanks to the development of computer technology, it is possible to simulate processes which occur during ultrasonic testing. That is why numerical simulations are becoming an integral part of non-destructive testing. Simulations are used to determine parameters of ultrasonic examination, especially parameters of probes and scan plan and also in the analysis of results. They are used in such cases, when it is necessary to verify applicability of probes and methods. This verification could be provided on the weld and test block which are not manufactured. It could be also provided on defects, which are not manufactured in test block, but their presence is possible in given weld joint. Simulations are very useful for verifying the propagation of ultrasonic signal in given area (e.g. weld area). If movement of probe is limited, possibility of whole volume scan should be verified.

Keywords

Non-Destructive Testing, Ultrasonic, Simulation, Phased Array

1. Introduction

Modeling and simulation of ultrasonic non-destructive testing is utilized in ever-increasing number of industrial NDT including nuclear power plants. The application is beneficial in various fields, such as evaluation and analysis of recorded data, modeling of ultrasonic inspection process, proposals of geometry of probes, proposals of inspection procedures and more [1].

Goal of this paper is to describe main advantages of ultrasonic simulation software and its usage in the field of ultrasonic examination. We find that combination of three tools (raypath, ultrasonic field computation, computa-

tion of response from defects) is very useful and in some cases it is necessary. Simulation of NDT is an essential part of qualification and inspection procedures in Czech Republic. In chapter 3, these three tools are described with some examples made by the author of this article.

2. Techniques of Ultrasonic Testing

The ultrasonic principle is based on the fact that solid materials are good conductors of sound waves. Whereby, the waves are not only reflected at the interfaces but also by internal flaws (material separations, inclusions etc.). The interaction effect of sound waves with the material is stronger the smaller the wave length, this means the higher the frequency of the wave.

$$\lambda = \frac{c}{f}$$

This means that ultrasonic waves must be used in a frequency range between about 0.5 MHz and 25 MHz and that the resulting wave length is in mm. With lower frequencies, the interaction effect of the waves with internal flaws would be so small that detection becomes questionable cases where the highest safety requirements are demanded (e.g. nuclear power plants, aerospace industry) [2].

Ultrasonic Testing uses high frequency sound energy to conduct examinations and make measurements. Ultrasonic inspection can be used for flaw detection/evaluation, dimensional measurements, material characterization, and more. A typical UT inspection system consists of several functional units, such as the pulser/receiver, transducer, and display devices. A pulser/receiver is an electronic device that can produce high voltage electrical pulses. Driven by the pulser, the transducer generates high frequency ultrasonic energy. The sound energy is introduced and propagates through the materials in the form of waves. When there is a discontinuity (such as a crack) in the wave path, part of the energy will be reflected back from the flaw surface. The reflected wave signal is transformed into an electrical signal by the transducer and is displayed on a screen [3].

2.1. Pulse Echo Technique

Pulse-echo ultrasonic measurements can determine the location of a discontinuity in a part or structure by accurately measuring the time required for a short ultrasonic pulse generated by a transducer to travel through a thickness of material, reflect from the back or the surface of a discontinuity, and be returned to the transducer.

2.2. Phased Array Technique

Phased array technique is currently the most advanced technique for ultrasonic testing. This technique is only an extension of pulse echo technique. The biggest difference compared to the pulse echo technique is in design of transducer. Phased array probe consists of a series of individual transducer elements placed in one house. Excitation of elements is controlled electronically and it is possible to change parameters of transducer and ultrasonic beam, e.g. dimension of transducer, angle and focal point of ultrasonic beam, etc.

With phased array probe it is possible to use several types of scanning, e.g. electronic scanning, sectorial scanning, etc.

2.3. Time of Flight Diffraction Technique

Time-of-flight diffraction (TOFD) method of ultrasonic testing is a sensitive and accurate method for the non-destructive testing of welds.

Measuring the amplitude of reflected signal is a relatively unreliable method of sizing defects because the amplitude strongly depends on the orientation of the crack. Instead of amplitude, TOFD uses the time of flight of an ultrasonic pulse to determine the position of a reflector. This technique consists of two transducers (emitter and receiver oriented in opposite directions) and is used to detect and size planar flaw by observing their top or/and bottom edges of diffraction echoes.

3. Simulation of Non-Destructive Testing

It is possible to use simulations for interpretation of results obtained by examination. For imaging of results all basic types of US images and their transformations can be used, which can serve e.g. for imaging of results in

3D model. On the basis of comparison of obtained US signal images it is possible to identify echoes which are obtained from defects with the help of simulation software, e.g. verifying of diffraction echo existence, separation of geometric echo from echo from defect, etc. Three main tools for simulations of ultrasonic testing are described in next chapters.

3.1. Raypath

Function of this tool is generating an image by tracing the path of ultrasonic waves in the test environment. Displayed lines represent the axis of the probe ultrasound beam with application of idealized reflection and transformation properties of the ultrasound signal. Signal amplitude is not considered in this tool. This tool could take into account different types of waves and these waves could be color coded. This tool may also take into account conversion of waves during reflection. **Figure 1** shows propagation of ultrasonic beam by angel probe. This beam is reflected on defect and on inner surface. Transformation from longitudinal to shear waves is also possible to see. Green color is for longitudinal waves and red for shear waves. This example is from our project on NDT qualification of nozzle to main circulation pipeline weld joint. This weld joint is located on nuclear power plant of VVER 440 type.

3.2. Ultrasonic Field Computation

Ultrasonic field computation is used to display propagation area of ultrasonic beams. On the market, there are some software that deal with the calculation of ultrasonic field. This tool could be used for:

- **Design of the phased array probe**

Simulation of ultrasonic field is very important for the design of ultrasonic probes, especially in the case of phased array probes. It is very important to design correct aperture and number of elements to avoid unwanted grating lobes. **Figure 2** shows correct design of a phased array probe with 32 elements. There is possible to see clear ultrasonic beam in refraction angle 40˚ in steel material. **Figure 3** shows undesirable design of phased array probe with the same aperture like previous probe, but only with 8 elements. It is possible to see strong grating lobe a weak ultrasonic beam for refraction angle 40˚ [4].

- **Coverage of inspected volume by acoustic pressure**

Another use of ultrasonic field simulation is when sectorial scanning is used and it is necessary to find out coverage of inspected volume by ultrasonic beam. **Figure 4** is an example of inspection volume coverage by phased array probe and sectorial scanning. Range of refraction angles are between 45˚ to 70˚. This example is from our project on NDT qualification of steam generator collector weld, which is located on Nuclear power plant Temelin in Czech Republic.

3.3. Computation of Response from Defects

Simulations are conducted to determine the optimum measurement parameters. Such parameters should be set

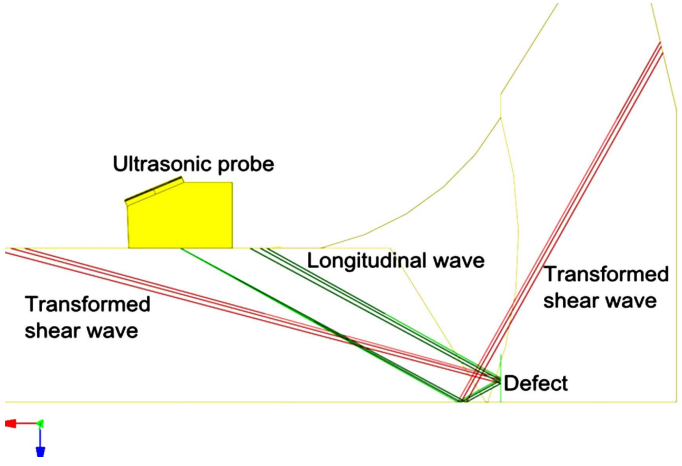

Figure 1. Example of raypath tool with wave conversion.

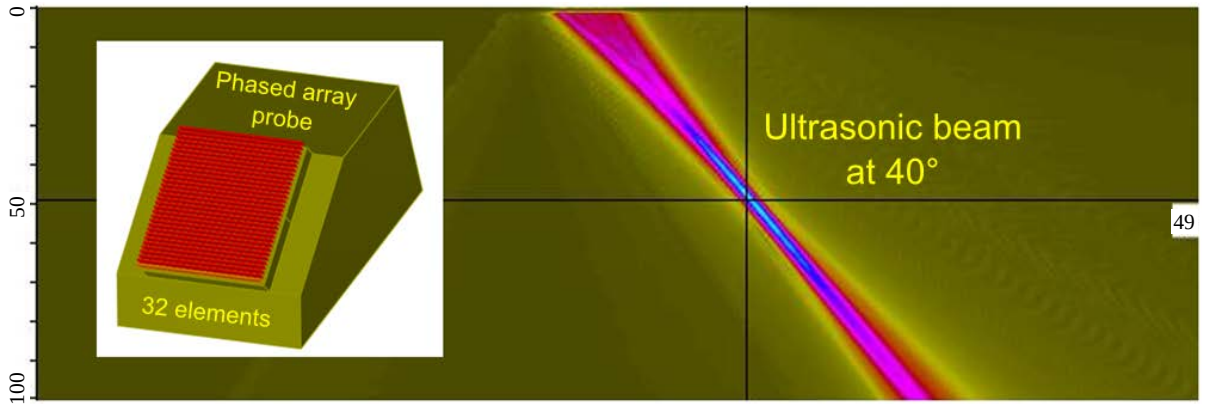

Figure 2. Phased array probe with 32 elements.

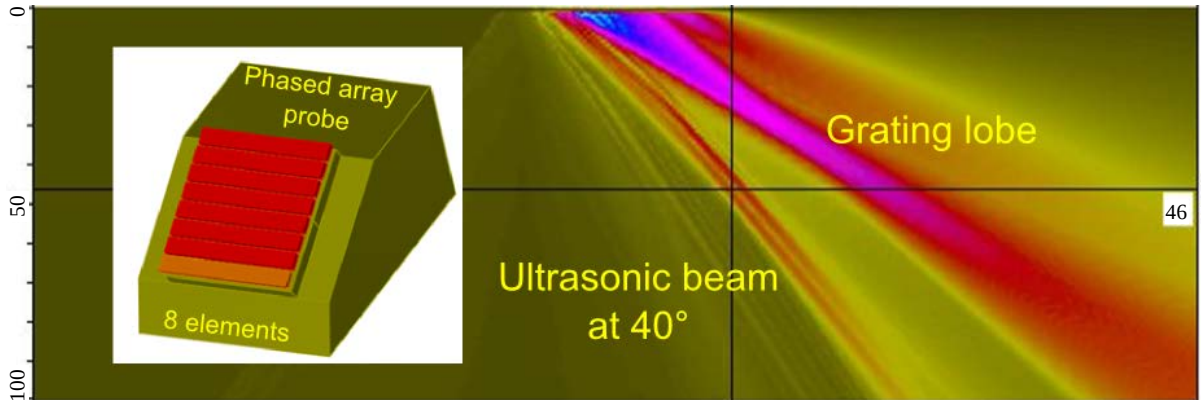

Figure 3. Phased array probe with 8 elements and unwanted grating lobe.

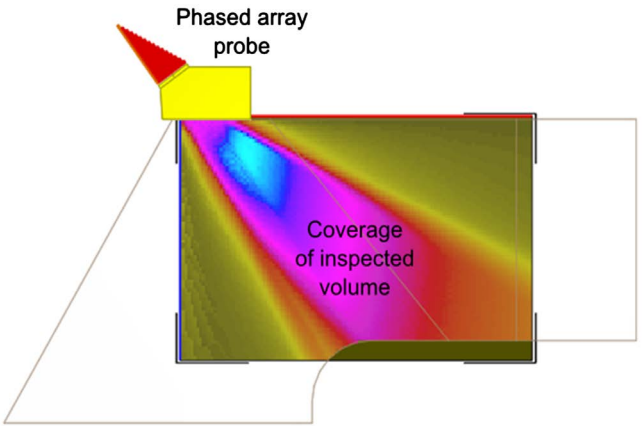

Figure 4. Coverage of inspected volume by sectorial scanning and phased array probe.

exact to detect defects during examination and meet with the criteria imposed for the current trial. Another application of simulation is in the process of evaluating the results of the examination. It means helping with identification of obtained echo-signals, design of calibration or test block, verifying of test equipment parameters, etc. In **Figure 5**, it is possible to see result from real examination compared to the results from simulation. This response is from real lack of fusion in the weld root. We found this lack of fusion in test block, which was used for qualification welders. This qualification was made for preparation of weld joint in steam generator collector repairs on nuclear power Dukovany in Czech Republic.

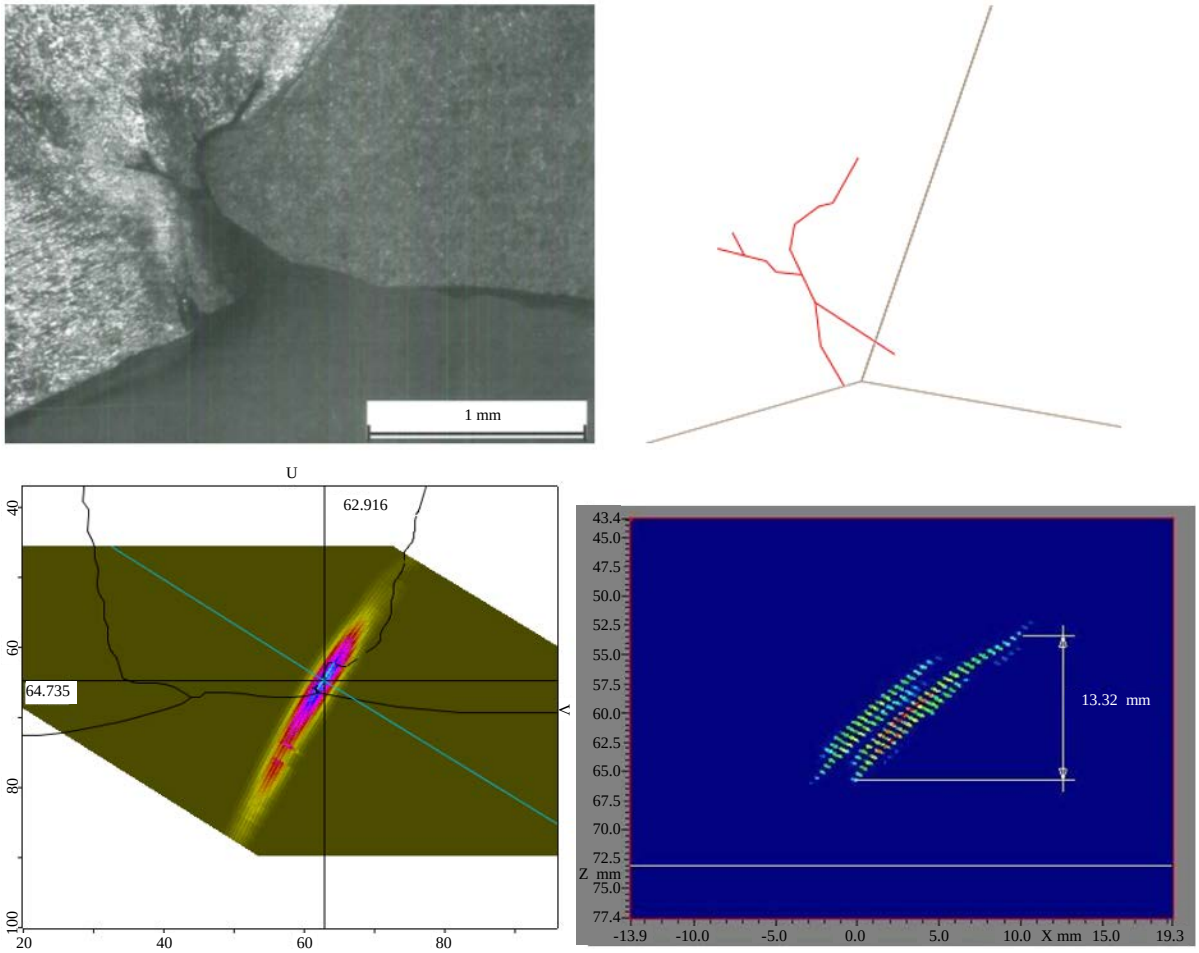

Figure 5. Real lack of fusion defect (left top), lack of fusion in simulation (right top), response from defect in simulation (left bottom), response from defect in real examination (right bottom).

4. Conclusion

Suitable assessments of inspected areas are necessary conditions for covering of safety service of important components in industry, especially at nuclear power plants. Implementing the new non-destructive methods and other supporting activities like computer modeling ensures increasing of examination quality of selected areas. That is why computer modeling is becoming an integral part of non-destructive testing. Examinations are extended by other additional information with the help of computer modeling. Other benefits are the possibilities to predict responses from defects, which are not manufactured in test block or even a simulation of a whole test block, which is not manufactured; or verification of usage of certain probe or method which belongs to possibilities of utilization of simulations.

Acknowledgements

The author would hereby express his greatest thanks to the SUSEN Project (CZ.1.05/2.1.00/03.0108), realized in the framework of the Operational Programme Research and Development for Innovations of the European Regional Development Fund (ERDF), for the financial support of the research.

References

[1] Mares, P., Horacek, L. and Vlcek, P. (2010) Recent Computer Activities and Achievements for UT Qualification of WWER Type NPPs Inspection Areas. *Proceedings of the* 8th *International Conference on NDE in Relation to Structural Integrity for Nuclear and Pressurised Components*, Berlin, 29 September-1 October 2010, 127-133.

[2] Kratkrämer, J. (1990) Ultrasonic Testing of Materials. 4th Edition, Springer-Verlag, Berlin.

[3] NDT Education Resource Center. http://www.ndt-ed.org/

[4] Neupauer, J. (2013) Praktickévyužitiemodelovaniaprinávrhu a výberesondy Phased Array. *Presentation on Sympózium Slovcert*, Senec, 16-17 October 2013.

Journal of Modern Physics, 2014, 5, 1173-1185
Published Online July 2014 in SciRes. http://www.scirp.org/journal/jmp
http://dx.doi.org/10.4236/jmp.2014.513119

Scientific Research

Flaw Detection Capability and Sensitivity in the Inspection of Nuclear Containment Liner and Shell Mock-Ups Utilizing a Magnetostrictive Sensor (MsS) Guided Wave UT Technique

Brian P. Hohmann[1], Joseph P. Crosson[1], Thomas C. Esselman[1], James J. Wall[2], Mike Quarry[2], Luke Breon[2]

[1]LPI, Inc., New York, NY, USA
[2]Electric Power Research Institute, Charlotte, NC, USA
Email: bhohmann@LPINY.com

Received 7 May 2014; revised 3 June 2014; accepted 26 June 2014

Abstract

This paper describes the results of a project on the inspection of visually inaccessible areas of nuclear containment liners and shells via the advanced Magnetostrictive sensor (MsS) Guided Wave (GW) nondestructive inspection technique. Full scale mockups that simulated shell and liner regions of interest in the containment of both a Pressurized Water Reactor (PWR) and Boiling Water Reactor (BWR) were constructed. Inspections were performed on the mock-ups in three stages to discern the signal attenuation caused by flaws and caused by concrete in the structures. The effect of concrete being in close proximity to the liner and shell was determined, and the capability to detect and size flaws via this GW technique was evaluated.

Keywords

Ultrasonic, Guided Wave, Nondestructive Inspection, Nuclear, Containment, Concrete, Mockup, Flaw Detection, Magnetostrictive Sensor, Pressurized Water Reactor, Boiling Water Reactor

1. Introduction

At a nuclear power plant, the containment building is of primary importance for safe operation. The primary

How to cite this paper: Hohmann, B.P., *et al.* (2014) Flaw Detection Capability and Sensitivity in the Inspection of Nuclear Containment Liner and Shell Mock-Ups Utilizing a Magnetostrictive Sensor (MsS) Guided Wave UT Technique. *Journal of Modern Physics*, **5**, 1173-1185. http://dx.doi.org/10.4236/jmp.2014.513119

containment and other safety related structures at a nuclear plant site must be capable of maintaining their design features for the operating life of the plant. Demonstrating the satisfactory condition of the containment building and other safety related structures is required for long-term operation of the plant, particularly when plant operation beyond 60 years is considered. Many pressurized water reactors (PWRs) have liners and most of those liners have concrete poured inside of them to form a floor. ID corrosion can occur in locations where there is an interface between the liner and the concrete. This location where the liner goes behind the concrete is a location of susceptibility to corrosion that is generally inaccessible via visual inspection. Water seals are typically installed at this location and they have the potential to be damaged or degrade over time in service, resulting in water intrusion between the concrete and the liner. Liner corrosion in the region from the ID was noted at twenty three PWRs—all caused by coating failures or moisture barrier degradation [1]-[3]. Much of the corrosion from the OD has occurred because of foreign material that was left in the concrete during initial plant construction. The drywell shells of boiling water reactors (BWRs) are also susceptible to ID and OD corrosion. Corrosion has been noted at Oyster Creek, Dresden, Hope Creek, and other commercially operating plants [4] [5]. The OD areas in the sand cushion region and in the ID near concrete that has been poured are also susceptible to corrosion over time. This operating experience shows that PWR and BWR liners are susceptible to corrosion if foreign objects were left in the concrete when it was initially poured and if these foreign objects are in contact with the metallic liner. The motivation for the current work was to demonstrate the ability to detect and quantify degradation in visually inaccessible areas of containment liners and shells, to allow informed decision making with regard to long-term operation of nuclear plants to be made.

Due to the fact that these locations where corrosion has been observed are generally inaccessible via visual inspection, there is a need to develop data on the feasibility of nondestructive examination (NDE) techniques that have the possibility of a high probability of detection (POD) for flaws. Guided waves (GW) are structure-borne elastic waves that propagate along the length of plate, guided by and confined within the inner or outer boundary of plate. This unique feature is a very capable tool for long-range plate inspection from a single probe location [6] [7]. Since the wave is guided by the plate boundary, the boundary decides on the wave modes and propagating velocity. The Magnetostrictive sensor (MsS) generates and detects ultrasonic guided waves electromagnetically in the material being tested. For the generation of ultrasonic waves, the sensor relies on the Magnetostrictive (or Joule) effect; which is the manifestation of small changes in the physical dimensions of ferromagnetic materials (on the order of several parts per million in carbon steel) caused by an externally applied magnetic field [6]. For wave detection, it relies on the inverse magnetostrictive (or Villari) effect. The change in the magnetic induction of ferromagnetic material is caused by mechanical stress (or strain). Since the probe relies on the magnetostrictive effects, it is called a magnetostrictive sensor (MsS).

A feasibility study was conducted in three stages to enable the inspection of the mockups at the following fabrication intervals: 1) Inspection of the liner and shell components with welds and studs but prior to concrete being placed and with no flaws; 2) Inspection of the mockup liner and shell components following the introduction of flaws meant to simulate potential in-service degradation but prior to placement of concrete; 3) Inspection of the mockup liner and shell components with flaws and with concrete placed and cured. The purpose of performing the inspections iteratively in the above described manner was to attempt to quantify the effect of signal attenuation in the GW method as a result of both flaws and concrete.

2. Mock-Up Design and Construction

To demonstrate the adequacy of the magnetostrictive sensor inspection technique for inspection of inaccessible metallic liner and shell surfaces, a number of mock-ups were constructed at LPI Inc.'s facilities in New York City. The mock-ups were designed to provide a full-scale, accurate representation of a PWR containment liner and a BWR drywell shell. Prior to construction, CAD drawings were prepared to provide a visual rendering of the fully fabricated assemblies. The PWR containment liner mock-ups were represented by two different mock-up constructions. One was for the transition of the external wall liner into the containment floor concrete. This is shown in **Figure 1**. A second mock-up was prepared for demonstrating a degradation screening process for a straight wall. The straight wall was meant to simulate an area where classical manual UT could be performed but would be too time consuming. This mock-up is shown in **Figure 2**. One of the benefits of guided wave UT is that since it is a technique capable for long-range plate inspection from a single probe location, it could be used as a "screening" process to quickly identify regions of interest for more detailed follow-up NDE

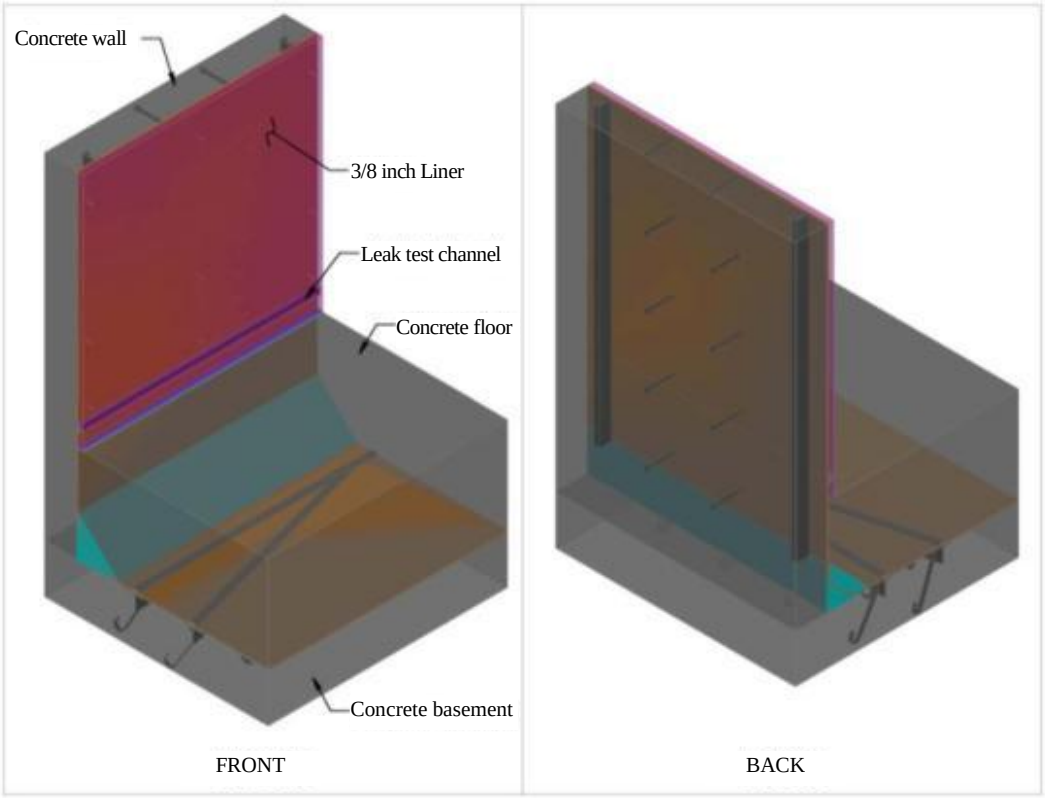

Figure 1. Rendering of mock-up of PWR containment wall liner.

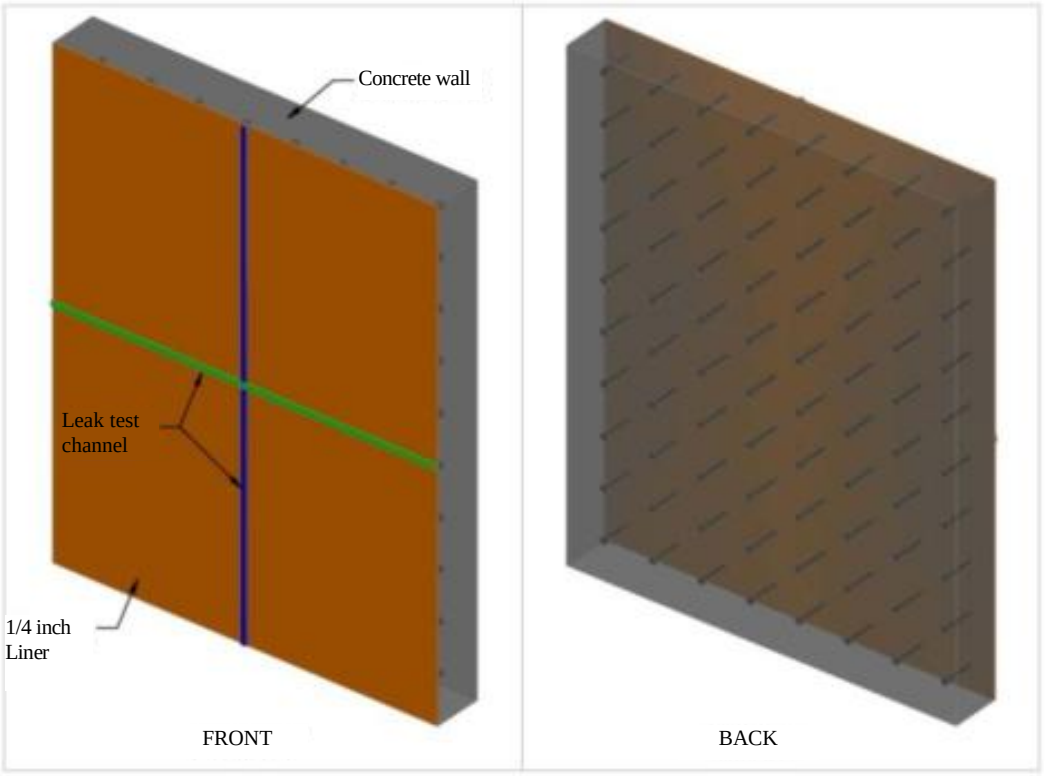

Figure 2. Rendering of mock-up of PWR flat wall liner.

inspection when utilized in the field at an operating plant. This NDE methodology provides redundancy to the overall inspection process that decreases the probability of false positives, increases the overall detection capability, and does both of the former in a cost-conscientious manner. The BWR drywell mock-up included the drywell shell adjacent to the sand cushion region. This is shown in **Figure 3**.

The mock-up shown in **Figure 1** is a replica of a typical liner design and includes liner plate butt welds, attachments, and surrounding concrete. The liner plate is 3/8 (0.375) inch (0.95 cm) thick along the wall and the curvature into the floor where it transitions at a weld to 1/4 (0.25) inch (0.64 cm) thickness. An additional weld in the floor region created a triangular steel section and an irregularly shaped steel section. Testing of this mock-up was performed to demonstrate the extent of the coverage of the MsS guided wave inspection system into the embedded liner and beyond the 90 degrees curvature where significant signal attenuation was anticipated due to contact with the steel embedment, welds, and concrete. The mock-up was oriented in the field-observed position with the containment wall concrete oriented vertically and the floor oriented horizontally. The potential effects of concrete bonding, concrete shrinkage, and deadweight on horizontal surfaces were then examined.

The mock-up of the straight wall shown in **Figure 2** represents a typical wall where the liner is exposed on one side and is backed by reinforced concrete on the other. The liner plate is 1/4 (0.25) inch (0.64 cm) thick. It contains butt welds and stud attachments on the concrete side. The mock-up of the BWR drywell shell demonstrated the feasibility to inspect the area of a nuclear plant which is embedded in the concrete and adjacent to the sand cushion. The shell was 1 1/8 (1.125) inch (2.86 cm) thick, which closely represented the field observed shell wall thickness. This increased thickness necessitated a change in the GW inspection system parameters, most notably the use of a lower frequency range.

The steel shell and liner components for the three mock-ups were fabricated at a company specializing in the

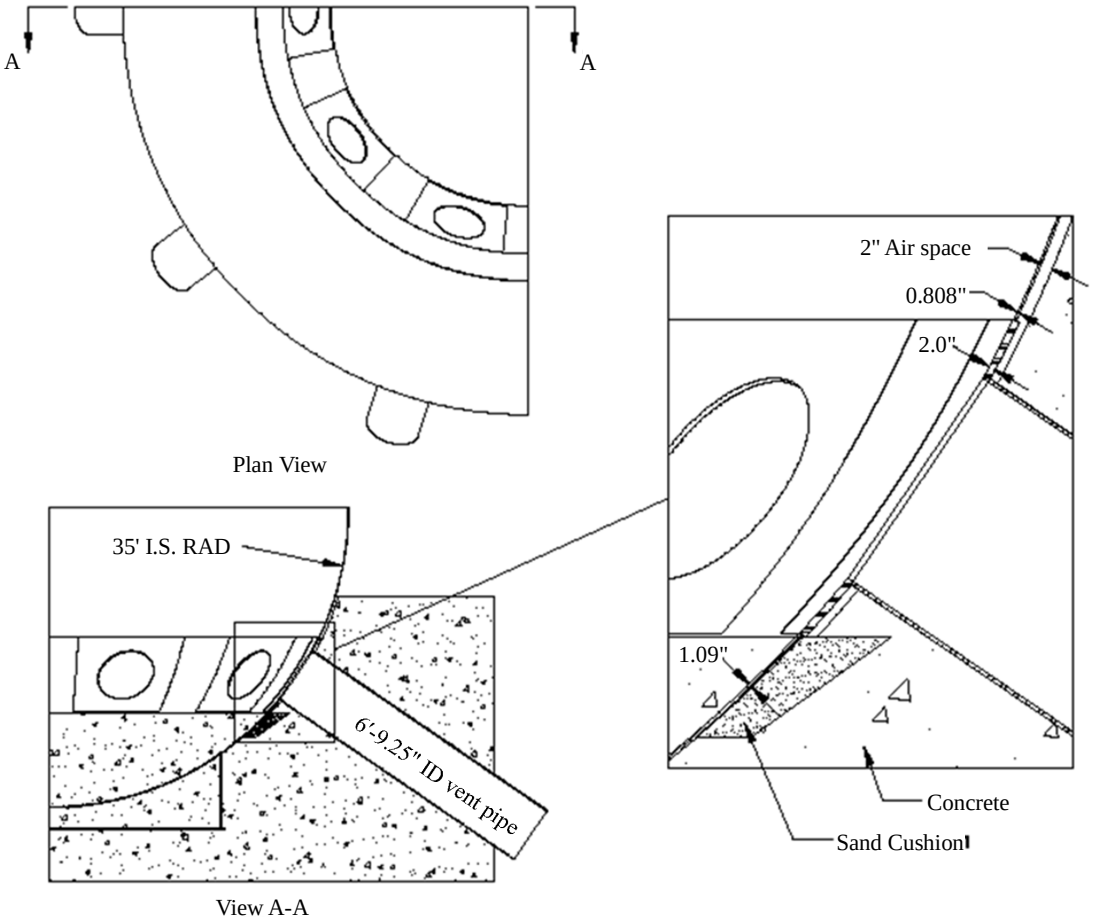

Figure 3. Rendering of mock-up of BWR drywell shell.

rolling of steel. The parts were delivered in pieces and all welding and final assembly was performed on site at LPI's laboratory facilities in New York City. The mockups were assigned the following nomenclature during testing: "BWR" for the BWR shell mockup, "A" for the PWR straight wall mock-up, and "G" for the PWR basemat mock-up.

Following assembly of the steel liner and shell components, the three mockups were inspected with the GW technique prior to any flaws being machined into them and prior to any concrete being poured, in order to gain a baseline reading. **Figure 4** and **Figure 5** show the mockups prior to flaw insertion and concrete placement, while **Figures 6-9** show the fully constructed mock-ups after flaw insertion and concrete placement. Flaws were placed on both the ID and OD sides. A coordinate system for each mockup was developed and the coordinates for all flaws was identified. Replication of all flaws was performed before concrete was poured so flaw topography could be maintained for future inspections.

3. Experimental Procedure

The model MsSR3030R instrumentation and probe (Guided Wave Analyis LLC, San Antonio, TX) shown in **Figure 10** were utilized to perform the guided wave testing. The operating software in the laptop computer controlled the operating parameters of the MsSR3030R instrumentation. Data was acquired through a USB port between the probe and laptop. The MsS probe consisted of a thin iron cobalt (FeCo) ferromagnetic strip and plate probe, which was used to apply a time-varying magnetic field to the nuclear mockups being tested. The instrumentation captured magnetic induction changes in the steel liner and shell components caused by the guided waves. The directional control of the wave propagation was achieved with this system by employing a phased array approach with two sensors. The GW was controlled such that propagation along one direction on either side of the MsS probe could be distinguished and separately evaluated.

Figure 11 shows dispersion curves that plot wave velocities at different frequencies propagating in 0.375-inch-thick (0.95 cm) plate. The plate has three wave modes: Symmetric Lamb wave (S), Asymmetric Lamb wave (A), and Shear-horizontal wave (SH). Except for the SH0 wave mode, the velocities of other wave modes are dispersive and vary with the wave frequency. The velocity of the SHO-wave, however, is constant (that is,

(a) (b)

Figure 4. (a) Front and (b) side view of the BWR mock-up prior to concrete placement.

Figure 5. The straight wall PWR mock-up, "A", lying with its OD side sticking up following welding of the four quadrants.

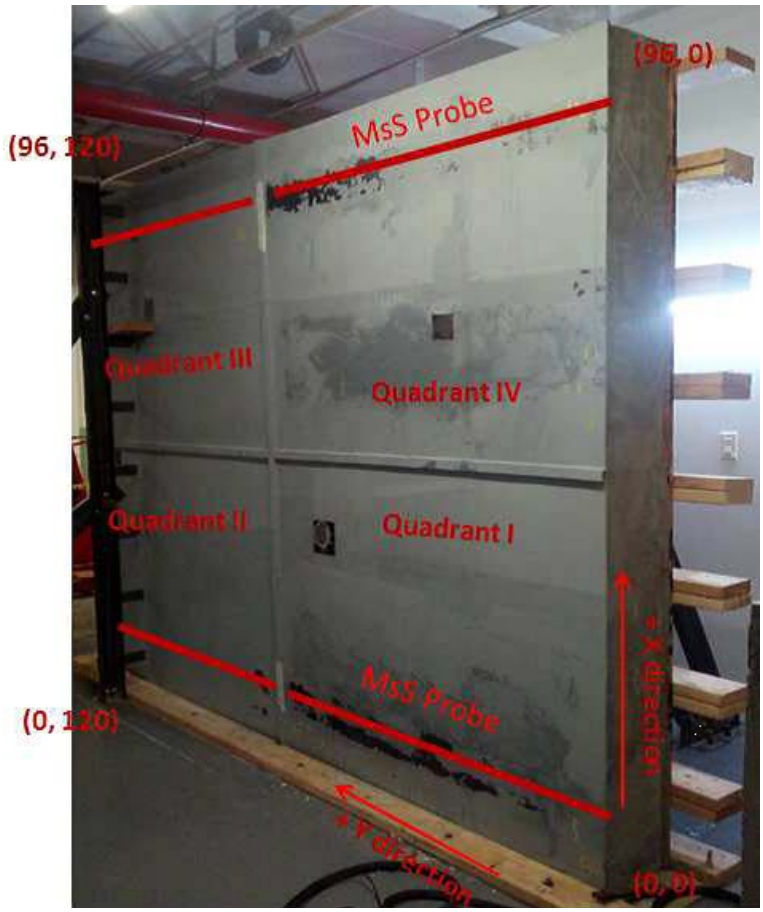

Figure 6. The PWR wall mock-up, "A", in the upright position following placement of concrete. Orientation of the four mock-up quadrants, the mock-up coordinate system for flaw location, and location of the Magnetostrictive sensor (MsS) probe placement noted in red.

Figure 7. The PWR basemat mockup, "*G*", following placement of concrete. Red arrow points to curved region of the liner.

(a) (b)

Figure 8. (a) Front and (b) side views of the fully constructed "BWR" shell mockup.

equal to the shear wave velocity of the plate material) and thus is independent of the frequency. This property means the SHO wave is non-dispersive so that its wave form does not change as the wave propagates a long distance. Therefore, the SHO wave mode is mostly used for the inspection of steel plate samples and was used for the evaluation of the nuclear mockups.

A scan was initially performed on the three mockups (labeled "A", "G", and "BWR") using the model MsSR3030R instrumentation prior to introduction of flaws and placement of concrete to generate a baseline signal response. The procedure utilized to acquire data included cleaning the steel liner and shell surfaces prior to testing. Any dirt or superficial corrosion was wiped off. If these tests were to be performed in the future

Figure 9. Appearance of the three fully constructed mock-ups.

Figure 10. MsSR3030R equipment and MsS plate probe used for inspecting mockups.

on-site at an operating plant and the test surface was rough, a wire brush or sand paper would additionally be used for surface preparation. Following surface preparation, FeCo strips of suitable length were prepared and attached at exposed steel locations via a wax bonding technique. The wax bonding technique was removable and did not damage the steel surface. Mechanical coupling, shear coupling or epoxy bonding are also considered suitable for attachment of the FeCo strip. Tape was placed over the length of the FeCo strip and position coordinates were marked on the tape. The FeCo strip was then conditioned (magnetized) for shear-horizontal mode operation. The MsS probe was then connected to the MsSR3030R instrumentation and placed on the object under test. Data was then acquired and analyzed, as shown in **Figure 12**. This procedure was followed on all mockups for all three stages of testing.

4. Results and Discussion

One result revealed from performing the baseline scans was that the thickness of the steel liner or shell under inspection affected both the allowable and the optimal test frequencies. For the “BWR” mockup, which was 1.125 inch (2.86 cm) thick, data were acquired at nine locations along the vertical y-axis direction with the horizontal

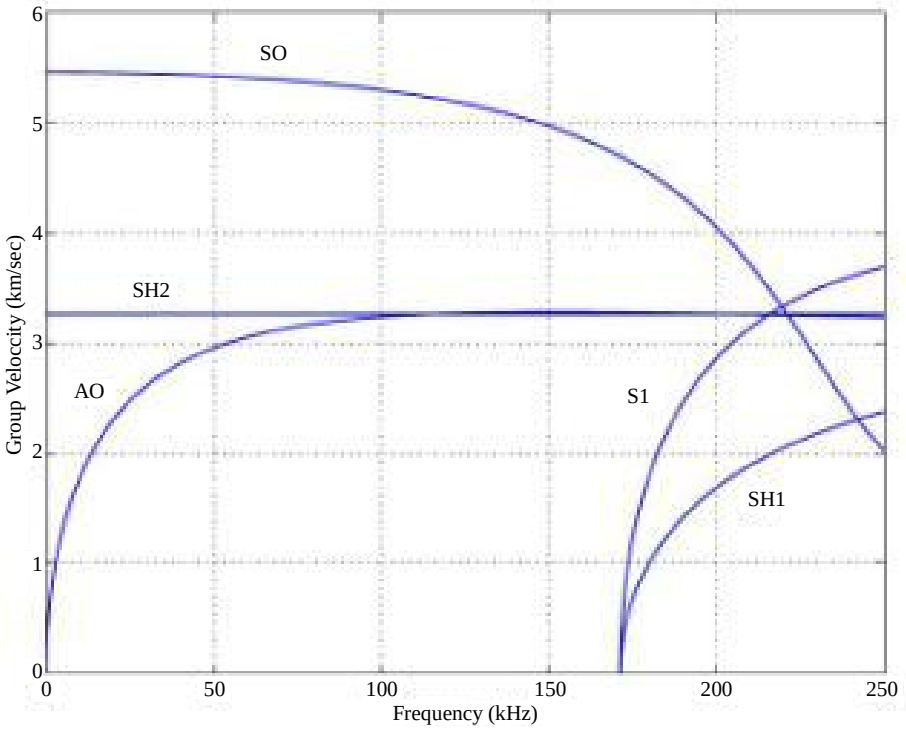

Figure 11. Dispersion curves of 0.375-inch-wall (0.95 cm) steel plate.

Figure 12. Baseline data acquisition of "G" mockup with MsS instrumentation.

x-axis position being held constant following placement of the FeCo strip. Two different lengths of MsS probe, 4 in. and 8 in. were used to acquire baseline data. Data from the 4 in MsS probe were acquired at center frequencies of 64, 90, and 128 kHz and two cycles. The resulting data plots for this mockup with the probe located at the (−26, 12) coordinate position are shown in **Figure 13** and **Figure 14**. The data shows one end-reflected

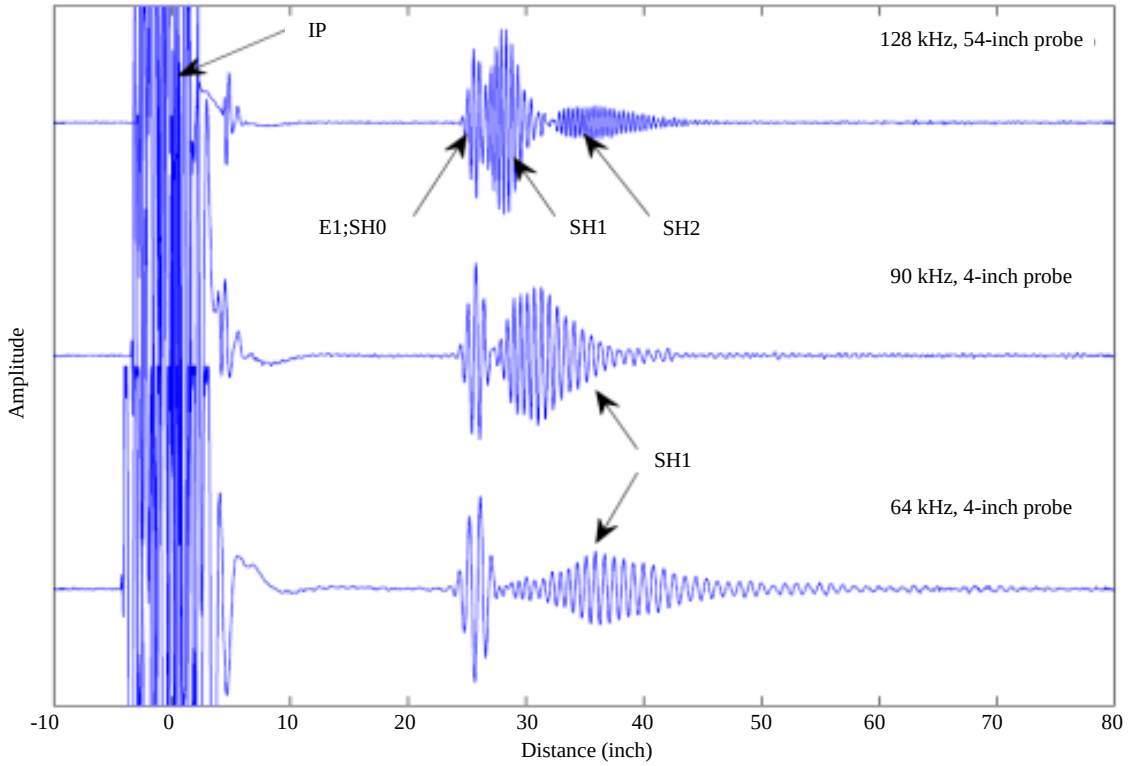

Figure 13. RF data plot acquired with 4 in. long MsS plate probe located at (−26, 12).

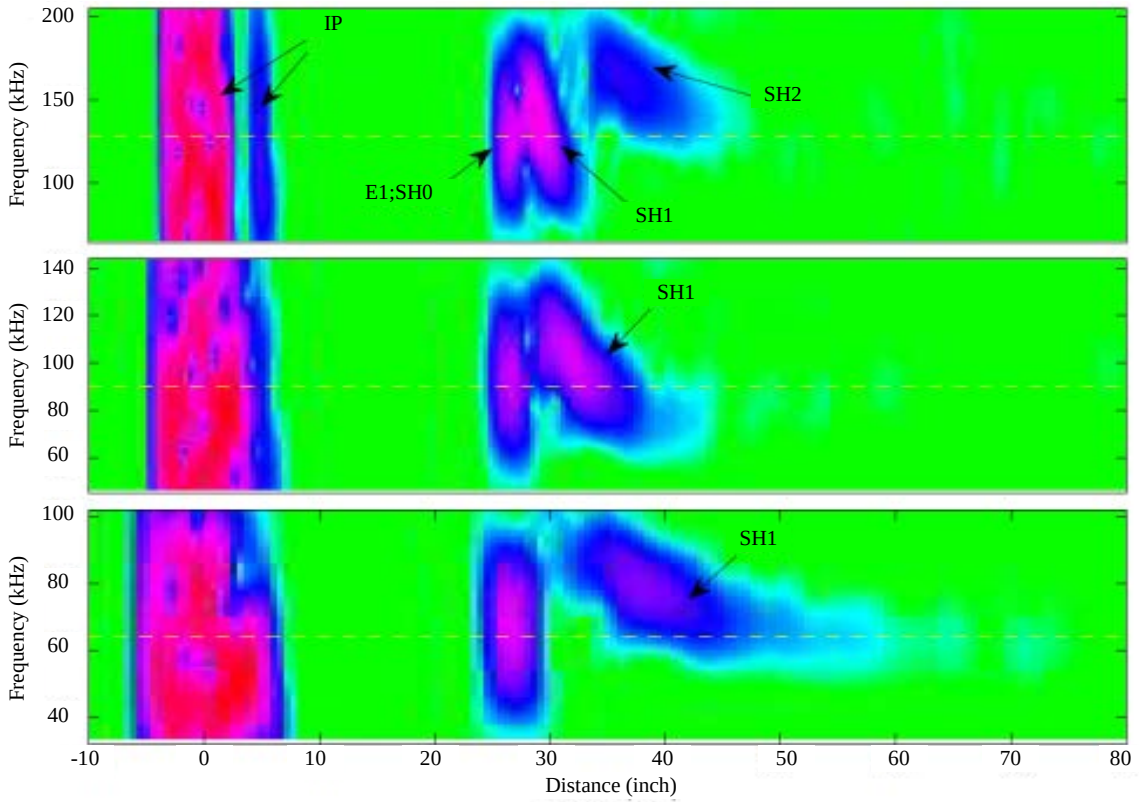

Figure 14. Spectrogram data plot of the RF data in **Figure 14**.

signal, E1, for three different shear-horizontal wave modes (SH0, SH1, and SH2). The spectrogram data of **Figure 14** shows the dispersive characteristics of the SH1 and SH2 wave modes. The dispersion curve for the BWR mockup is shown in **Figure 15** for shear-horizontal wave modes only. The cutoff frequencies for SH0 through SH4 are shown with respect to group velocity in **Figure 15**. The cutoff frequency is defined as the frequency at which the mode does not remain purely guided, or in other words, when a guided wave mode is converted into a radiation mode. The effectiveness of the subject NDE technique requires that the wave remain guided. The cutoff frequencies for the SH1 and SH2 wave modes were determined to be 57 kHz and 115 kHz. In an attempt to remove the dispersive SH1 and SH2 wave modes, follow-up data was acquired at lower frequencies of 32 kHz and 45 kHz, however the resulting data did not have a high signal-to-noise ratio (SNR) for end-reflected signals. It was determined that at frequencies of approximately 90 kHz and higher, the amplitude of the SH1 mode is approximately equal to the SH2 mode. For this reason, during subsequent inspections this higher operating frequency was used and the number of cycles was increased. The two operating conditions found to generate the best SNR for detection of flaws were determined to be 1) 82 kHz, 5 cycles and 2) 138 kHz, 5 cycles. The liner mockups "A" and "G", which were only 0.375 in. and 0.25 in. thick, did not have the same limitations with dispersive waves as was found with the "BWR" mockup.

Various types of flaws were introduced into all three of the mock-ups in order to simulate flaws typical of in-service degradation, such as pitting and corrosion, as well as flaws typically used in the evaluation of nondestructive systems, including flat bottom hole (FBH) flaws and cluster-type flaws of multiple FBHs in close proximity. The flaws and the number of flaws were selected to determine the feasibility and sensitivity of various inspection techniques. The flaws would have been different if they were to be used for qualification of

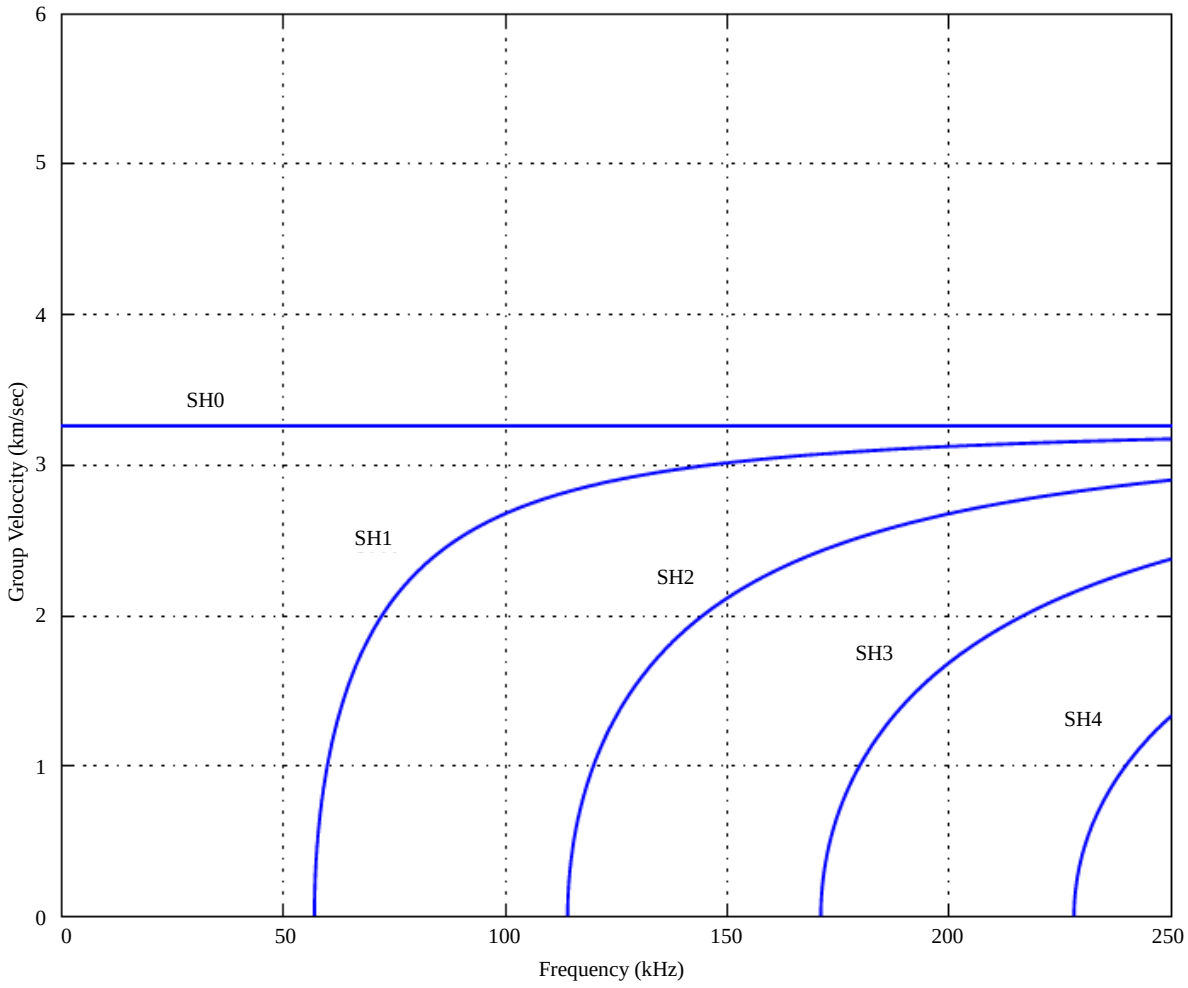

Figure 15. Shear-Horizontal mode dispersion curve for BWR mockup.

inspectors. In all cases, a point of origin and coordinate system were selected for each mock-up, and the exact location of flaw placement was noted in order to compare with future inspections after concrete placement obscured visual observation of flaws. Flaws of varying depths and diameters were placed on both the ID and OD sides of the mock-ups, as shown in **Figure 16**, and a flaw map legend was developed to facilitate the quantification of each NDE technique with respect to flaw detection. A full description of the flaw map and inspection results is provided in reference [8]. Prior to pouring of the concrete, all flaws were replicated and then filled with a non-conductive epoxy mount material to inhibit intimate contact of the concrete with the flaw.

For the "BWR" mockup, six flaws were inspected from the ID side and five flaws from the OD side. The MsS guided wave UT system was able to detect all six flaws (6/6) on the ID side prior to concrete placement, and three of five flaws (3/5) on the OD side prior to concrete placement. Following placement and curing of the concrete, the system detected 5/6 flaws on the ID side and 2/5 flaws on the OD side. Flaws that were not detected prior to concrete were not detected after concrete had been poured. The flaw type with the lowest detectability was the "scalloped" flaw, which had an irregular shape and was meant to simulate actual in-service wall loss. Both the diametrical size of the flaw as well as the depth of the flaw affected detection capability.

For the "G" mockup, nine flaws were inspected from the ID side and four flaws from the OD side. The MsS guided wave UT system was able to detect 7/9 flaws on the ID side and 4/4 flaws on the OD side prior to concrete placement. Following placement and curing of the concrete, the system detected 7/9 flaws on the ID side and 3/4 flaws on the OD side. As was the case with the BWR mockup, flaws not detected prior to concrete were not detected after concrete had been poured. Flat-bottom hole (FBH) and cluster type flaws were in general more easily detectable than scalloped type flaws. Detection of pitting flaws depended on flaw depth. In general, the presence of welds significantly attenuated the signals from the NDE technique. The presence of a liner thickness deviation at the weld location in the basemat region of the mock-up also significantly lowered flaw detection capability.

For the "A" mockup, three flaws were inspected from the ID side and 13 flaws from the OD side. The MsS guided wave UT system was able to detect 3/3 flaws on the ID side and 11/13 flaws on the OD side prior to concrete placement. Following placement and curing of the concrete, the system detected 3/3 flaws on the ID side and 10/13 flaws on the OD side. Flaws not detected prior to concrete were not detected after concrete had been poured. Sensitivity to flaw detection was decreased for flaws in close proximity to mockup features such as studs or leak-tight channels.

For all three stages of testing, data was acquired and evaluated by an ASNT Level III inspector certified in Guided Wave UT. In general, it was demonstrated that flaws or progressive degradation such as simulated corrosion could be detected with the GW technique in visually inaccessible areas of the mock-ups. Simulated

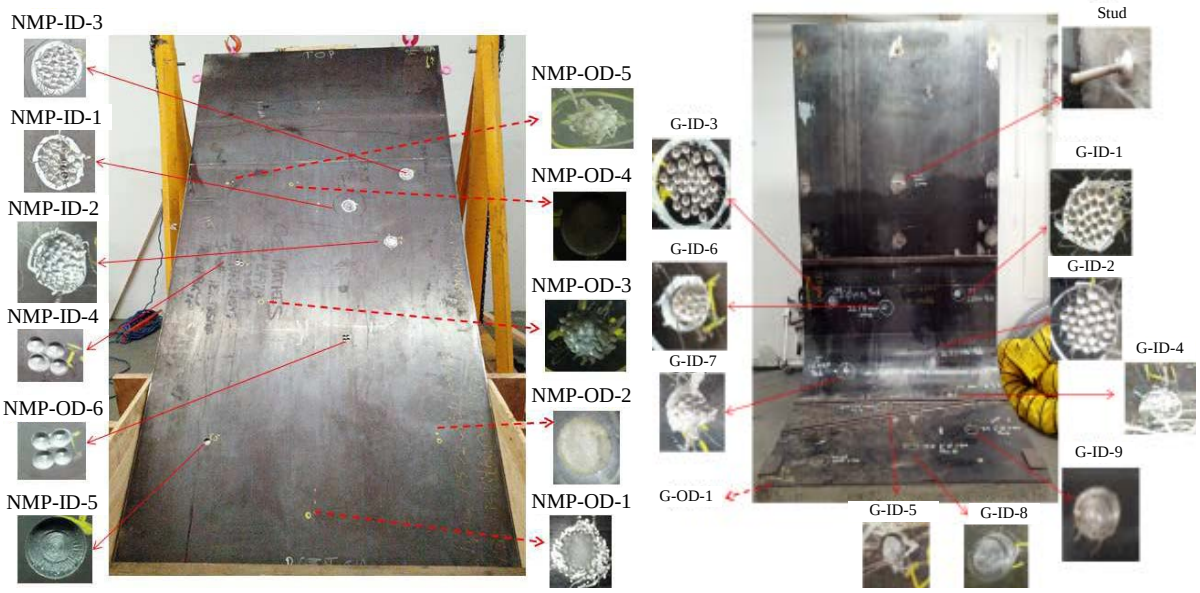

Figure 16. Various flaws inserted into both ID and OD side of the BWR and G mock-ups.

corrosion-type flaws, as small as 2 inches in diameter, were detected at a distance of several feet with the advanced NDE technique. Flaws with a scalloped-type appearance had the poorest detection capability. Significant GW signal attenuation was observed at weld locations, with an approximately 50 percent loss in amplitude observed. It should be noted that the signal effectively passed through three welds, as fillet welds were required for placement of the leak-tight channels, which were found around all full-penetration butt welds. Surprisingly, the presence of concrete had very little effect on the detection capability of the MsS guided wave system. It is believed that shrinkage of the concrete during curing permitted a small (micrometers) air gap to be present between the concrete and the metal liners and shell. This air gap allowed wave propagation over long distances. If the concrete had been in intimate contact with the liner and shell regions, it is expected that wave propagation would have been severely inhibited. The flaw sizing capability of the MsS system was not found to have adequate precision for application in operating plants, and improvement in this area is a goal of future research and development.

5. Conclusion

This research demonstrated that flaws or progressive degradation such as simulated corrosion could be detected with the GW technique in visually inaccessible areas of the constructed nuclear containment mock-ups. Simulated corrosion-type flaws, as small as 2 inches in diameter, were detected at a distance of several feet with the advanced NDE technique. In general, the presence of welds significantly attenuated the signals from the GW technique. The presence of a liner thickness deviation at the weld location in the "G" mock-up also significantly lowered flaw detection capability and increased signal attenuation. Future research in optimization of the flaw sizing ability of the MsS instrumentation would be required before implementation of the technique could be pursued in an operating nuclear plant.

Acknowledgements

This work was supported by the Electric Power Research Institute (EPRI) and the United States Department of Energy (DOE) through Idaho National Laboratory (INL).

References

[1] Dunn, D., Pulvirenti, A. and Hiser, M. (2011) Containment Liner Corrosion Operating Experience Summary, Technical Letter Report, Revision 1. US Nuclear Regulatory Commission, Office of Nuclear Regulation Research, Rockville.

[2] First Energy, Beaver Valley Power Station Unit 1, Containment Liner Corrosion Report, CR 06-0122, ML091960488.

[3] NRC Letter from J. White to P. Sena (2009) Beaver Valley Power Station, Unit 1, NRC Routine Inspection Report 05000334/2009006, ML091870328.

[4] US Nuclear Regulatory Commission License Renewal Interim Staff Guidance LR-ISG-2006-01 (2006) Plant Specific Aging Management Program for Inaccessible Areas of Boiling Water Reactor Mark I Steel Containment Drywell Shell, ML063210041.

[5] US Nuclear Regulatory Commission Information Notice 2011-15 (2011) Steel Containment Degradation and Associated License Renewal Aging Management Issues.

[6] Kwun, H. (1999) NUREG/CR-5724 Feasibility of Magnetostrictive Sensor Inspection of Containments.

[7] Pei, J., Yousuf, M.I., Degertekin, F.L., Honein, B.V. and Khuri-Yakub, B.T. (1995) Lamb Wave Tomography and Its Application in Pipe Erosion/Corrosion Monitoring. *Research in Nondestructive Evaluation*, **8**, 189-197.

[8] (2013) Synthetic Aperture Focusing Technique and Guided Wave Examination of Containment Liners and Shells. EPRI Technical Report No. 000000003002001720. Electric Power Research Institute, Palo Alto.

Journal of Modern Physics, 2014, 5, 1186-1201
Published Online July 2014 in SciRes. http://www.scirp.org/journal/jmp
http://dx.doi.org/10.4236/jmp.2014.513120

A Receiver Model for Ultrasonic Ray Tracing in an Inhomogeneous Anisotropic Weld

Q. Liu, Gert Persson, Hakan Wirdelius

Department of Materials and Manufacturing Technology, Chalmers University of Technology, Göteborg, Sweden
Email: gert.persson@chalmers.se

Received 30 March 2014; revised 27 April 2014; accepted 21 May 2014

Abstract

In this paper, a receiver model for ultrasonic ray tracing simulation is described. This is a complementary part of an existing simulation model and is the next step towards a numerical solution to the inverse problem and thus a NDT methodology for characterization of the dendrite orientation in a weld. The establishment of the receiver model is based on the electromechanical reciprocity principle. A concise retrospect of the weld model and the 2D model is made. The reciprocity principle is applied in an original way to handle the model problem including the back wall. Experimental qualitative validations for both *P* and SV waves on a specific weld are also made for C-scans included in this paper. Two different cases are studied. The first is a direct incidence of an ultrasonic ray towards the weld, and the second is a reflection from the back surface in the base material followed by an incidence to the weld. Even though mode-converted rays are excluded in the simulations, both the *P* and SV probe-models show the same behavior as the experimental results. The qualitative validation though reveals that it even if a thorough time-gating of received information would enable exclusion of mode-conversion in the model, inaccuracy of experimental results is affecting the evaluation of the weld model.

Keywords

Ultrasonic Receiver Model, Reciprocity Principle, 2D Ray Tracing

1. Introduction

In-service inspection of components that includes welds in austenitic stainless steel and Inconel metal has revealed systematic faults that are due to unpredictable paths of the ultrasound in the welded material. These welds exhibit not only highly anisotropic behavior but also involve inhomogeneous ultrasonic properties. This is

How to cite this paper: Liu, Q., Persson, G. and Wirdelius, H. (2014) A Receiver Model for Ultrasonic Ray Tracing in an Inhomogeneous Anisotropic Weld. *Journal of Modern Physics*, **5**, 1186-1201. http://dx.doi.org/10.4236/jmp.2014.513120

caused by the solidification process and the orientation of the dendrites (*i.e.* large grain structures) is governed by the temperature gradient in the cooling process.

Modeling of ultrasonic non-destructive testing (NDT) is important and helpful e.g. in predicting the response of an NDT inspection, correctly analyzing output data or acquiring a medium's mechanical properties. Many endeavors have been made to simulate this process. Among them, some special efforts are made to ultrasound propagation through an anisotropic weld [1]-[7]. When ultrasonic NDT is performed on a weld with strong anisotropy, special phenomena may occur compared to same inspection conducted on an isotropic medium. For example, the group velocity does not necessarily have the same propagating direction or amplitude as the phase velocity. This will make ultrasound beams propagate in an unexpected or unpredictable way through a weld.

This paper is a part of an initiative to develop a methodology that estimates grains' orientations in an anisotropic weld by using ultrasonic information in an inverse scheme. Well defined anisotropy in the simulated volume is prerequisite in order to make simulations of the forward problem, *i.e.* ultrasonic inspection of an anisotropic weld. The framework of such an initiative consists of a weld model, a forward 2D ray tracing model, experiments and an inverse problem solver. The latter justifies the limitations in the simplified model presented in this paper (e.g. 2D model, no mode conversion and ray tracing). The assumption of the weld being two dimensional and transversely isotropic is often used [8]-[12] and has recently also been experimentally validated [13]. Furthermore, the grain orientation is believed to be an essential factor that affects the propagation of ultrasound. In most simulation cases, a simple weld model is created by studying the macrograph of an austenitic weld. Different algorithms are then utilized to simulate the propagation of ultrasound through weld models. There also exist other methodologies to deduce anisotropic weld models that are not based on information retrieved from macrographs from reproduced welds. Gueudre *et al*. [14] have created a model by considering the welding process. In their models, the grain's orientation at different positions is decided by several parameters such as the chamfer geometry, the number of passes and the diameter of electrodes.

Another 2D ray tracing model was recently validated by using EFIT calculations [15] with very good agreement. In simulating the propagation of ultrasound through the weld model, the ultrasonic beam is approximated for high frequencies as a ray. The direction of the ultrasonic energy is continuously followed. Transmission and reflection are considered on the fusion lines between the base material and the weld, as well as on the boundaries between the sub regions in the weld. In the simulation, no mode conversion between the *P* wave and the SV wave is considered. This can be experimentally assessed by gating out the received information in thoroughly chosen time window. As a consequence, only the wave with the same mode is traced from the transmitter to the receiver.

In the present paper, a receiver model is presented, which is a continuation of a previously developed forward ray tracing model [16]. For the modeling of a receiver in an ultrasonic NDT system, Auld's electromechanical reciprocity principle [17] [18] is the most well-known approach. In most cases, it is applied to simulate the detection of a diffracted signal from a scatterer in a medium [19]-[22]. The reciprocity principle is employed to model the detection of the ultrasonic transmitted signal in the 2D ray tracing program. There are seven sections in this paper. The second section is a brief retrospect of the weld model and the forward ray tracing model. It is followed by a discussion of the receiver model. Simulations and validations of the receiver model are introduced in Sections 4 to 6. Discussions and concluding remarks are presented in Section 7.

2. A Retrospect of the Established 2D Ray Tracing Model

The forward model is composed of four main elements: a weld model, a transmitter model, a 2D ray tracing algorithm and a receiver model. In a previous paper [16], the first three models have been presented. A brief description is repeated here.

The weld model is established by studying the crystalline structure of a V-butt weld. The prototype is a weld specimen provided by Swedish Qualification Center (SQC) and defined as weld B27 in [17]. Following the process of creating a weld model introduced in the previous paper and based on the macrostructure identified in **Figure 1(a)** the weld model is defined as shown in **Figure 1(b)**. There are about eighty sub-regions in it, which have their own particular grain orientations. Each sub-region is considered homogeneous, lossless and transversely isotropic. For the weld model used in this paper, the grains' elastic constants are $c_{11} = 249$ GPa, $c_{12} = 112$ GPa, $c_{13} = 145$ GPa, $c_{33} = 216$ GPa, $c_{44} = c_{55} = 129$ GPa and $c_{66} = (c_{11} - c_{12})/2$ (with the axis of symmetry in the local x_3-direction) and the density is $r = 8.30 \times 10^3$ kg/m^3 [17]. The base material outside the

weld is modeled as conventional stainless steel and is prescribed to be isotropic (Lamé constants $\lambda_L = 109$ GPa, $m_L = 79$ GPa and density $r = 8.02\times10^3$ kg/m^3). The dimension of the weld is as follows. The upper width is assumed to be 18 mm, and the lower width is 13 mm. The height is supposed to be 22 mm. For the convenience of the ray tracing simulations, the curved boundaries in the original weld model is further replaced by straight lines, which is shown in **Figure 1(c)**.

The model of the transmitter is created from a truncated traction distribution representing the pressure produced by the probe on the surface of the component [16]. The traction distribution is correlated to a presumed plane wave propagating in a half-space with prescribe direction. Taking a plane P wave as an example, in the frequency domain, it can be described by the following expression,

$$\boldsymbol{u}_p = A\left(\sin\gamma\boldsymbol{e}_1 + \cos\gamma\boldsymbol{e}_3\right)e^{ik_p\left(\sin\gamma\cdot x_1 + \cos\gamma\cdot x_3\right)} \tag{1}$$

where A is the amplitude of the wave; γ is the angle between the propagation direction and the x_3 axis, and k_p is thewave number. A diagram describing this assumption is shown in **Figure 2**.

A truncation of the corresponding traction distribution along the upper surface of the half-space is performed, which provides

$$\boldsymbol{t}_p^{(\boldsymbol{e}_3)} = \begin{cases} i\mu A k_p\left(\left(\sin2\gamma\right)\boldsymbol{e}_1 + \left(\dfrac{k_s^2}{k_p^2} - 2\sin^2\gamma\right)\boldsymbol{e}_3\right)e^{i\left(k_p\sin\gamma\right)x_1} & \left(a \le x_1 \le b\right) \\ 0 & \text{otherwise} \end{cases} \tag{2}$$

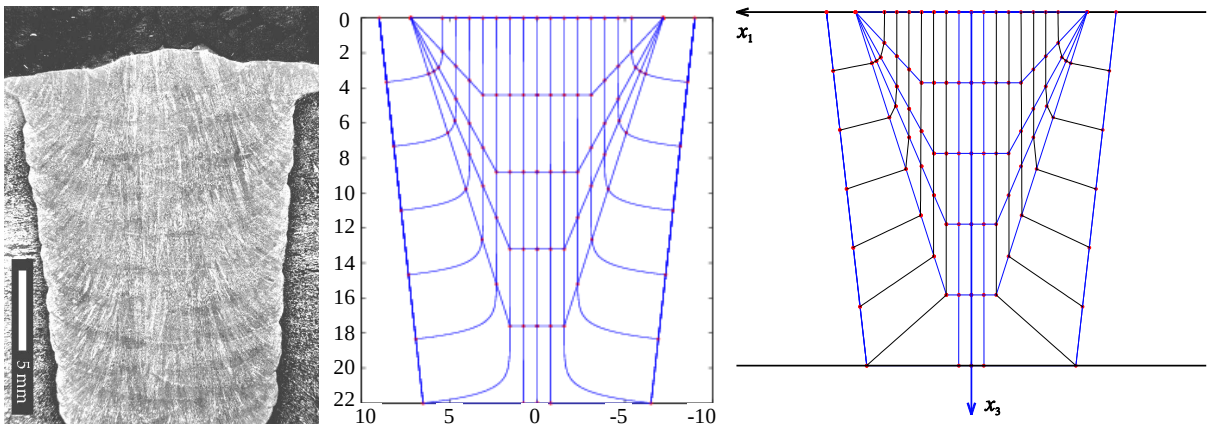

(a) (b) (c)

Figure 1. A weld model is generated by studying the macrograph of a typical weld.

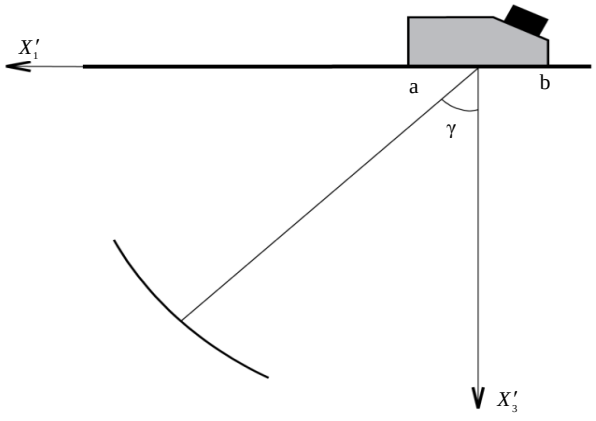

Figure 2. The transmitter model is generated from a presumed plane wave propagating in an isotropic half-space.

where μ is the shear modulus and k_s is the wave number of the S wave.

If Fourier transform in x_1 is fulfilled, the above truncated traction distribution is

$$\hat{\boldsymbol{t}}_p^{(\boldsymbol{e}_3)}\Big|_{x_3=0} = i\mu A k_p \left((\sin 2\gamma)\boldsymbol{e}_1 + \left(\frac{k_s^2}{k_p^2} - 2\sin^2\gamma \right) \boldsymbol{e}_3 \right) F_p(q;a,b) = \mu\left(T_1^p \boldsymbol{e}_1 + T_3^p \boldsymbol{e}_3 \right) \tag{3}$$

In this expression, $q = k_p \sin\gamma$ and

$$\begin{cases} F_p(q;a,b) = \int_a^b e^{i\left(k_p \sin\gamma\right)x_1} e^{-iqx_1} \mathrm{d}x_1, \\ T_1^p = iAk_p (\sin 2\gamma) F_p(q;a,b), \\ T_3^p = iAk_p \left(\frac{k_s^2}{k_p^2} - 2\sin^2\gamma \right) F_p(q;a,b). \end{cases}$$

Hence, Equation (3) is taken as the model of the ultrasonic transmitter.

A simple 2D ray tracing algorithm has also been developed. The ray direction, which is also the ultrasonic energy direction, is derived from the relationship between the phase velocity and the energy velocity (the energy velocity must always be normal to the slowness surface). Since the group velocity and the energy velocity are identical for acoustic waves in a lossless medium, an expression can be utilized to calculate the energy velocity [23],

$$\boldsymbol{v}_g = \boldsymbol{e}_1 \frac{\partial \omega}{\partial k_1} + \boldsymbol{e}_3 \frac{\partial \omega}{\partial k_3} \tag{4}$$

with k_1 and k_3 as the components of the wave vector in x_1 and x_3 directions [16]. Transmission and reflection on the fusion lines between the weld and the base material, as well as on the boundaries between different sub-regions in the weld model are considered, which produce both the transmitted ray direction and the relative amplitude. Mode conversion is neglected in this 2D ray tracing model, which means that only waves of a single type are followed continuously. If there is no transmitted body wave generated, the ray tracing algorithm will stop.

3. The Receiver Model

In the modeling process, the ultrasonic testing is assumed to be performed with a transmitter-receiver structure of pitch-catch configuration. According to Auld's reciprocity principle, the response of the receiver model can be expressed by the change of the electrical transmission coefficient between two states that correspond to the situations with or without a scatterer. Hence, the response of the ultrasonic receiver model can be calculated as

$$\delta\Pi = \frac{i\omega}{4P} \int_\Gamma \left(\boldsymbol{u}_2 \cdot \boldsymbol{t}_1 - \boldsymbol{u}_1 \cdot \boldsymbol{t}_2 \right) \mathrm{d}\Gamma \tag{5}$$

here, ω is the angular frequency and P is the probe electrical power. Γ denotes the border of a closed integration contour surrounding the scatterer, $\boldsymbol{u}$ denotes the displacement vector, and $\boldsymbol{t}$ is the traction. Subscripts 1 and 2 indicate that the field is linked to two different states, 1 and 2. It is the difference between these two different states that produces the change in the electrical transmission coefficient. Auld's reciprocity argument is only valid for a loss-free medium (*i.e.* no viscous damping) which is modeled in this case. The found deviations between experimental and simulated results presented in next chapter could partly be explained by this diversity.

For the receiver model in this paper, state 1 is chosen as the actual testing situation. As shown in the left part of **Figure 3**, in this state the transmitter works in the presences of the reflecting back wall and the weld. The "scatterer" in Auld's formalism [18] then consists of both the weld and the lower back surface. The transmitter is located at positions along the negative x_1 axis and outside the weld. In state 2, the scatterer, defined above, is absent. The receiver acting as a transmitter then works over a homogeneous half-space with the same elastic properties as the base material. In addition, the transmitter functions along the positive x_1 axis and outside the weld. When performing calculations according to Equation (5), the integration contour is selected as the dotted lines in **Figure 3**. Thus, the whole scatterer is enclosed by the integration contour and the main task in simulating the

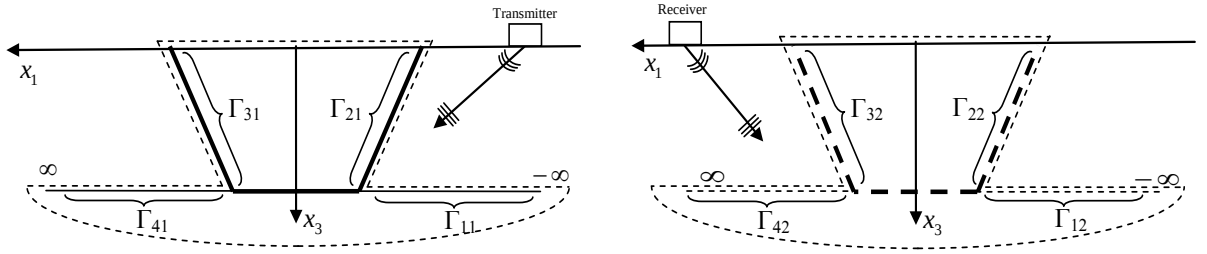

Figure 3. Illustrations of state 1 and 2 in the reciprocity model.

received signal is to determine the displacement $\boldsymbol{u}$ and the traction $\boldsymbol{t}$ along the integration contour in these two states.

Since the weld's upper border $(x_3 = 0)$ is assumed to be traction free in both states, this part of the integration gives no contribution to the calculation. In addition, the borders Γ_{11} and Γ_{41} are traction free in state 1 because the lower half-space is considered to be a vacuum. While in state 2, since there is no scatterer, the borders of Γ_{12} and Γ_{42} are not treated as traction free as they are part of the infinite halfspace. In addition, fields in both states are calculated in the isotropic media on the boundaries Γ_{11}/Γ_{12}, Γ_{21}/Γ_{22}, Γ_{31}/Γ_{32} and Γ_{41}/Γ_{42}.

On the side of incidence, two different cases are considered in state 1. The first case is that ultrasound impinges directly on the boundary Γ_{21} and propagates through the weld. The second case is that the ultrasound first impinges boundary on the Γ_{11}, and then the reflected wave impinges on boundary Γ_{21} and propagates further. Similarly, on the other side of the weld, the transmitted wave may first reflect on the boundary Γ_{41} and then terminate at the upper border. Or it may run directly to the upper border. Therefore, in state 1, reflected fields on the boundaries Γ_{11} and Γ_{41} are considered.

Let us assume a P wave being reflected on Γ_{11} as an example (the P wave reflection on Γ_{41} and the SV wave reflection can be dealt in a similar way). The incident plane P wave is then propagating within the isotropic part and can be defined by the following expression,

$$\boldsymbol{u}_p = A\left(\sin\gamma\boldsymbol{e}_1 + \cos\gamma\boldsymbol{e}_3\right)e^{ik_p\left(\sin\gamma\cdot x_1+\cos\gamma\cdot x_3\right)} = \frac{A}{k_p}\left(q\boldsymbol{e}_1 + h_p\boldsymbol{e}_3\right)e^{i\left(qx_1+h_px_3\right)} \tag{6}$$

As in Equation (1), A is the displacement amplitude of the P wave. q and h_p are wave numbers in the x_1 and x_3 directions, respectively. The wave number h_p satisfies $h_p = \sqrt{k_p^2 - q^2}$. The total displacement field (the reflected SV wave is neglected) becomes

$$\boldsymbol{u}_p^{\Sigma} = \boldsymbol{u}_p + \boldsymbol{u}_p^r = \frac{A}{k_p}\left(q\boldsymbol{e}_1 + h_p\boldsymbol{e}_3\right)e^{i\left(qx_1+h_px_3\right)} + R_p^r\frac{A}{k_p}\left(q\boldsymbol{e}_1 - h_p\boldsymbol{e}_3\right)e^{i\left(qx_1-h_px_3\right)} \tag{7}$$

where R_p^r is the reflection coefficient given by literature [12] $R_p^r = \dfrac{4q^2h_ph_s - \left(k_s^2 - 2q^2\right)^2}{4q^2h_ph_s + \left(k_s^2 - 2q^2\right)^2}$.

Reflected fields on the boundary Γ_{21} are not taken into account in the model because it is believed to give only a small contribution to the total field. As mentioned above in the forward ray tracing program, no mode conversion is considered in the calculations. The traction components on the boundary are given by $t_i = \sigma_{ij}n_j$, where n_j is the component of the inward directed normal $\boldsymbol{n}$ of the boundary. The stress σ_{ij} is determined by Hooke's law $\sigma_{ij} = C_{ijkl}\varepsilon_{kl}$. Here, C_{ijkl} is the stiffness matrix. The strain ε_{kl} is related to the displacement by $\varepsilon_{ij} = \frac{1}{2}\left(u_{i,j} + u_{j,i}\right)$. In these expressions, Einstein's summation convention is used.

4. Experimental Setup

Since neither mode conversion, viscous damping or any coarseness of the weld are included in the model at this stage, the intention with the validation is to identify necessary modifications in the experimental procedure or essential limitations in selecting weld, when the inverse problem in a later stage is to be addressed. The valida-

tion only intends to qualitatively validate the variation in anisotropic properties in the welding direction, in an ultrasonic pitch-catch perspective.

The experimental part of this project was performed by the Swedish Qualification Center (SQC) according to instruction (*i.e.* procedure) developed in collaboration with Chalmers. The purpose to collect data from real inspection objects with material structure defined by the welding specifications is to compare experimental data with theoretically calculated values. The three-dimensional welded volume is piecewise modeled by two dimensional line scans with variation of the predefined anisotropic orientation in each individual scan.

Collection of data has been performed by keeping one probe on a fixed distance from the weld centre line and moving the receiving probe perpendicular to the weld in line with the other probe (see **Figure 4**). This has been repeated along the weld with an increment of 4 mm. Further details of used equipment, welding specifications and information of the procedure to collect experimental are specified in [17].

5. Simulations

The output of the ultrasonic NDT system, expressed by the change in the electrical transmission coefficient, is calculated according to Equation (5), but in a discrete form on each boundary. The expression in Equation (5) is approximated by

$$\delta\Pi \approx \frac{i\omega}{4P}\sum_{\Gamma_{1,2,3,4}}\left(\boldsymbol{u}_2\cdot\boldsymbol{t}_1-\boldsymbol{u}_1\cdot\boldsymbol{t}_2\right)\Delta\Gamma \tag{8}$$

In the calculations, 100 discrete points are preset evenly along the fusion lines Γ_2 and Γ_3, with an interval of $\Delta\Gamma = 0.2214$ mm. The number of integration points on Γ_1 and Γ_4 is determined by

$$N = \frac{L}{\Delta\Gamma} \tag{9}$$

where L is the horizontal distance between the lower left corner (or the right corner) of the weld and the assumed furthest scanned position. In the simulation, the scan is supposed to cover from 10 mm to 108 mm along the upper surface of the base material, out of the weld. Therefore, $L = 101.5$ mm is adopted and then $N \approx 458$. In order to simulate the main lobe generated by a real ultrasonic transmitter, seven rays are adopted in each simulation. The simulation result of the receiver model is the superposition of the contributions from these rays. These seven rays are distributed evenly between $\pm\beta$ from the transmitter's nominal angle (*i.e.* prescribed angle [21]). To determine the parameter β in the simulation, an expression in Krautkrämer and Krautkrämer [24]

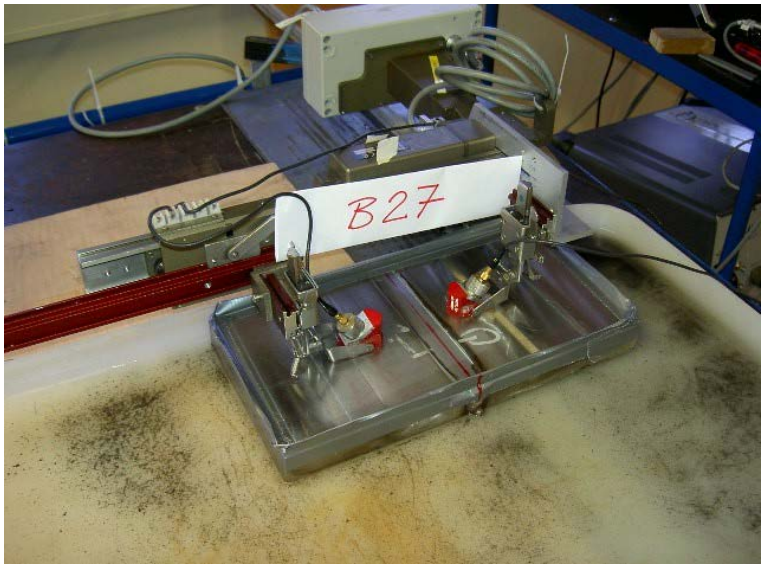

Figure 4. A picture of the experimental setup with the transmitter and receiver in a tandem configuration.

is referred to. It says that, for a circular piston oscillator, the divergence of the beam γ_α is approximately

$$\sin\gamma_\alpha = k_\alpha \frac{\lambda}{D} \tag{10}$$

In this expression, k_α is a factor whose value is supplied in a reference table to suit different sizes of the main lobe. α is the ratio of the sound pressure on the edge to the maximum, λ is the wavelength, and D is the aperture of the probe.

In this paper's calculation, k_α adopts the value of $k_\alpha = 0.37$. This corresponds to a main lobe whose sound pressure on the edge is about 84% of the maximum, almost 1.5 dB which correlates with the ray assumption in the model. For a P wave probe of 2.25 MHz, the wavelength is $l = 2.56$ mm $\left(C_p = 5770 \text{ m/s}\right)$. In the 2D transmitter model, the aperture of the transmitter is $D = 10$ mm and the calculation from Equation (10) gives $\gamma_p = 5.44$. Similarly, for an SV wave probe of 1 MHz, $\gamma_{sv} = 6.67$. Based on these values $b_p = b_{sv} = 6$ is chosen. Since the plane wave assumption is made in the modeling, the calculation of the displacement amplitude of a ray in the transmitter model is based on the far-field amplitude information at a fixed distance from the transmitter. Moreover, when a ray impinges on a boundary, only points lying in an area with a length of l around the intersection by the ray and the boundary is considered influenced by the ray. Points outside this area are not affected by the ray. Therefore, fields are not calculated for these points. Experiences made from the simulations revealed that $l = 12$ mm was a good choice. To simulate different sections in a C-scan display, a different random variation with a maximum of ±5% is introduced in the grain orientations in each run of the calculation. The intention is to validate the degree of variation along the welding direction and qualitatively compare with the C-scan plots achieved from the experiments. Grains with an orientation of 90˚ to the x_1 axis (mostly in the center of a weld, as shown in **Figure 1(c)**) are free from this random change because they are believed to be close to the actual situation.

Two different groups of simulations are performed for the same weld model, one for the P wave and another for the SV wave. In each group, three different cases are simulated. Parameters for each case are listed in **Table 1** with the transmitter positions defined in **Figure 5**. The experiments were set up under the same conditions as listed in **Table 1** and executed at SQC. Simulation results, as well as the corresponding experimental results are shown in **Figures 6-17**. **Figure 6**, **Figure 8** and **Figure 10** are simulation results for the *P* wave. They correspond to a transmitter position of −18 mm, −33 mm and −67 mm (along the x_1 axis), respectively. For the SV wave, **Figure 6**, **Figure 12** and **Figure 14** are the simulation results of three different transmitter positions of −18 mm, −24 mm and −36 mm, respectively. Transmitter positions in the model's coordinate system are shown in **Figure 3**. In each figure, subplot (a) is the plot of one of the ray tracing runs. There are totally nine runs because of the adoption of nine groups of randomness in the grain orientations. Here only the last group of the simulation results among the nine runs is displayed for each simulation shown in subplot (a). Subplot (b) is the output of the receiver model corresponding to the different randomness taken in grain orientations in the simulations. Subplot (c) is also the output of the receiver model, but depicted in a surface plot (*i.e.* a simulated C-scan). The x_2 axis in this subplot indicates different sections corresponding to a C-scan, and the subplot (c) shows a fluctuation in the signal response due to the randomly variation in grain direction in each individual line scan. To facilitate the comparison, the simulation results of the P wave receiver model in **Figure 6**, **Figure 8** and **Figure 10** are first normalized with the maximum in **Figure 6(b)**, and then transformed into decibel from 0 to −20 dB. The figures of the SV wave calculation are dealt with in a similar manner, but normalized with the maximum in **Figure 12(b)**.

6. Validations

Experimental results of ultrasonic C-scan are displayed in **Figure 7**, **Figure 9** and **Figure 11** for the P wave.

Table 1. Experimental parameters on a specific weld.

Wave type	Probe angle (˚)	Probe frequency (MHz)	Transmitter position 1 (mm)	Transmitter position 2 (mm)	Transmitter position 3 (mm)
P	60	2.25	−18	−33	−67
SV	45	1	−18	−24	−36

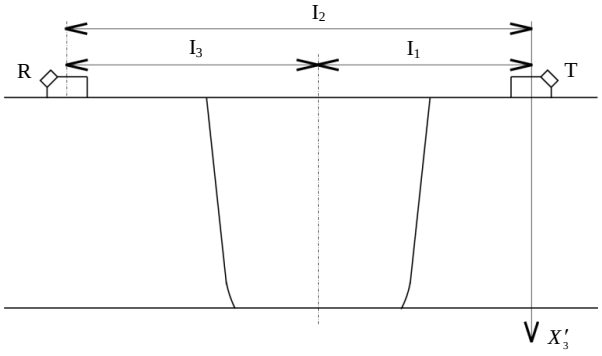

Figure 5. The relationship of the coordinate systems used in the simulation and the experiment.

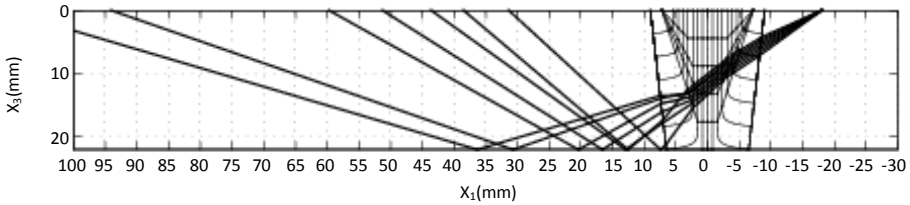

(a)

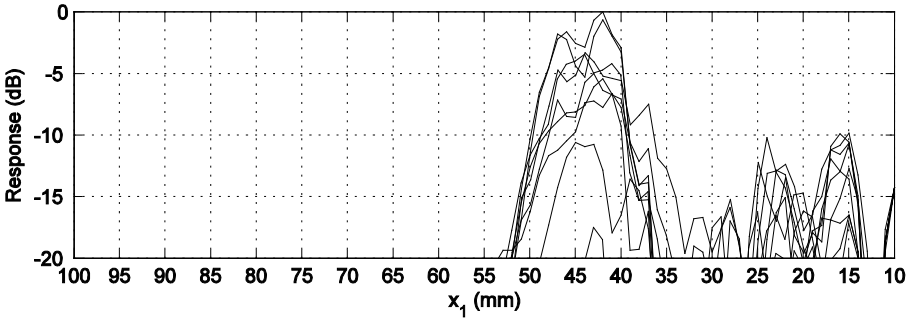

(b)

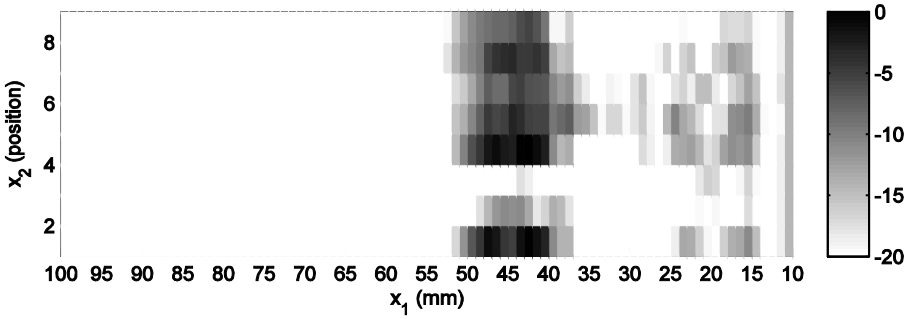

(c)

Figure 6. Simulation result of the *P* wave (probe position is −18 mm). (a) Ray tracing plot; (b) Receiver model output 1; (c) Receiver model output 2.

Figure 13, **Figure 15** and **Figure 17** are experimental results of the SV wave. In the experiments, a new coordinate system is adopted so as to facilitate the operations, which is shown in **Figure 5**. Obviously, this is different from the coordinate system used in the model shown in **Figure 3**. In each run, the distance l_1 of the transmitter from the center of the weld is first determined. Then, the position of the transmitter is taken as the origin. The receiver scans a certain distance l_2 from the transmitter, in the negative direction. This can be observed in

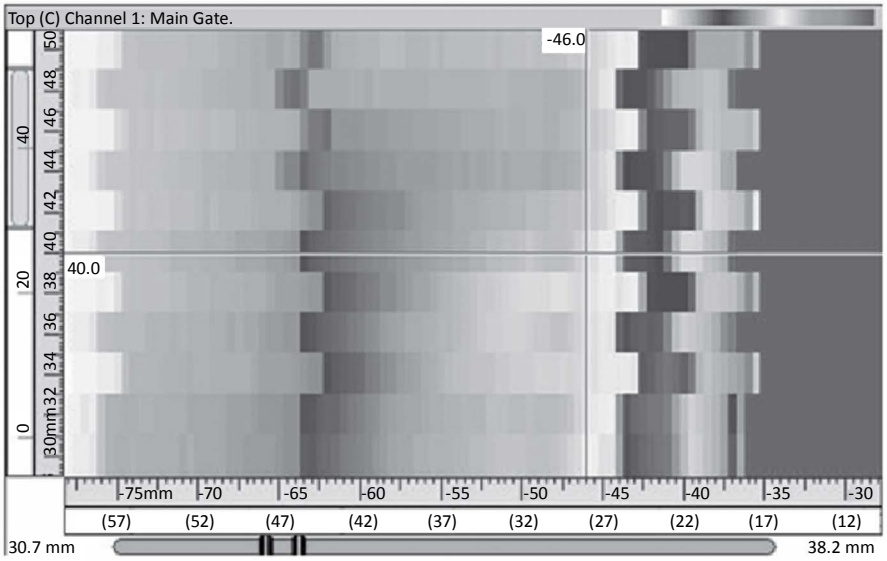

Figure 7. Experimental result of the *P* wave (probe position is −18 mm).

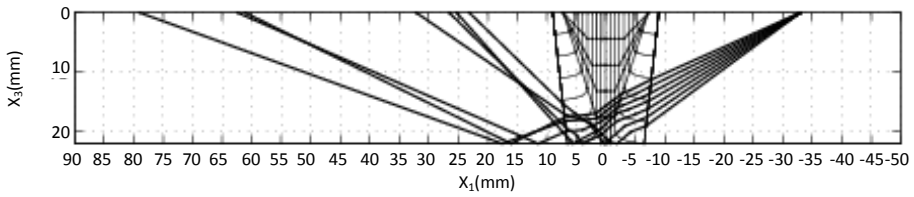

(a)

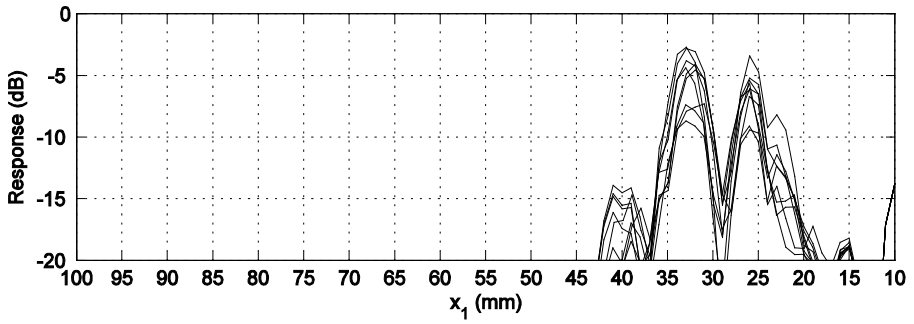

(b)

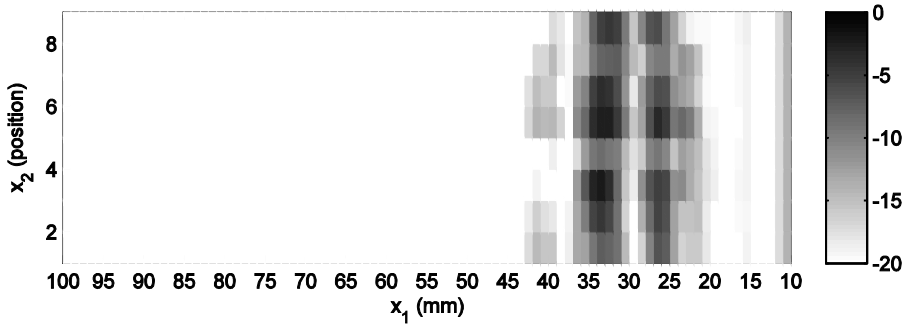

(c)

Figure 8. Experimental result of the *P* wave (probe position is −33 mm). (a) Ray tracing plot; (b) Receiver model output 1; (c) Receiver model output 2.

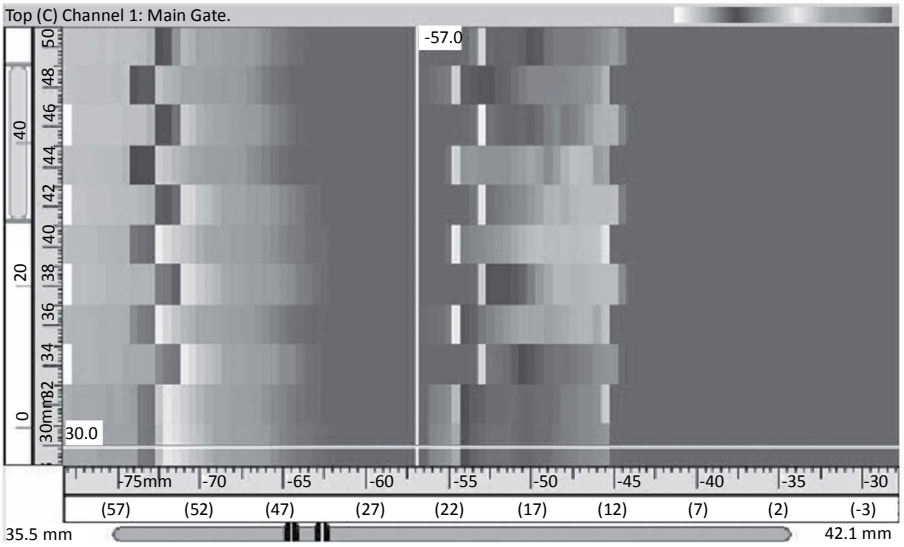

Figure 9. Experimental result of the *P* wave (probe position is −33 mm).

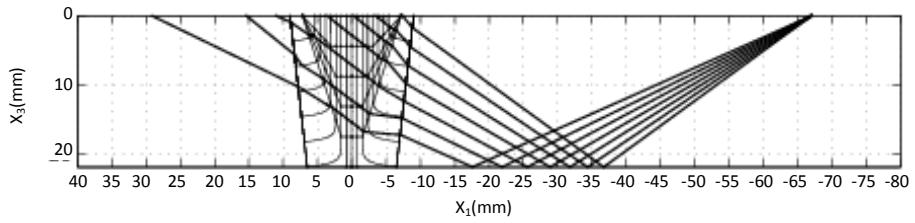

(a)

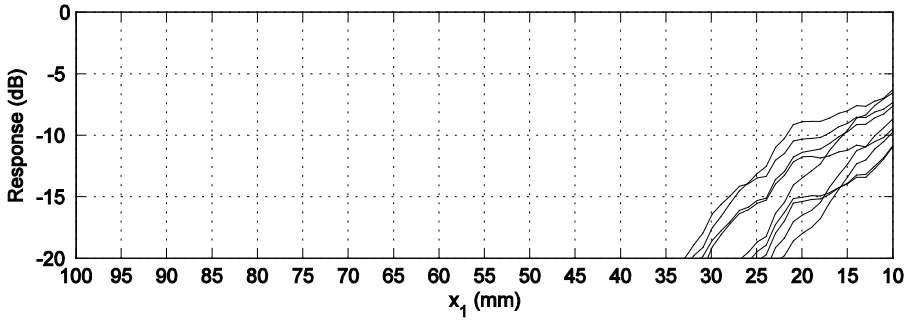

(b)

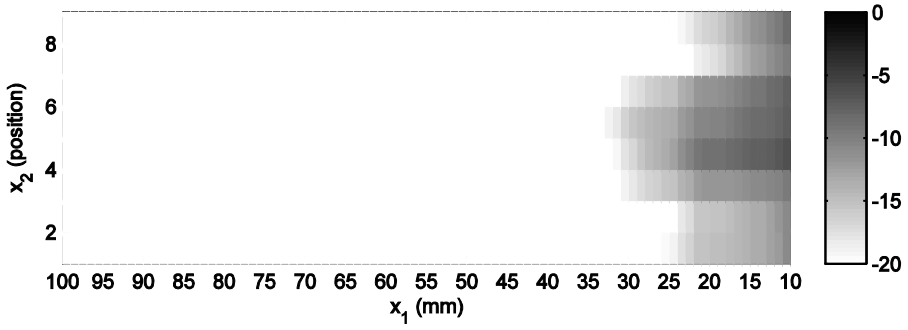

(c)

Figure 10. Simulation result of the *P* wave (probe position is −67 mm). (a) Ray tracing plot; (b) Receiver model output 1; (c) Receiver model output 2.

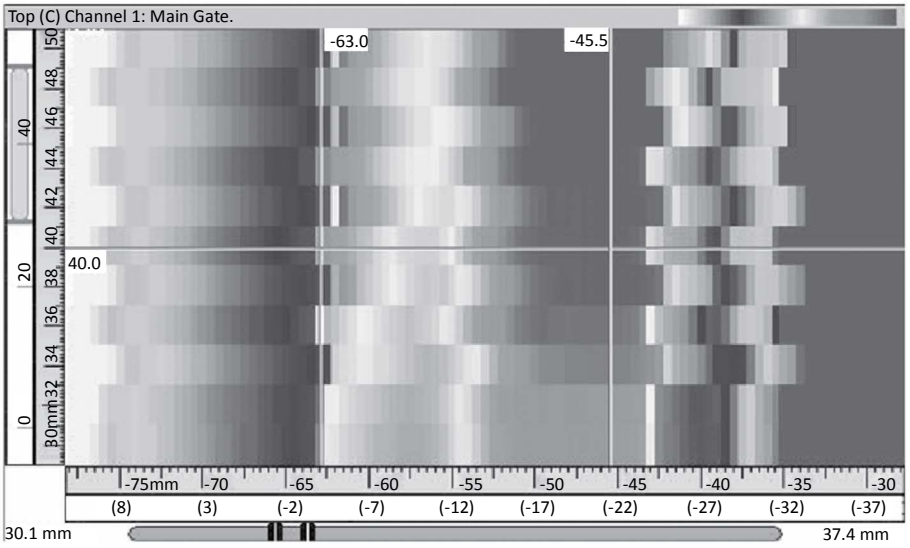

Figure 11. Experimental result of the *P* wave (probe position is −67 mm).

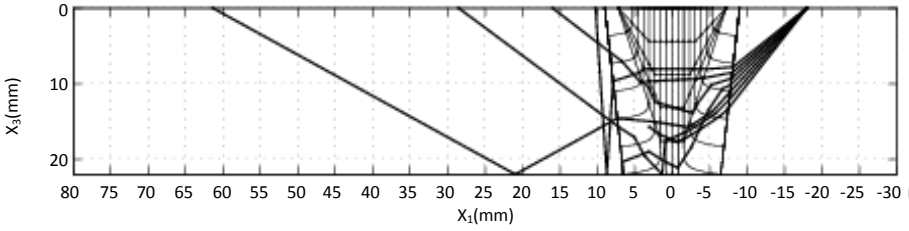

(a)

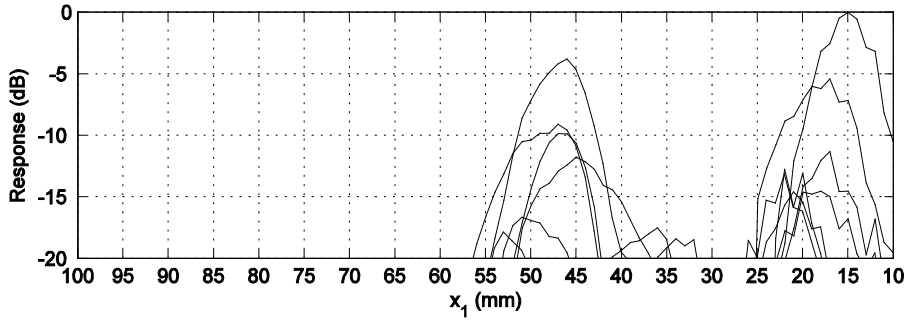

(b)

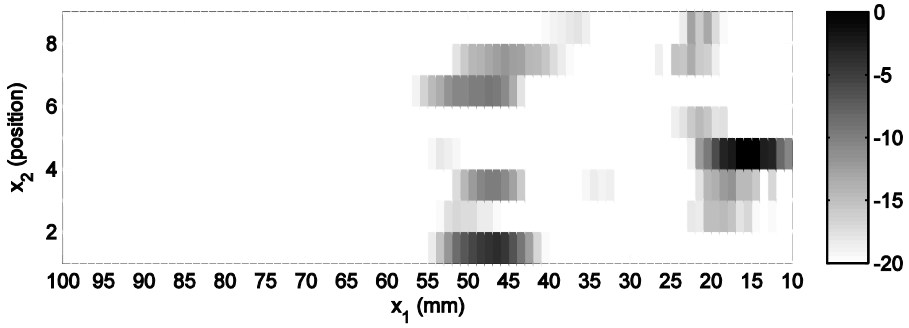

(c)

Figure 12. Simulation result of the SV wave (probe position is −18 mm). (a) Ray tracing plot; (b) Receiver model output 1; (c) Receiver model output 2.

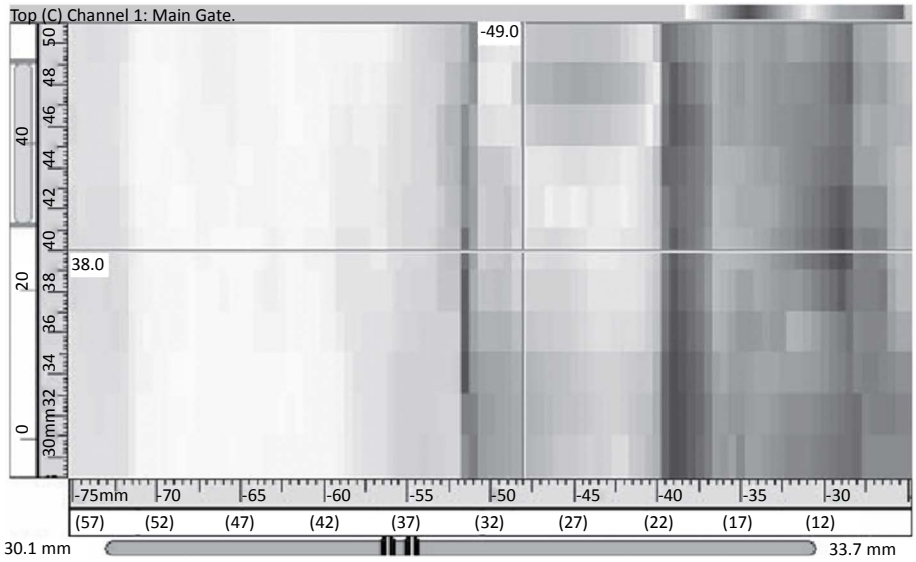

Figure 13. Experimental result of the SV wave (probe position is −18 mm).

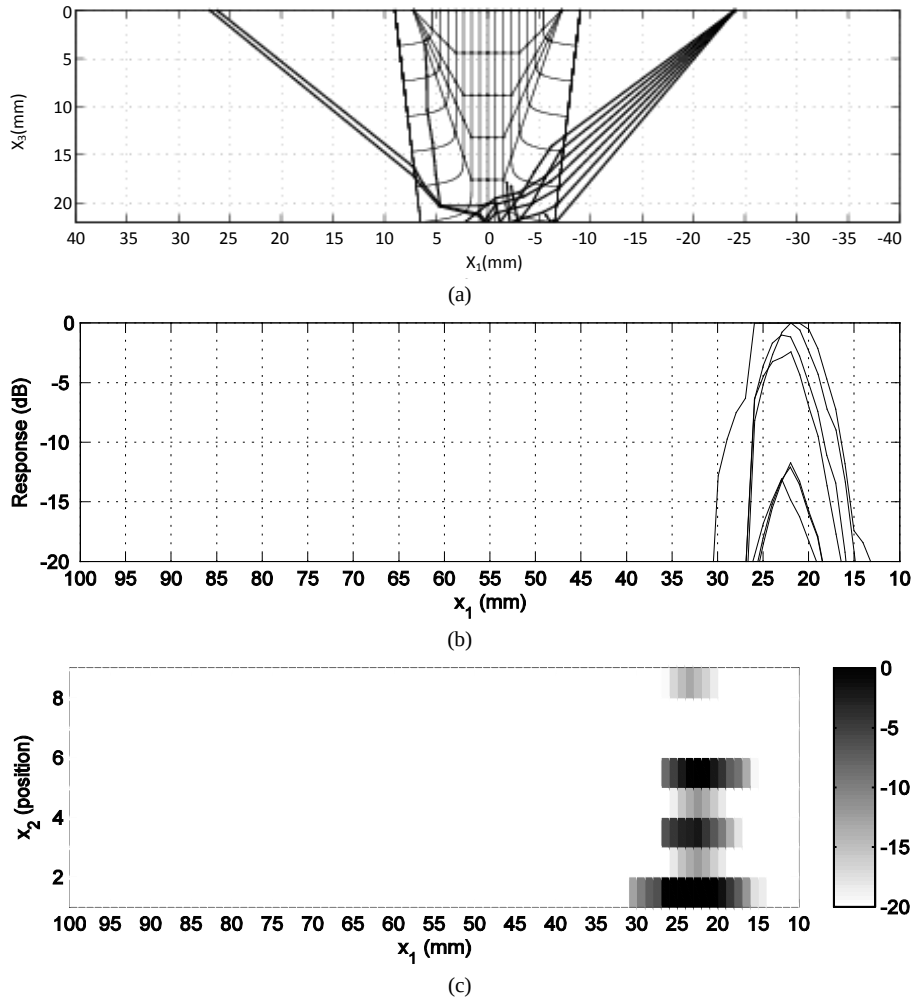

Figure 14. Simulation result of the SV wave (probe position is −24 mm). (a) Ray tracing plot; (b) Receiver model output 1; (c) Receiver model output 2.

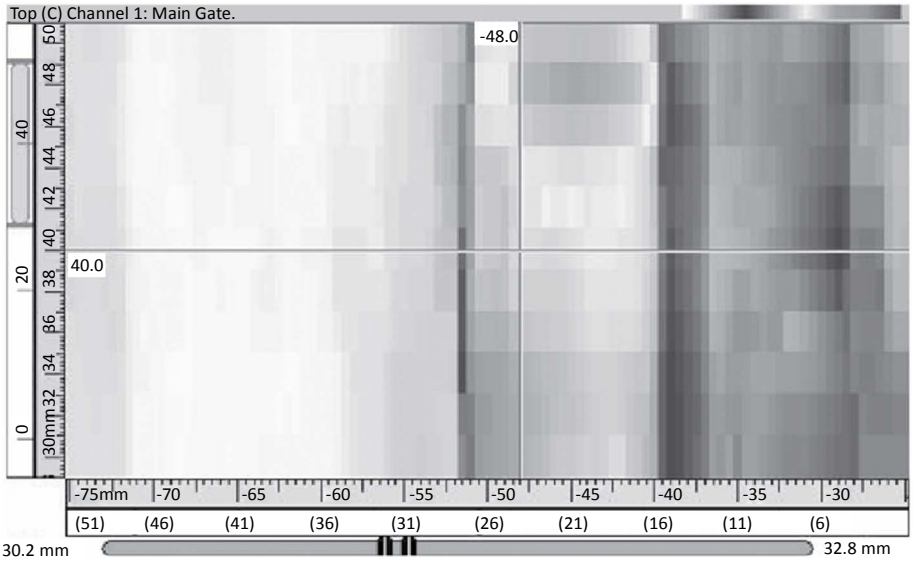

Figure 15. Experimental result of the SV wave (probe position is −24 mm).

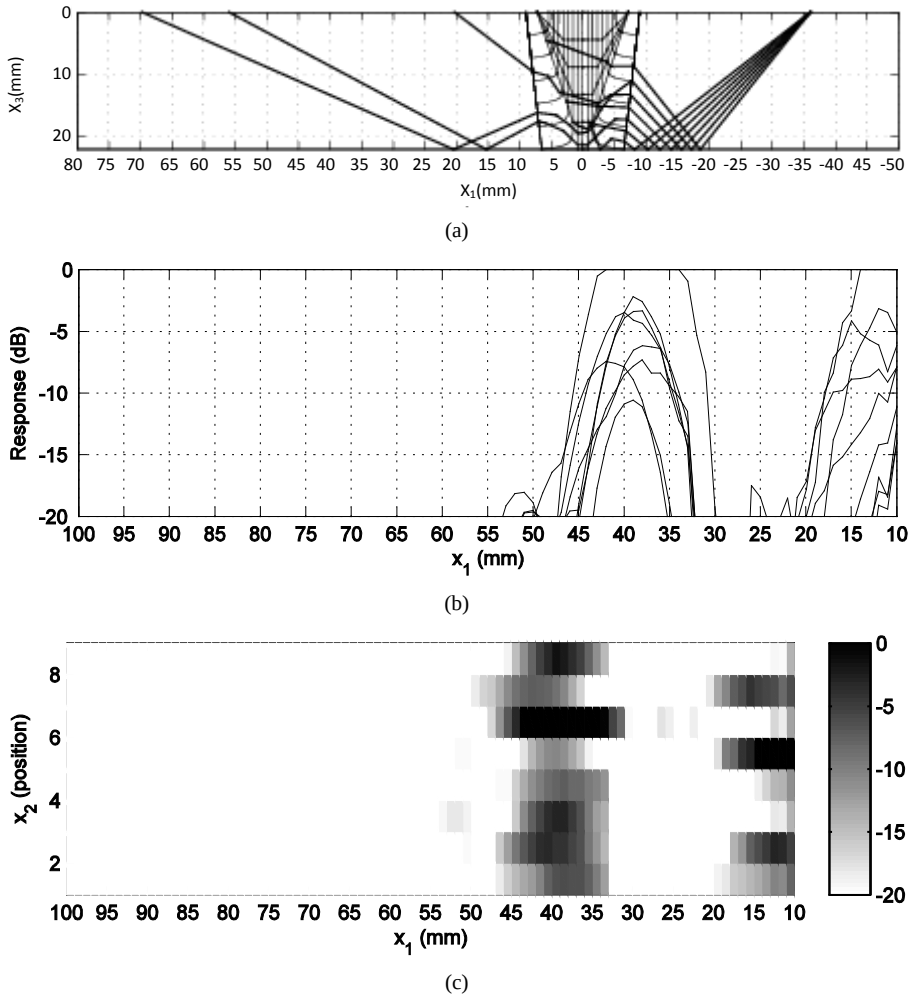

(a)

(b)

(c)

Figure 16. Simulation result of the SV wave (probe position is −36 mm). (a) Ray tracing plot; (b) Receiver model output 1; (c) Receiver model output 2.

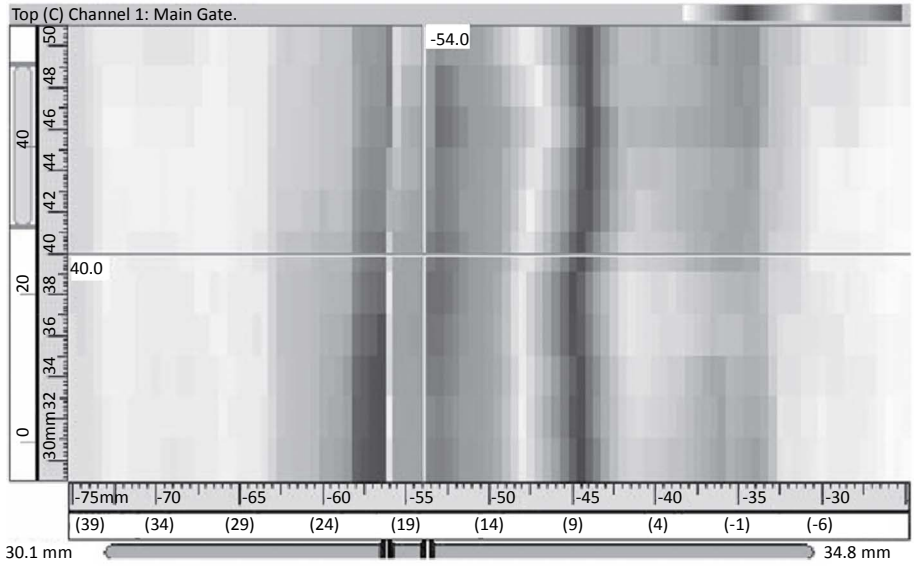

Figure 17. Experimental result of the SV wave (probe position is −36 mm).

each figure of the experimental result. The scales of the abscissa on the first line are all negative, from about −30 mm to about −80 mm. For the sake of making a better comparison between the simulation results and the experimental outputs, a coordinate transformation is executed as a post processing. With this coordinate transformation, the coordinate of the receiver is switched to be associated with the weld center, rather than the transmitter. This is realized by $l_3 = l_2 - l_1$, which is illustrated in **Figure 5**. After the transformation, a new abscissa whose scales are in parentheses is arranged in each figure of the experimental output, under the original abscissa. The experimental data are evaluated with the software UltraVision and displayed in gray palette. This causes the loss of color information. Therefore, an approximate peak position is labeled in each experimental result as a remedy.

When considering the simulation results, it is observed from the subplots (a) that the *P* wave is less affected by the weld than the SV wave is. For the *P* wave, all rays can reach the upper surface of the weld model, while some of the SV rays terminate in the weld without further transmission. In addition, some of the SV rays behave irregularly when propagating through the weld model. This phenomenon implies that SV waves are more sensitive to the grains' crystal orientations, which coincides with common knowledge of the SV wave propagation in an anisotropic medium. On the other hand, this indicates that the weld model has more influence on the SV wave propagation than on corresponding *P* wave. Therefore, the partition of the weld, as well as the setup of the boundaries between sub-regions is essential for a successful simulation, especially for the SV wave. In addition, mode conversion is not considered in the modeling, which also possibly makes the number of transmitted SV waves too few.

The receiver model presents the distribution of the signal in subplots (b) and (c). A simulated C-scan plot is implemented by the adoption of randomness in the modeled grain orientations. It is noticed that the distribution of the receiver model's output does not agree with that of the ray tracing plot perfectly. In **Figure 6(a)**, rays occupy the area almost from 30 mm to 100 mm along the upper boundary, while in **Figure 6(b)** and **Figure 6(c)**, the main peak appears approximately from 37 mm to 52 mm. In **Figure 8(a)**, rays are distributed over the area between 22 mm and 80 mm. But in **Figure 8(b)** and **Figure 8(c)**, double peaks cover the area between 20 mm and 37 mm. Similar situations also occur in **Figure 12** and **Figure 16**. Good agreement between the ray tracing plot and the receiver model output can only be observed in **Figure 10** and **Figure 14**. In **Figure 10(a)**, rays are terminated between 10 mm and 30 mm. In the corresponding receiver model output, a similar result is achieved. In **Figure 14**, the only two transmitted rays stop around 27 mm. The receiver model output covers approximately the same place. This phenomenon is believed to be caused by the application of the reciprocity principle. According to the reciprocity relationship, the modeled receiver is the same as the modeled transmitter. Thus, for a 60˚ transmitter, the same type of receiver is supposed. Consequently, only the waves propagating around this angle contributes to the receiver's main output.

When considering the experimental outputs, it is found that since the scans only cover an interval of 20 mm

(from 30 mm to 50 mm) along the weld, marked difference among the sections of a C-scan cannot be noticed for the *P* wave results. But for the SV wave results, difference among the sections of a C-scan can be observed, e.g. in **Figure 13** and **Figure 15**. In evaluating the *P* wave data, detailed analyses are always required to discern the true signal from the one caused by mode conversion because the signal strength caused by mode conversion is usually much stronger. This is clarified in **Figure 7**, **Figure 9** and **Figure 11**, in which the dark areas on the rightmost side are believed to be caused by mode conversion. In addition, in **Figure 11**, only the left cursor indicates the requested peak signal position. The right cursor is an indication of the mode conversion.

If the receiver model's output 2 and the C-scan plot of the experimental result are compared, the result is not very satisfying. Even if only the maximum response position is considered, there is a difference between the simulation result and the experimental result. For the *P* wave experiments, in **Figure 6(c)**, the maximum of the receiver model output is between 40 mm and 50 mm. However, the experimental result presents the maximum around 28 mm in the C-scan display. If **Figure 8(c)** and **Figure 9** are compared, different peak forms can be noted though the areas of maximal signal overlap. **Figure 10(b)** displays a tendency of having the maximal signal in the weld, which is shown in **Figure 11**, while quantitative information is missed. This is caused by the limitation of the receiver model, which always starts scans from 10 mm. For the SV wave experiments, similar disparity can be located also. For example in **Figure 13**, the experiment result indicates clearly that the maximal output is distributed in the area from 26 mm to 33 mm, while in the simulation result of the receiver model, this tendency is quite vague. In **Figure 14(c)**, only some sections display the same distribution area of the maximal signal as in **Figure 15**. The differences between **Figure 16(c)** and **Figure 17** can partially be attributed to the imperfectness of the weld model and the ray tracing model. Another possibility is the influence of mode conversion that is mentioned above. In the modeling and simulations, mode conversion is not included. In the experiments, the recorded result is a comprehensive action of all the factors that also includes effects such as mode conversion. This could to some extent be filtered out by thorough time gating of the received signal.

7. Concluding Remarks

A receiver model for a 2D ultrasonic ray tracing program is proposed in this paper. It is based on Auld's electromechanical reciprocity principle. Two different states are employed in the calculation. The first state represents the actual testing situation. The "scatterer" is then present and the transmitter works at the same position as in the actual measurement. For the second state, no "scatterer" is present and the transmitting probe is positioned on the other side of the weld (receiving side). Numerical calculations are performed for both *P* and SV waves. In each case, three different transmitter positions are used. The distribution of the detected signal then is presented by the receiver model. Simulation results are compared with the C-scan plots from the experiments. In some of these cases there are obvious differentiations. This involves a number of possibilities due to deviations between the idealized mathematical model of the NDT inspection situation and the actual experimental data collected by conventional equipment in an industrial environment. Beside the previous mentioned exclusion of viscous damping in the model also the simplification of the texture in the weld could be part of the explanation. Another plausible cause could be inaccuracies in the collection procedure of experimental data (described in [17]). The latter also indicates on how essential the time-gating procedure is when, as in this case, mode conversion is excluded in the model.

A point achieved from the validating process and the comparison is that the simulation presents the maximum received signal at a point, while the experiments present the maximum output over an area. Hence, the resolution of the experimental results is vital to the evaluation of the later inversion calculation. How to obtain a reliable result from the experiments and then apply it to the comparison with the forward simulation result is a new challenge.

Acknowledgements

This project is financed by the Swedish Qualification Center (SQC). Kjell Högberg, Gunnar Werner and Jeanette Gustafsson from SQC provided great help in the experiments. This is gratefully acknowledged.

References

[1] Ogilvy, J.A. (1985) *British Journal of NDT*, **27**, 13-21.

[2] Fellinger, P., Marklein, R., Langenberg, K.J. and Klaholz, S. (1995) *Wave Motion*, **21**, 47-66. http://dx.doi.org/10.1016/0165-2125(94)00040-C

[3] Schmitz, V., Walte, F. and Chakhlov, S.V. (1999) *NDT & E International*, **32**, 201-213. http://dx.doi.org/10.1016/0165-2125(94)00040-C

[4] Spies, M. (2000) *NDT & E International*, **33**, 155-162. http://dx.doi.org/10.1016/S0963-8695(99)00036-5

[5] Moysan, J., Apfel, A., Corneloup, G. and Chassignole, B. (2003) *International Journal of Pressure Vessels and Piping*, **80**, 77-85. http://dx.doi.org/10.1016/S0308-0161(03)00024-3

[6] Spies, M. (2004) *Ultrasonics*, **42**, 213-219.

[7] Jeong, H. (2009) *NDT & E International*, **42**, 210-214. http://dx.doi.org/10.1016/j.ndteint.2008.09.010

[8] Köhler, B., Müller, W., Spies, M., Schmitz, V., Zimmer, A., Langenberg, K.-J. and Metzko, U. (2006) *AIP Conference Proceedings*, **820**, 57-64. http://dx.doi.org/10.1063/1.2184511

[9] Nakahata, K., Hirose, S., Schubert, F. and Köhler, B. (2009) *Journal of Solid Mechanics and Materials Engineering*, **3**, 1256-1262. http://dx.doi.org/10.1299/jmmp.3.1256

[10] Baek, E. and Yim, H. (2011) *NDT & E International*, **44**, 571-582. http://dx.doi.org/10.1016/j.ndteint.2011.05.011

[11] Connolly, G.D., Lowe, M.J.S., Rokhlin, S.I. and Temple, J.A.G. (2010) *The Journal of the Acoustical Society of America*, **127**, 2802-2812. http://dx.doi.org/10.1121/1.3372724

[12] Ogilvy, J.A. (1985) *NDT International*, **18**, 67-77. http://dx.doi.org/10.1016/0308-9126(85)90100-2

[13] Chassignole, B., El Guerjouma, R., Ploix, M.-A. and Fouquet, T. (2011) *NDT & E International*, **43**, 273-282. http://dx.doi.org/10.1016/j.ndteint.2009.12.005

[14] Gueudre, C., Le Marrec, L., Moysan, J. and Chassignole, B. (2009) *NDT & E International*, **42**, 47-55. http://dx.doi.org/10.1016/j.ndteint.2008.07.003

[15] Kolkoori, S.R., Rahaman, M.-U., Chinta, P.K., Kreutzbruck, M. and Prager, J. (2012) *AIP Conference Proceedings*, **1430**, 1227-1234.

[16] Liu, Q. and Wirdelius, H. (2007) *NDT & E International*, **40**, 229-238. http://dx.doi.org/10.1016/j.ndteint.2006.10.004

[17] Wirdelius, H., Persson, G., Hamberg, K. and Högberg, K. (2008) ULiAS 4—Experimental Validation of a Software that Models Ultrasonic Wave Propagation through an Anisotropic Weld. SKi Report: 05.

[18] Auld, B.A. (1979) *Wave Motion*, **1**, 3-10. http://dx.doi.org/10.1016/0165-2125(79)90020-9

[19] Tan, T.H. (1977) *Journal of the Acoustical Society of America*, **61**, 928-931. http://dx.doi.org/10.1121/1.381393

[20] Kino, G.S. (1978) *Journal of Applied Physics*, **49**, 3190-3199. http://dx.doi.org/10.1063/1.325312

[21] Boström, A. and Wirdelius, H. (1995) *Journal of the Acoustical Society of America*, **97**, 2836-2848. http://dx.doi.org/10.1121/1.411850

[22] Eriksson, A.S., Mattsson, J. and Niklasson, A.J. (2000) *NDT & E International*, **33**, 441-451. http://dx.doi.org/10.1016/S0963-8695(00)00016-5

[23] Achenbach, J.D. (1973) Wave Propagation in Elastic Solids. North-Holland, Amsterdam, Ch. 6, 6.5.

[24] Krautkrämer, J. and Krautkrämer, H. (1990) Ultrasonic Testing of Materials. Springer-Verlag, Berlin, Ch. 4.4. http://dx.doi.org/10.1007/978-3-662-10680-8

Journal of Modern Physics, 2014, 5, 1202-1222
Published Online July 2014 in SciRes. http://www.scirp.org/journal/jmp
http://dx.doi.org/10.4236/jmp.2014.513121

Scientific Research

An Optimization Technique for Inverse Crack Detection

Håkan Wirdelius

Department of Materials and Manufacturing Technology, Chalmers University of Technology, Göteborg, Sweden
Email: hakan.wirdelius@chalmers.se

Received 2 May 2014; revised 29 May 2014; accepted 21 June 2014

Abstract

Any attempts to apply techniques that are based on indirect measurements of parameters that are believed to correlate to any material properties (or state) in an in-line situation must by necessity identify a mathematical model of this relationship. The most conventional approach is to use some empirically based model. If the analysis instead is based on an analytical model of a physical explanation, this trainee period can be minimized and the system is more dynamic and less sensitive to changes within the chain of production. A numerical solution to the inverse problem of ultrasonic crack detection is in this case investigated. This solution is achieved by applying optimization techniques to a realistic model of the ultrasonic defect detection situation. This model includes a general model of an ultrasonic contact probe working as transmitter and/or receiver and its interaction with the defect. The inverse problem is reduced to minimization of a nonlinear least squares problem and is performed with a quasi-Newton algorithm consisting of a locally convergent SVD-Newton method combined with a backtracking line search algorithm. The set of synthetic data the model is fitted with are generated both by numerical integration and with the two-dimensional stationary-phase method while the forward solver in the optimization procedure is based on the latter. In both these cases, the convergence, in terms of numbers of iterations, is sufficient when the initial guess is reasonably close.

Keywords

Inverse Problem, Ultrasonic NDT, Quasi-Newton Algorithm

1. Introduction

Nondestructive testing (NDT) has many industrial applications with increasing use in reliability investigations of materials and components. New and stronger demands on safety, reliability and optimization have made it im-

proper to just detect a flaw or the presence of inferior material properties. The need of quantitative information has given rise to more fundamental approaches to nondestructive evaluation (NDE) with growing emphasis on theoretical modeling of the ultrasonic inspection situation.

In the previous research, we have developed a complete mathematical model of the ultrasonic NDT situation (UTDefect) which has been incorporated into different simulation software (SUNDT and simSUNDT). The development has been ongoing since almost twenty years and has been validated and described in a numerous journal and conference contributions (see e.g. [1]-[3]). The model includes a general model of an ultrasonic contact probe working as transmitter and/or receiver and the interaction of the ultrasound with the defect. This realistic model offers the possibility of avoiding, or at least reducing, time-consuming and costly experimental work. It can also be useful in the design of inspection routines as it gives an estimate of weather a postulated defect can be detected or not.

The practical situation when ultrasonic NDE is used is in fact an inverse problem, *i.e*. based on the signals from transmitting and receiving probes an interpretation is performed (see **Figure 1**). This interpretation is then often based on earlier experiences or by comparing with experimental work or computer simulations. Analytical solutions to the inverse problem have up today only been found for very simple situations and are often based upon a linearization of the inverse problem performed by the Born approximation (an extensive review discussing this is available by Bates *et al*. [4]). This linearization limits the applicability since it, at least in principle, restricts the problem to weak penetrable scatterers or low frequencies. Even so this assumption has actually been successfully applied for more complex ultrasonic situations [5]. A slightly different approach, still based on the Born approximation, has been to retrieve a large amount of point source information and address the inversion by various time domain back propagation techniques (Synthetic Aperture Focussing Techniques described in e.g. [6] [7]). Degtyar *et al*. [8] introduced an inversion procedure based on a nonlinear least-squares method to determine elastic constants from group or phase velocity data in orthotropic and transversely isotropic materials. Corresponding approach has also been used in order to retrieve viscoelastic material properties based on ultrasonic experimental data (Castaings *et al*. [9] [10]).

To investigate its possibility, we approach the inverse problem by applying optimization techniques to our previous general model of the ultrasonic inspection in the present paper. This choice of technique is based on a paper by Björkberg and Kristensson [4] where an optimization technique is successfully used to numerically solve an electromagnetic inverse problem. This problem originates from geophysical prospecting applications and differs from ours in the sense that all components of the scattered field is available by measurements from bore holes in the ground. In ultrasonic NDT situations, only two electric pulses in time, representing the incoming and scattered field, respectively, are the available information from the transmitter and receiver.

The aim of this paper is to investigate if it is possible to numerically solve the inverse problem that occurs in ultrasonic crack detection, by minimizing the mean-square error between the ultrasonic model and corresponding data.

The plan of the present paper is the following. In the first section, we briefly discuss the model of the NDT situation previously presented by Boström and Wirdelius [11] [12]. This includes the probe model, the interaction

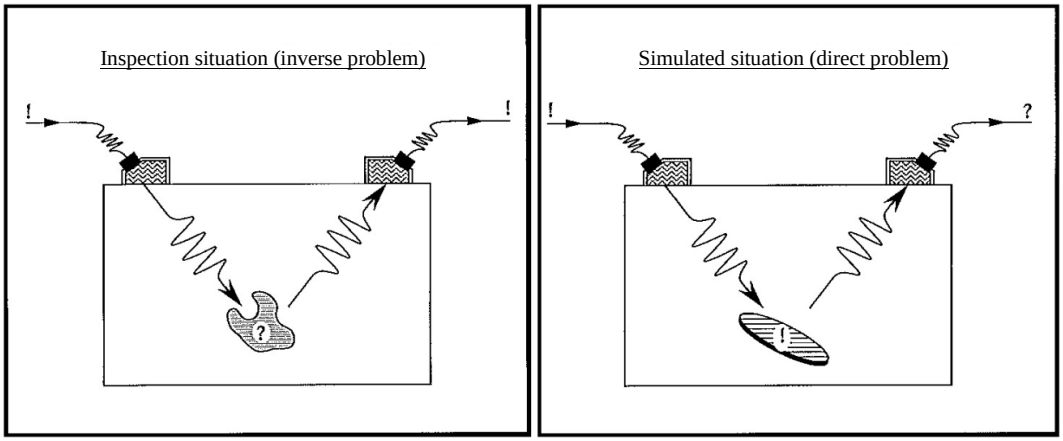

Figure 1. Simulated situation versus inspection situation.

of the probe field with the defect and the reciprocity argument that handles the action of the probe when it is acting as a receiver. The next section presents the optimization technique that is used and is followed by a section with numerical results based on previous sections. Finally, we give some concluding remarks and suggestions for future considerations.

2. Model of the Ultrasonic Inspection

The governing linearized equations for wave propagation in an elastic medium are the equation of motion, Hooke's law and the strain-displacement relation. If time harmonic conditions are assumed (time factor $e^{-i\omega t}$ is suppressed) these three relations can be combined into the elastodynamic equation of motion governing the displacement field $\boldsymbol{u}$

$$k_p^{-2}\nabla\nabla\cdot\boldsymbol{u}-k_s^{-2}\nabla\times\nabla\times\boldsymbol{u}+\boldsymbol{u}=0 \tag{1}$$

where

$$\begin{cases}k_p^2=\rho\omega^2/(\lambda+2\mu)\\ k_s^2=\rho\omega^2/\mu\end{cases}$$

are the compressional and shear wave numbers, respectively (ρ is the density, λ and μ are the Lamé constants of the elastic half-space).

The total displacement field is given by the sum of the incident field $(\boldsymbol{u}^i)$ and the scattered field $(\boldsymbol{u}^s)$

$$\boldsymbol{u}=\boldsymbol{u}^i+\boldsymbol{u}^s \tag{2}$$

Let us expand the incident field in terms of regular spherical partial vector waves $(\mathrm{Re}\,\boldsymbol{\Psi}_n)$ and the scattered field in corresponding outgoing spherical partial vector waves $(\boldsymbol{\Psi}_n)$, *i.e.*

$$\begin{cases}\boldsymbol{u}^i=\sum_n a_n\,\mathrm{Re}\,\boldsymbol{\Psi}_n\\ \boldsymbol{u}^s=\sum_n f_n\boldsymbol{\Psi}_n\end{cases} \tag{3}$$

Then it is possible to find a linear relationship between the expansion coefficients for the incident and scattered field and this entity is known as the transition matrix $\boldsymbol{T}$

$$f_n=\sum_{n'}T_{nn'}a_{n'} \tag{4}$$

All information about the scatterer is contained in its transition matrix and there are various methods of evaluating it. Most common is to use the null-field approach [12] but in our case with a prescribed open penny-shaped crack it is more convenient to use an integral equation method previously described by Boström and Eriksson [13]. The $\boldsymbol{T}$ matrix of a spherical cavity is obtained by separation-of-variables.

We now introduce a coordinate system as in **Figure 2** with the z axis normal to the scanning surface and the x axis chosen so that the probe beam is emitted into the third quadrant of the xz plane with the angle γ with the negative z axis. In **Figure 2**, we have introduced $\hat{k}=-\cos\gamma\hat{z}-\sin\gamma\hat{x}$ as the propagation direction and $\hat{v}$ is the S wave polarization direction (with $\hat{v}\cdot\hat{k}=0$ and $\hat{x}$, $\hat{y}$ and $\hat{z}$ as the unit vectors). We choose $\hat{v}_{SH}=\hat{y}$ and $\hat{v}_{SV}=\hat{v}_{SH}\times\hat{k}=\sin\gamma\hat{z}-\cos\gamma\hat{x}$ in order to distinguish between horizontally and vertically polarized shear waves.

In order to model a probe of specific type and angle, the traction vector corresponding to a plane wave of identical type and angle is taken as boundary conditions on the surface of the elastic half-space. Now let the contact probe be characterized by this prescribed traction on the surface of the elastic half-space and assume that this area, corresponding to the acting probe, is elliptic or rectangular.

We then get

$$\boldsymbol{t}=\begin{cases}Agi\mu k_p\left[\left(k_s^2/k_p^2-2\sin^2\gamma\right)\hat{z}+\delta\sin2\gamma\hat{x}\right]e^{-ik_p x\sin\gamma} & \text{P probe}\\ Agi\mu k_s\left[\sin2\gamma\hat{z}-\delta\cos2\gamma\hat{x}\right]e^{-ik_s x\sin\gamma} & SV\text{ probe}\\ Agi\mu k_s\left[\delta\cos\gamma\hat{y}\right]e^{-ik_p x\sin\gamma} & SH\text{ probe}\end{cases} \tag{5}$$

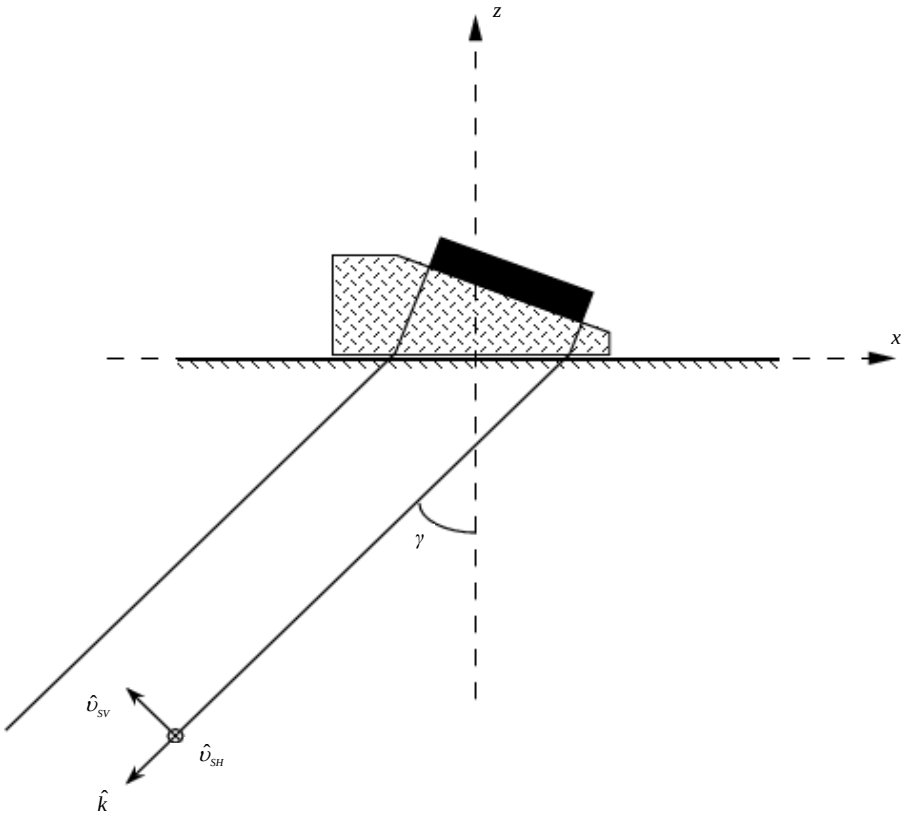

Figure 2. Geometry of the probe with definition of coordinate system and propagation/polarization directions.

beneath the probe and $\boldsymbol{t} = \boldsymbol{0}$ elsewhere (*A* represents the amplitude). The function $g = g(x, y)$ and the constant $\delta \in [0,1]$ enables reduction of edge effects and varied coupling respectively (for further details see [14]). In order to solve this boundary value problem and combine the incident field with the transition matrix formulation, we make following ansatz for the displacement field radiated from the probe

$$\boldsymbol{u}(\boldsymbol{r}) = \sum_{j=1}^{3} \int_{C_-} \mathrm{d}\hat{\gamma} \xi_j(\hat{\gamma}) \boldsymbol{\phi}_j(\hat{\gamma}; \boldsymbol{r}) \tag{6}$$

with the plane vector wave functions, $\boldsymbol{\phi}_j(\hat{\gamma}; \boldsymbol{r})$, defined as in Boström *et al.* [15], and with the coefficients $\xi_j(\hat{\gamma})$ as unknowns. Then the corresponding traction on the surface can be written as

$$\boldsymbol{t}(\boldsymbol{u})\big|_{z=0} = \sum_{j=1}^{3} \mathrm{d}\hat{\gamma} \xi_j(\hat{\gamma}) \boldsymbol{t}_j(\phi_j)\big|_{z=0} \tag{7}$$

which is identified as a 2D Fourier transform with corresponding inverse transform of the applied traction vector (Equation (5)). This reduces the evaluation of the expansion coefficients to solving a system of equations. In order to incorporate the probe model into the $\boldsymbol{T}$ matrix formulation we have to transform our displacement field from the plane vector waves centred at the contact area into spherical vector wave functions suitably oriented and centred at the defect. This involves a transformation, a translation and a rotation as discussed in Boström and Wirdelius [1].

The characterization of the probe acting as a transmitter is encapsulated in the expansion coefficients for the incident field (a_n) and to evaluate its behaviour as a receiver we use a electromechanical reciprocity argument by Auld [16] and define two elastodynamic states:

$$\begin{cases} \boldsymbol{u}_1, \boldsymbol{t}_1 : \text{a acting as transmitter with defect present} \\ \boldsymbol{u}_2, \boldsymbol{t}_2 : \text{b acting as transmitter without defect present} \end{cases} \tag{8}$$

(each probe acting with incident power P). Then the change in the electrical response of probe b, due to the presence of a defect (enclosed by a control surface S), is found as

$$\delta\Gamma = -\frac{i\omega}{4P}\int_S \left[\boldsymbol{u}_2 \cdot \boldsymbol{t}_1 - \boldsymbol{u}_1 \cdot \boldsymbol{t}_2\right] \mathrm{d}S \tag{9}$$

Expanding the two states in spherical vector wave functions and using the Betti identities we end up with the following expression for the electrical signal response

$$\delta\Gamma \sim \sum_{nn'} a_n^b T_{nn'} a_{n'}^a \text{ with } \begin{cases} \text{characterization of transmitting probe by } a_{n'}^a \\ \text{characterization of defect by } T_{nn'} \\ \text{characterization of receiving probe by } a_n^b \end{cases} \tag{10}$$

3. Optimization Technique

In the previous section, the theory for the direct problem (the ultrasonic NDT model) has been presented while we in this section introduce the optimization techniques that are used to numerically solve the corresponding inverse problem (see [11] [14] for further details).

The optimization problem is to fit a set of data (y_i, d_i), $i = 1, \cdots, m$, with a model $m(\boldsymbol{x}, y_i)$. Let us define the residual function as

$$\begin{aligned} &\boldsymbol{R} : \mathbb{R}^n \to \mathbb{R}^m, m > n \\ &r_i(\boldsymbol{x}) = m(\boldsymbol{x}, y_i) - d_i \end{aligned} \tag{11}$$

where $\boldsymbol{x} \in \mathbb{R}^n$ is a point in parameter space, y_i is the coordinate, d_i is the data of the i^{th} "sampling" and $r_i(\boldsymbol{x})$ denotes the i^{th} component function of $\boldsymbol{R}(\boldsymbol{x})$. Then the optimization can be stated as a minimization problem (referred to as a nonlinear least-squares problem)

$$\text{minimize}_{\mathbf{x}\in\mathbb{R}^n} f(\boldsymbol{x}) = \frac{1}{2}\boldsymbol{R}(\boldsymbol{x})^{\mathrm{T}} \boldsymbol{R}(\boldsymbol{x}) = \frac{1}{2}\sum_{i=1}^m r_i(\boldsymbol{x})^2 \tag{12}$$

A quadratic model of $f(\boldsymbol{x})$ around the current point $\boldsymbol{x}_c$ is achieved by a two term Taylor expansion

$$\begin{aligned} g_c(\boldsymbol{x}) &= f(\boldsymbol{x}_c) + \nabla f(\boldsymbol{x}_c)^{\mathrm{T}}(\boldsymbol{x} - \boldsymbol{x}_c) + \frac{1}{2}(\boldsymbol{x} - \boldsymbol{x}_c)^{\mathrm{T}} \nabla^2 f(\boldsymbol{x}_c)^{\mathrm{T}} (\boldsymbol{x} - \boldsymbol{x}_c) \\ &= \frac{1}{2} R(\boldsymbol{x}_c)^{\mathrm{T}} R(\boldsymbol{x}_c) + R(\boldsymbol{x}_c)^{\mathrm{T}} J(\boldsymbol{x}_c)(\boldsymbol{x} - \boldsymbol{x}_c) + \frac{1}{2}(\boldsymbol{x} - \boldsymbol{x}_c)^{\mathrm{T}} \left\{ J(\boldsymbol{x}_c)^{\mathrm{T}} J(\boldsymbol{x}_c) + S(\boldsymbol{x}_c) \right\} (\boldsymbol{x} - \boldsymbol{x}_c). \end{aligned} \tag{13}$$

with the Jacobian matrix $\boldsymbol{J} \in \mathbb{R}^n \times \mathbb{R}^m$, with components $\boldsymbol{J}(\boldsymbol{x})_{ij} = \partial r_i(\boldsymbol{x}) / \partial x_j$ and the second derivate matrix of $\boldsymbol{R}(\boldsymbol{x})$ as

$$\boldsymbol{S}(\boldsymbol{x}) = \sum_{i=1}^m r_i(\boldsymbol{x}) \nabla^2 r_i(\boldsymbol{x}) \tag{14}$$

The next iterate $\boldsymbol{x}_+$ is then found as the minimizer of Equation (14) by applying Newton's method (see Dennis and Schnabel [14]), *i.e.*

$$\boldsymbol{x}_+ = \boldsymbol{x}_c - \left[\boldsymbol{J}(\boldsymbol{x}_c)^{\mathrm{T}} \boldsymbol{J}(\boldsymbol{x}_c) + \boldsymbol{S}(\boldsymbol{x}_c) \right]^{-1} \boldsymbol{J}(\boldsymbol{x}_c)^{\mathrm{T}} \boldsymbol{R}(\boldsymbol{x}_c) \tag{15}$$

This is a fast local method since it is locally (*i.e.* near the true minimizer $\boldsymbol{x}_{tr}$) q-quadratically convergent but has the drawback of the necessity of calculating $\boldsymbol{S}(\boldsymbol{x})$ which is usually either unavailable or inconvenient to obtain.

Instead of using the quadratic model $g_c(\boldsymbol{x})$, we introduce the affine model of $\boldsymbol{R}(\boldsymbol{x})$ around the current point $\boldsymbol{x}_c$

$$\begin{aligned} &\boldsymbol{G}_c : \mathbb{R}^n \to \mathbb{R}^m, m > n \\ &\boldsymbol{G}_c(\boldsymbol{x}) = \boldsymbol{R}(\boldsymbol{x}_c) + \boldsymbol{J}(\boldsymbol{x}_c)(\boldsymbol{x} - \boldsymbol{x}_c) \end{aligned} \tag{16}$$

This is an over determined system of linear equations and therefore we cannot expect to find an $\boldsymbol{x}_+$ that satisfies $G_c(\boldsymbol{x}_+)=0$. A logical consequence is then to choose the next iterate $\boldsymbol{x}_+$ as the solution to the linear least-squares problem

$$\text{minimize}_{\boldsymbol{x}\in\mathbb{R}^n}\ \frac{1}{2}\boldsymbol{G}_c(\boldsymbol{x})_2^2=\hat{g}_c(\boldsymbol{x}) \tag{17}$$

If $\boldsymbol{J}(\boldsymbol{x}_c)$ has full rank the solution can be written as

$$\boldsymbol{x}_+=\boldsymbol{x}_c-\left[\boldsymbol{J}(\boldsymbol{x}_c)^{\mathrm{T}}\boldsymbol{J}(\boldsymbol{x}_c)\right]^{-1}\boldsymbol{J}(\boldsymbol{x}_c)^{\mathrm{T}}\boldsymbol{R}(\boldsymbol{x}_c) \tag{18}$$

The only difference between the quadratic models $g_c(\boldsymbol{x})$ (Newton method) and $\hat{g}_c(\boldsymbol{x})$ (Gauss-Newton method) is the lack of second order information of $\nabla^2 f(\boldsymbol{x}_c)$ in the latter which makes it q-quadratically convergent only if $\boldsymbol{S}(\boldsymbol{x}_{tr})=\boldsymbol{0}$ (*i.e.* $\boldsymbol{R}(\boldsymbol{x})$ linear or $\boldsymbol{R}(\boldsymbol{x}_{\mathrm{tr}})=\boldsymbol{0}$: a zero-residual problem). If it is a small-residual problem then the convergence will be q-linear. However, for large-residual problems it may not be locally convergent at all.

In order to enhance the Gauss-Newton method we introduce the singular value decomposition (SVD) of the Jacobian matrix $\left(\boldsymbol{J}\in\mathbb{R}^n\times\mathbb{R}^m\right)$

$$\boldsymbol{J}=\boldsymbol{U}\boldsymbol{D}\boldsymbol{V}^{\mathrm{T}},\ \boldsymbol{D}=\begin{cases}d_{ii}=\sigma_i\geq 0,\ \ i=1,\cdots,\min(m,n)\\ d_{ij}=0,\ \ i\neq j\end{cases}\quad\left(\boldsymbol{D}\in\mathbb{R}^m\times\mathbb{R}^n\right) \tag{19}$$

where $\boldsymbol{U}\in\mathbb{R}^m\times\mathbb{R}^m$ and $\boldsymbol{V}\in\mathbb{R}^n\times\mathbb{R}^n$ are orthogonal matrices. The diagonal elements of $\boldsymbol{D}$ (*i.e.* the singular values of $\boldsymbol{J}$) are the nonnegative square roots of the eigenvalues of $\boldsymbol{J}^{\mathrm{T}}\boldsymbol{J}$ if $m\geq n$ (or $\boldsymbol{J}\boldsymbol{J}^{\mathrm{T}}$ if $n\geq m$) and the columns of $\boldsymbol{U}$ and $\boldsymbol{V}$ are eigenvectors of $\boldsymbol{J}^{\mathrm{T}}\boldsymbol{J}$ and correspondingly $\boldsymbol{J}\boldsymbol{J}^{\mathrm{T}}$ if $n\geq m$.

Furthermore we define a pseudoinverse of $\boldsymbol{J}$, the Moore-Penrose inverse, as

$$\boldsymbol{J}^{\dagger}=\boldsymbol{V}\boldsymbol{D}^{\dagger}\boldsymbol{U}^{\mathrm{T}},\ \ \boldsymbol{D}^{\dagger}=\begin{cases}d_{ii}^{\dagger}=\begin{cases}\dfrac{1}{\sigma_i},\sigma_i>0\\ 0,\sigma_i=0\end{cases}\\ d_{ij}^{\dagger}=0,i\neq j\end{cases}\quad\left(\boldsymbol{D}^{\dagger}\in\mathbb{R}^n\times\mathbb{R}^m\right) \tag{20}$$

Then the minimizer of Equation (17) is found by (*i.e.* SVD-Newton iterate)

$$\boldsymbol{x}_+=\boldsymbol{x}_c-\boldsymbol{J}(\boldsymbol{x}_c)^{\dagger}\boldsymbol{R}(\boldsymbol{x}_c) \tag{21}$$

In order to suppress linear dependence of the column vectors, which will occur in the case of problems that are insensitive to variations of, or a linear combination of, parameters, we introduce the regularized Moore-Penrose inverse as

$$\boldsymbol{J}_{\lambda}^{\dagger}=\boldsymbol{V}\boldsymbol{D}_{\lambda}^{\dagger}\boldsymbol{U}^{\mathrm{T}},\ \boldsymbol{D}_{\lambda}^{\dagger}=\begin{cases}d_{ii}^{\dagger}=\begin{cases}\dfrac{1}{\sigma_i},\sigma_i\geq\lambda^2\\ 0,\sigma_i<\lambda^2\end{cases}\\ d_{ij}^{\dagger}=0,i\neq j\end{cases}\quad\left(\boldsymbol{D}_{\lambda}^{\dagger}\in\mathbb{R}^n\times\mathbb{R}^m\right) \tag{22}$$

where the regularizing parameter, λ, has the effect of masking off directions in parameter space in which the problem is ill-conditioned.

The previous discussed locally convergent variation of the Newton method has to be supplemented by a global strategy in order to also enable global convergence to the problem. The direction of the Newton step is always a descent direction (if $\boldsymbol{S}(\boldsymbol{x}_c)$ is limited this includes the Gauss-Newton) but the step may well be too large and therefore not globally convergent.

Given this descent direction, $\boldsymbol{p}_k$, and $\alpha\in(0,1)$ we try to find $\boldsymbol{x}_{k+1}=\boldsymbol{x}_k+\zeta_k\boldsymbol{p}_k$, with $\zeta_k\in(0,1]$, until we get

$$f\left(\boldsymbol{x}_{k+1}\right) \le f\left(\boldsymbol{x}_k\right) + \alpha\zeta_k \nabla f\left(\boldsymbol{x}_c\right)^{\mathrm{T}} \boldsymbol{p}_k \tag{23}$$

if also

$$\nabla f\left(\boldsymbol{x}_{k+1}\right)^{\mathrm{T}} \boldsymbol{p}_k = \nabla f\left(\boldsymbol{x}_k + \zeta_k \boldsymbol{p}_k\right)^{\mathrm{T}} \boldsymbol{p}_k \ge \beta \nabla f\left(\boldsymbol{x}_k\right)^{\mathrm{T}} \boldsymbol{p}_k, \quad \beta \in (\alpha, 1] \tag{24}$$

is satisfied. Then there can be proven that given any direction $\boldsymbol{p}_k$ such that

$$\nabla f\left(\boldsymbol{x}_k\right)^{\mathrm{T}} \boldsymbol{p}_k < 0 \tag{25}$$

there exists $\zeta_k > 0$ such that any method that generates a sequence $\{\boldsymbol{x}_k\}$ obeying these three conditions $(23 \to 25)$, is at each iteration globally convergent. Let us define $\hat{f}(\zeta) = f\left(\boldsymbol{x}_k + \zeta \boldsymbol{p}_k\right)$ and, if we need to backtrack, use the most current information about $\hat{f}$ to model it, and then take the value of ζ that minimizes this model as our next value of ζ_k.

Initially we have; $\hat{f}(0) = f\left(\boldsymbol{x}_k\right)$, $\hat{f}'(0) = \nabla f\left(\boldsymbol{x}_k\right)^{\mathrm{T}} \boldsymbol{p}_k$ and $\hat{f}(1) = f\left(\boldsymbol{x}_k + \boldsymbol{p}_k\right)$, which result in the following quadratic model of $\hat{f}(\zeta)$

$$\hat{g}_q(\zeta) = \left[\hat{f}(1) - \hat{f}(0) - \hat{f}'(0)\right]\zeta^2 + \hat{f}'(0)\zeta + \hat{f}(0) \tag{26}$$

then

$$\hat{\zeta} = -\hat{f}'(0) \Big/ 2\left[\hat{f}(1) - \hat{f}(0) - \hat{f}'(0)\right] \Leftrightarrow \hat{g}_q'\left(\hat{\zeta}\right) = 0 \text{ and } \hat{g}_q''\left(\hat{\zeta}\right) > 0 \tag{27}$$

and $\hat{\zeta} \in \left(0, \frac{1}{2}\right]$ is our new choice of ζ_k.

In order to ensure proximity we in the numerical calculations start up with a SVD-Newton step (using Equation (22)) and if this full step does not give an acceptable decrease in the residual we use the above described backtracking line search along this direction.

4. Numerical Results

In this section we present numerical examples of the optimization algorithm developed by Björkberg and Kristensson [11] and here implemented into the elastodynamic problem of defect detection. Our choice of NDE-situation has been the pulse-echo measurement on a elastic half-space with the material assumed to be steel with compression and shear wave speeds 5940 m/s and 3230 m/s (Poison's ratio $\nu = 0.29$). A major limitation of the numerical optimization is of course the necessity to postulate the defect geometry (*i.e.* a priori information on the used $\boldsymbol{T}$ matrix).

We have restricted our optimization to three combinations of defect geometry and scanning probe: spherical cavity (diameter 10 mm) detected with an unangled circular (diameter 10 mm) *P* probe, open horizontal penny-shaped crack (diameter 10 mm) detected with an unangled circular (diameter 10 mm) P probe and the same crack lying perpendicular to the surface scanned by a 60˚ angled quadratic (side 10 mm) SV probe. All defects are situated at a depth of 60 mm and given a radius of 5 mm and corresponding single frequency C-scans are found in **Figures 3(a)-(c)**) with individual normalization.

These three ultrasonic inspection situations all contributes with four parameters which we then seek in our optimizations. These four parameters are the x and y coordinates, the depth a (of the defect centre) and the defect diameter d. The deviations from the true values are given in percentages and for a and d these percentages are relative the values $a = 60$ mm and $d = 100$ mm. For the x and y coordinates, however, the percentages are somewhat arbitrarily given relative (−10, −15), (−10, −15) and (70, −10) mm for cases 3A-C, respectively (these are the distances from the defect to the lower left corner of the C-scans in **Figures 3(a)-(c)**). To identify what information our residual should be based upon we have done parametric studies and these are presented in **Figures 4-6**. These show that phase information in our case is not useful as a residual which is most obvious when we vary depth or size of the scatterer. The residual is also shown to be more sensitive to the number of frequencies than to the actual number of geometrical samplings points. This effect is revealed in **Figure 5** when compared with **Figure 4** and is most obvious for the size parameter.

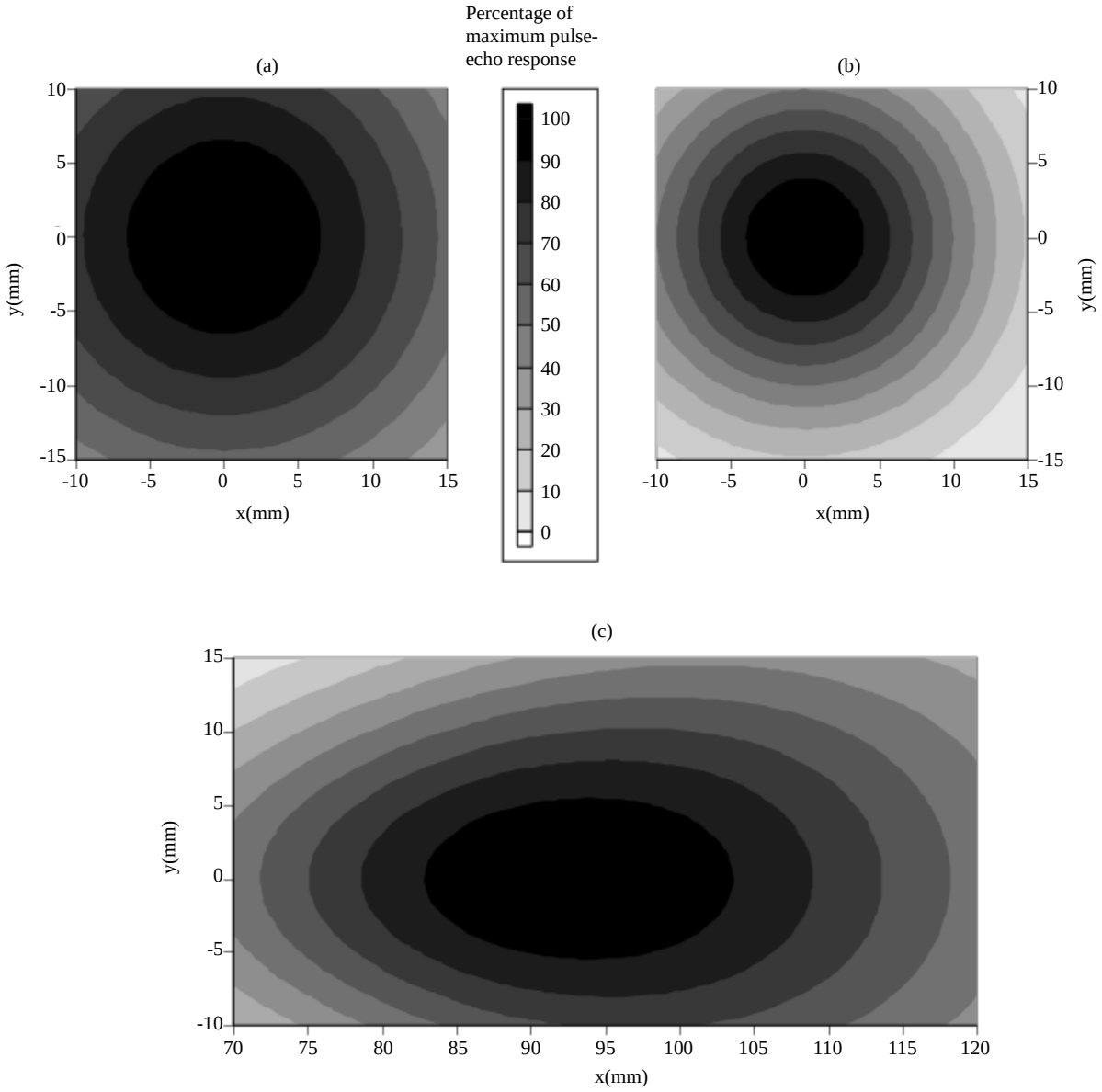

Figure 3. Pulse-echo amplitude as a function of probe position (all probes operating at 1 MHz single frequency): A/ Unangled circular (diameter 10 mm) *P* probe with a spherical cavity defect (diameter 10 mm) located at the depth 60 mm. B/ Unangled circular (diameter 10 mm) *P* probe with a penny-shaped crack (diameter 10 mm) located at the depth 60 mm and parallel to the surface. C/60˚ angled quadratic (side 10 mm) SV probe with a penny-shaped crack (diameter 10 mm) located at the depth 60 mm and perpendicular to the surface.

In the expression for the expansion coefficients, a_n^a and a_n^b, a double integral has to be evaluated. To avoid a quite computer time-consuming numerical integration (*i.e.* Gauss-Legendre qudrature), we have chosen to evaluate this with the two-dimensional stationary-phase method (the distance between defect and probe is used as the large parameter). In the far field this have been found to be accurate at least within the main lobe (see [1]) and in order to avoid what is referred to as an "inverse crime" (see Colton and Kress [17]), we have also optimized with a "stationary-phase solver" on a integral solution of the direct problem. It is also necessary to suppress the compression part when using an angled SV probe to get the optimization successful.

The time dependence is easy to obtain by an FFT algorithm, but even if the time window is easy to predict and thereby kept small this involves dealing with a waste number of points without any valid information since the response is a pulse in time. Therefore we have chosen to optimize in the frequency domain but with a similar

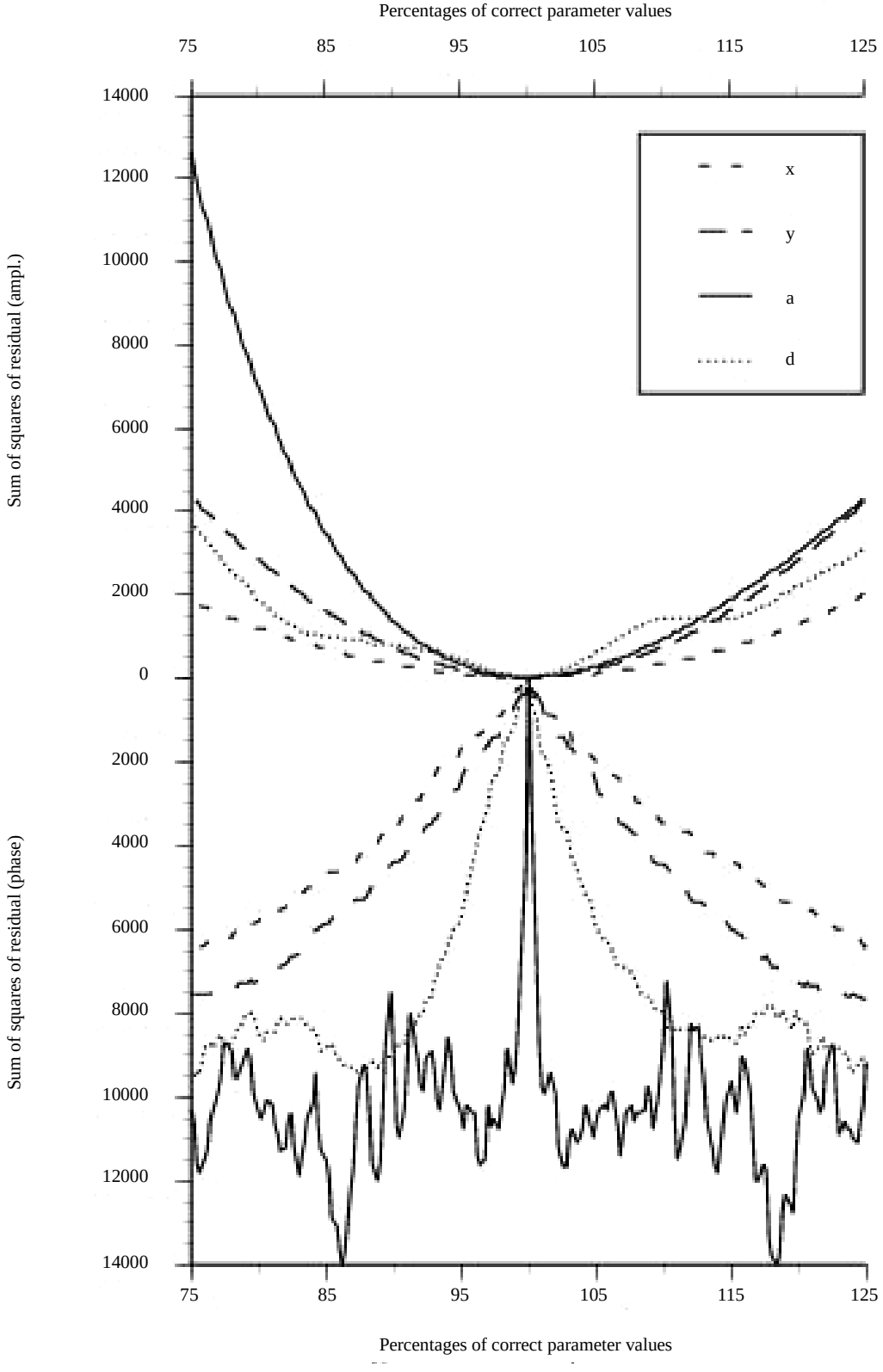

Figure 4. Amplitude residual and phase residual as a function of deviation from correct parameter value for NDE situation 3*A*. Parameters are: *x* and *y* coordinate, the depth *a* and the diameter *d* of the defect. Based on information from 12 freq. and 12 × 12 geometrical points ($m = 1728$).

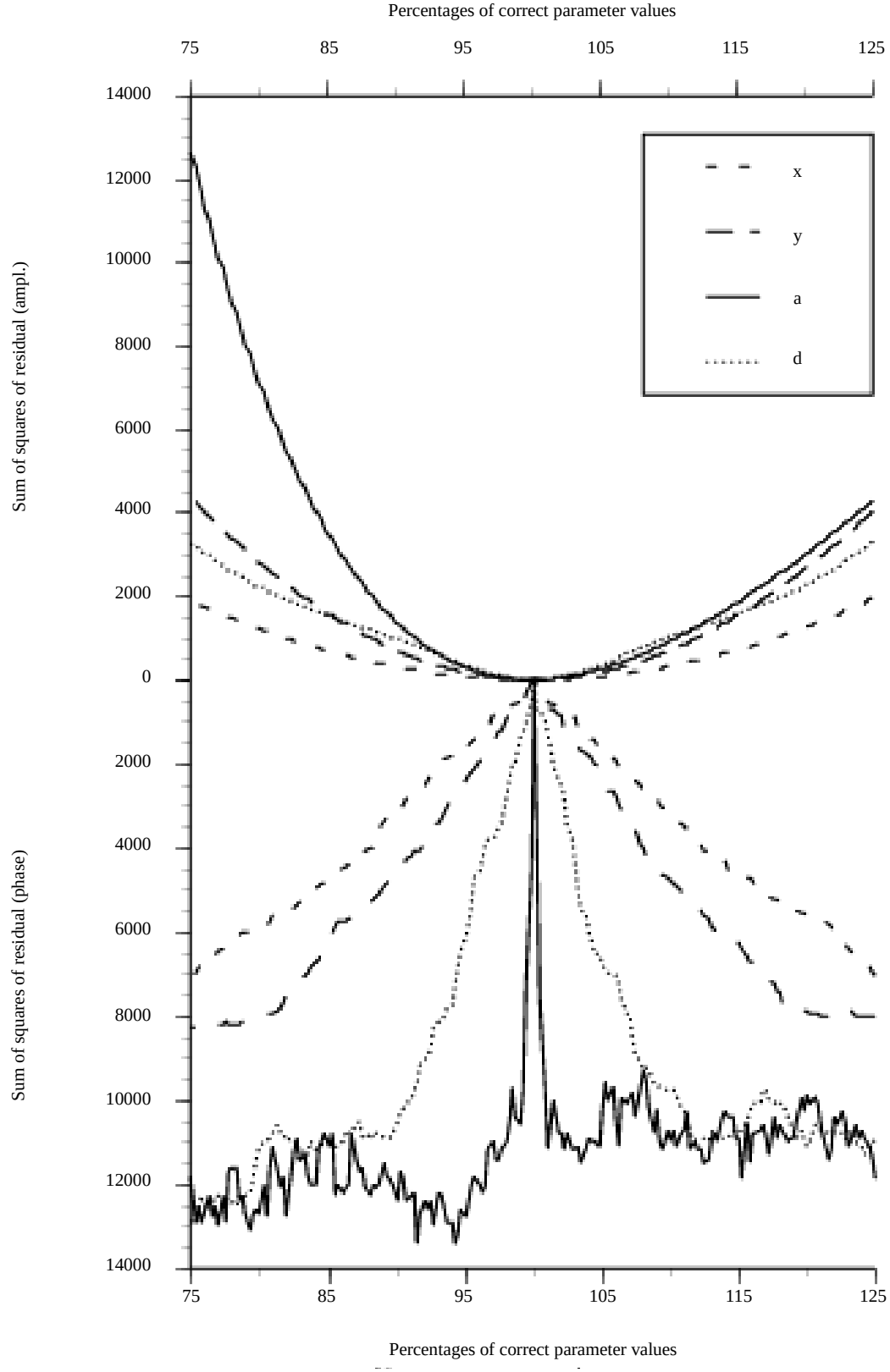

Figure 5. Same as in **Figure 4** but based on information from 50 freq. and 6 × 6 geometrical points (m = 1800).

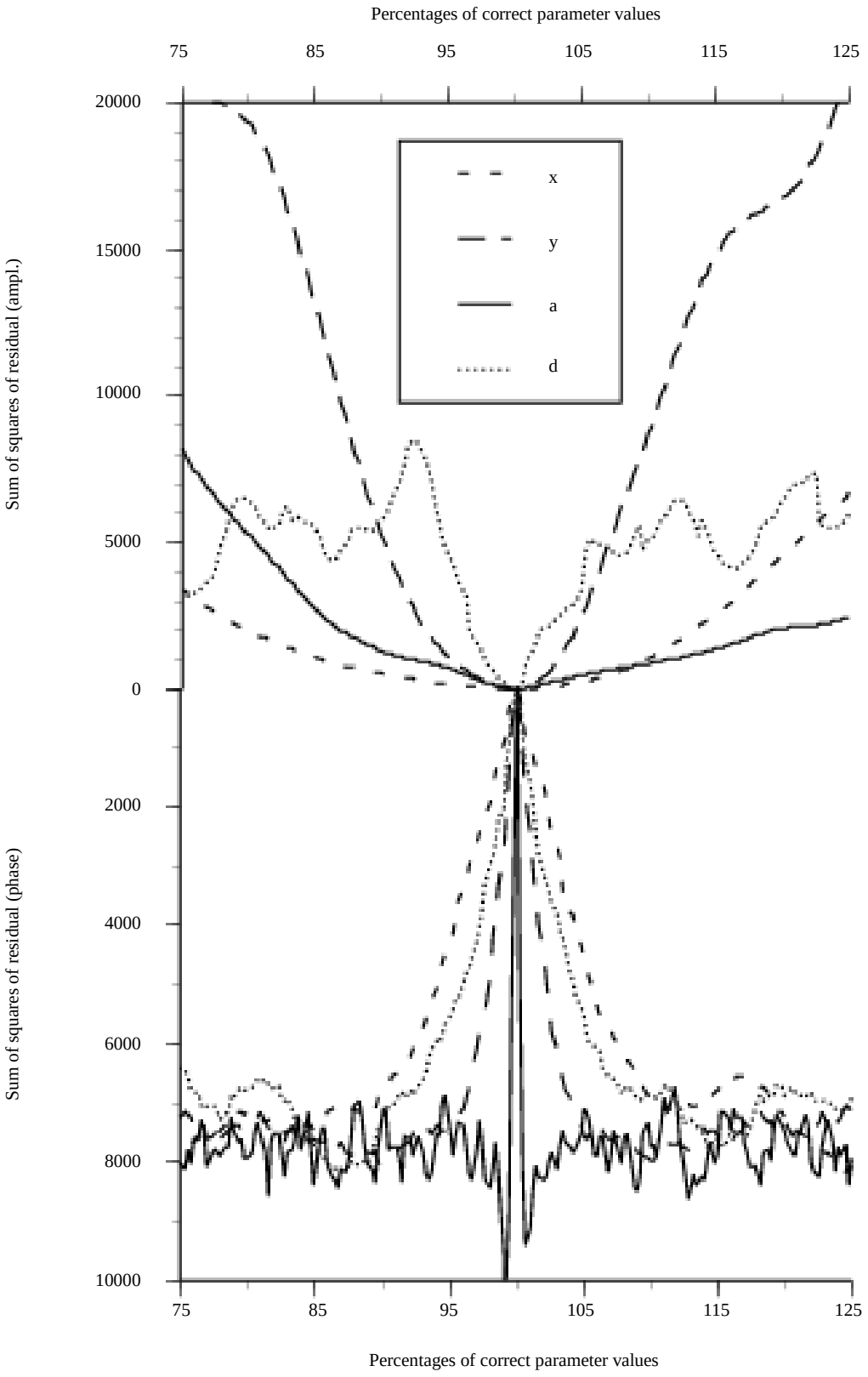

Figure 6. Same as in **Figure 4** and **Figure 5** but for NDE situation 3*B* based on information from 10 freq. and 11 × 11 geometrical points (m = 1210).

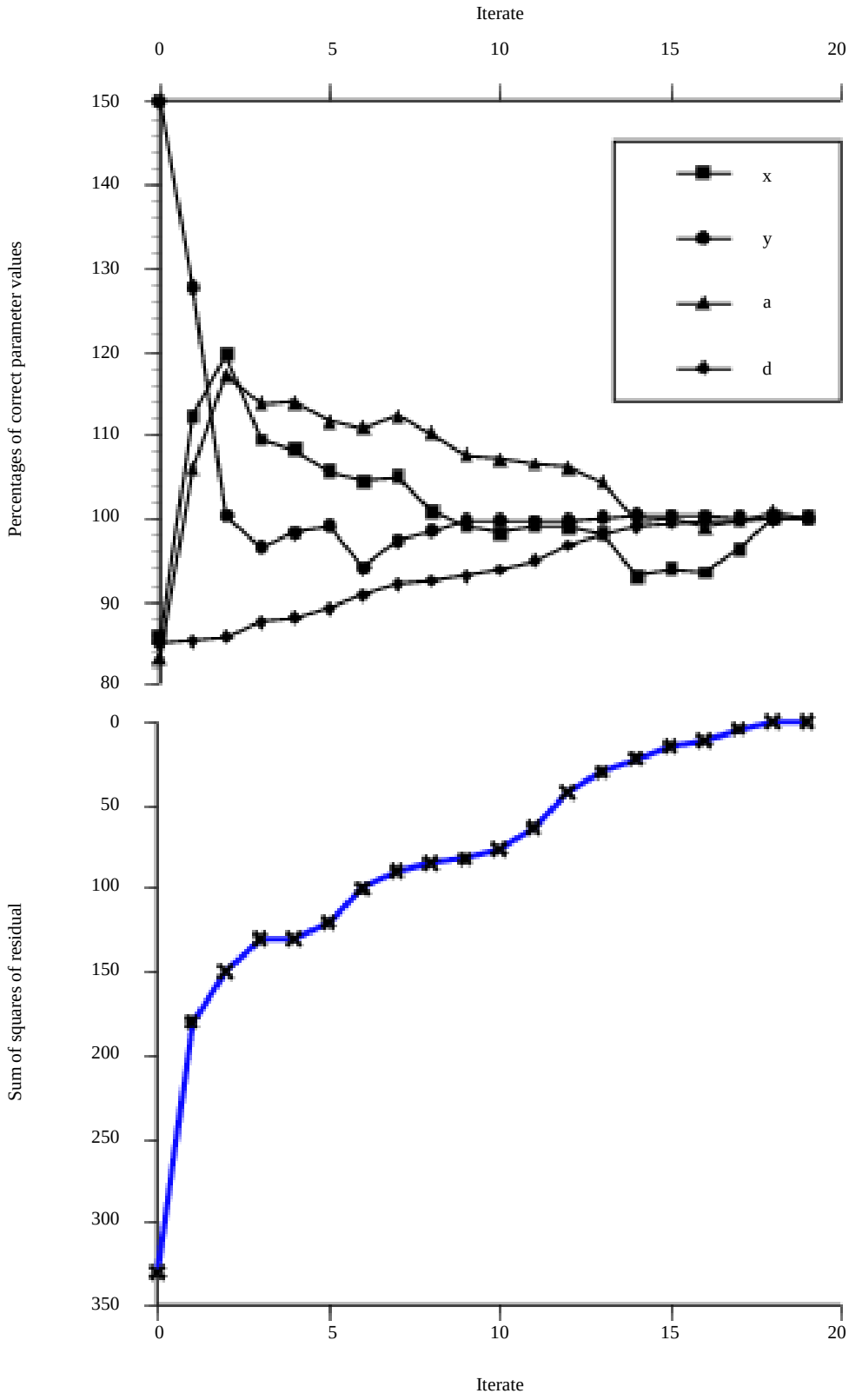

Figure 7. Optimization on situation 3*C* based on information from 50 freq. and 6 × 6 geometrical points (m = 1800).

weight function characterizing the probe as that proposed by Boström and Wirdelius [1]. In this model a symmetric sine square function is used as the frequency spectrum and our model of the signal response can therefore be written as

$$\omega(\mathbf{x}, y_i) = \sin^2\left(\omega(y_i)\right)\left|\delta\Gamma(\mathbf{x}, y_i)\right|, \quad i = 1, \cdots, m \tag{28}$$

with m as the product of geometrical sampling points and the number of frequencies.

No normalization has been incorporated into the ultrasonic NDT model and therefore the actual residual value is individual in each case. The maximum amplitude of signal response for the three cases shown in **Figure 3** varies as $\delta\Gamma^{3B}_{\max} / \delta\Gamma^{3A}_{\max} \approx 4.5$ and $\delta\Gamma^{3A}_{\max} / \delta\Gamma^{3C}_{\max} \approx 9$.

The parameter that is limiting the optimization is the size and this is also obvious in the parametric study of the penny-shaped crack parallel to the scanned surface. In fact, the number of frequencies had to be increased to 50 (10 frequencies are used in **Figure 6**) in order to get the optimization to converge. Even then the initial guess had to be within a deviation of 15 percentages in order to converge.

Figures 7-9 shows the result from the optimization of the situation of a 60˚ angled SV probe with a penny-shaped crack perpendicular to the surface. In **Figure 7** the initial guess of crack diameter is 85% of the

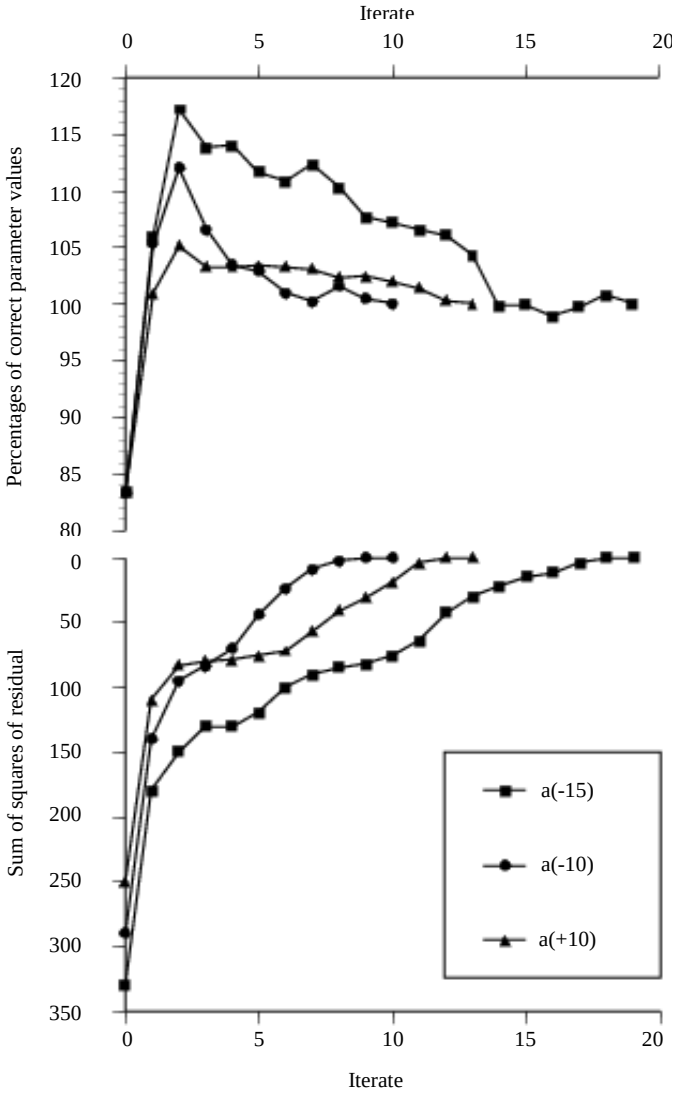

Figure 8. The depth variation when optimization is performed as in **Figure 7** and for three initial guess of defect diameter.

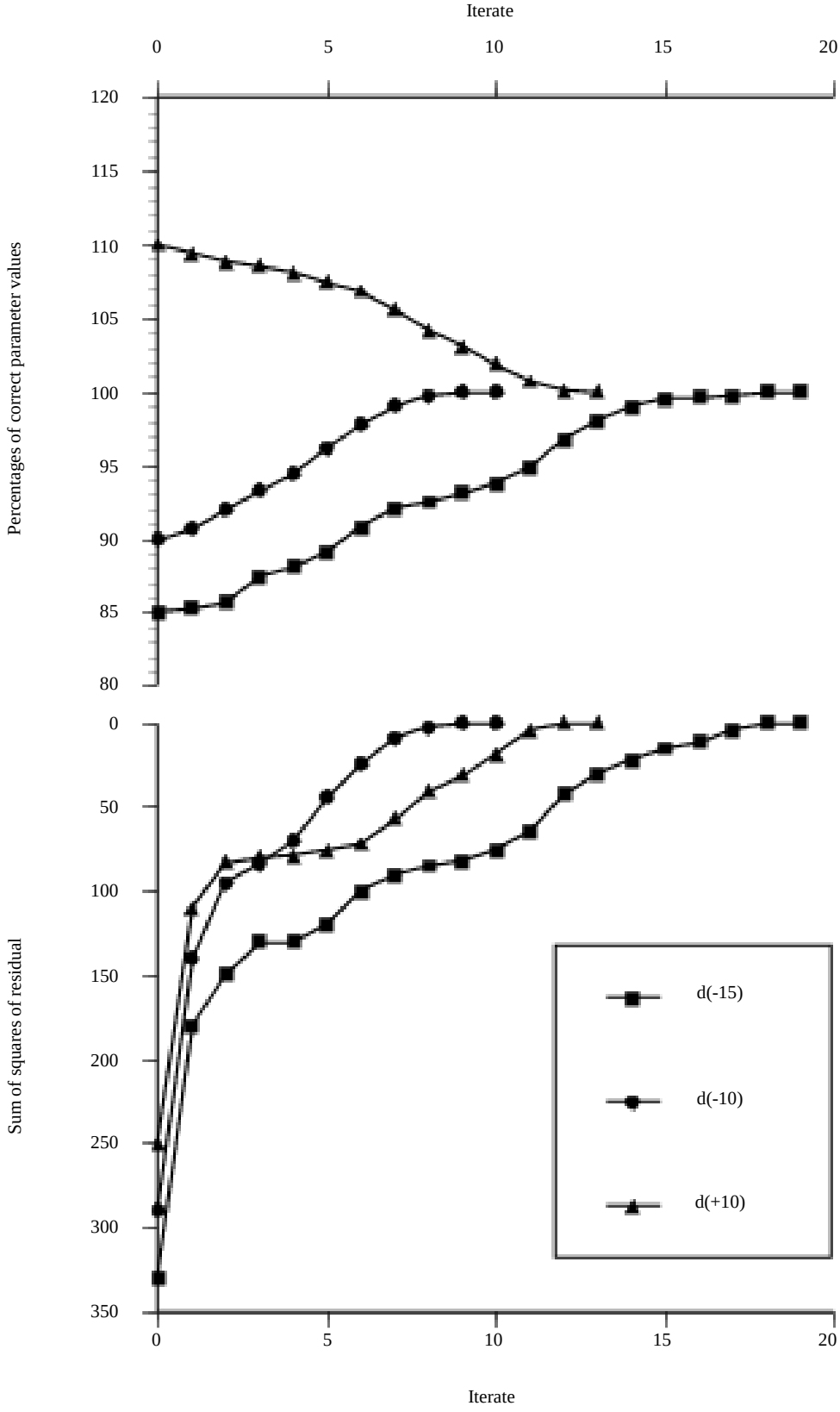

Figure 9. The diameter variation when optimization is performed as in **Figure 7** and **Figure 8**.

correct value and all the parameters convergence rate is presented in the figure while we have chosen to present the diameter and depth convergence rate as a function of initial guess of diameter in **Figure 8** and **Figure 9**, respectively. This is due to the fact that these two parameters are not independent of each other. The over-estimation of the depth at second iterate found in **Figure 8** is as seen strongly dependent on the initial guess of diameter and critical in terms of convergence. The two major stopping criteria of the optimization are the distance between two steps and sufficient decrease of the residual.

In **Figure 10**, we present the optimization on the same NDT situation using an asymptotic probe model on data achieved by the corresponding integral solution. This reduce the convergence from being *q*-quadratical to being *q*-linear and the number of iterates increases from 20 to 25 before the stopping criterion of step size ends the optimization. At the minimum all parameters are within 1% deviation from the values representing the "true" minimizer, except for the x parameter that ends at 96% of its corresponding value.

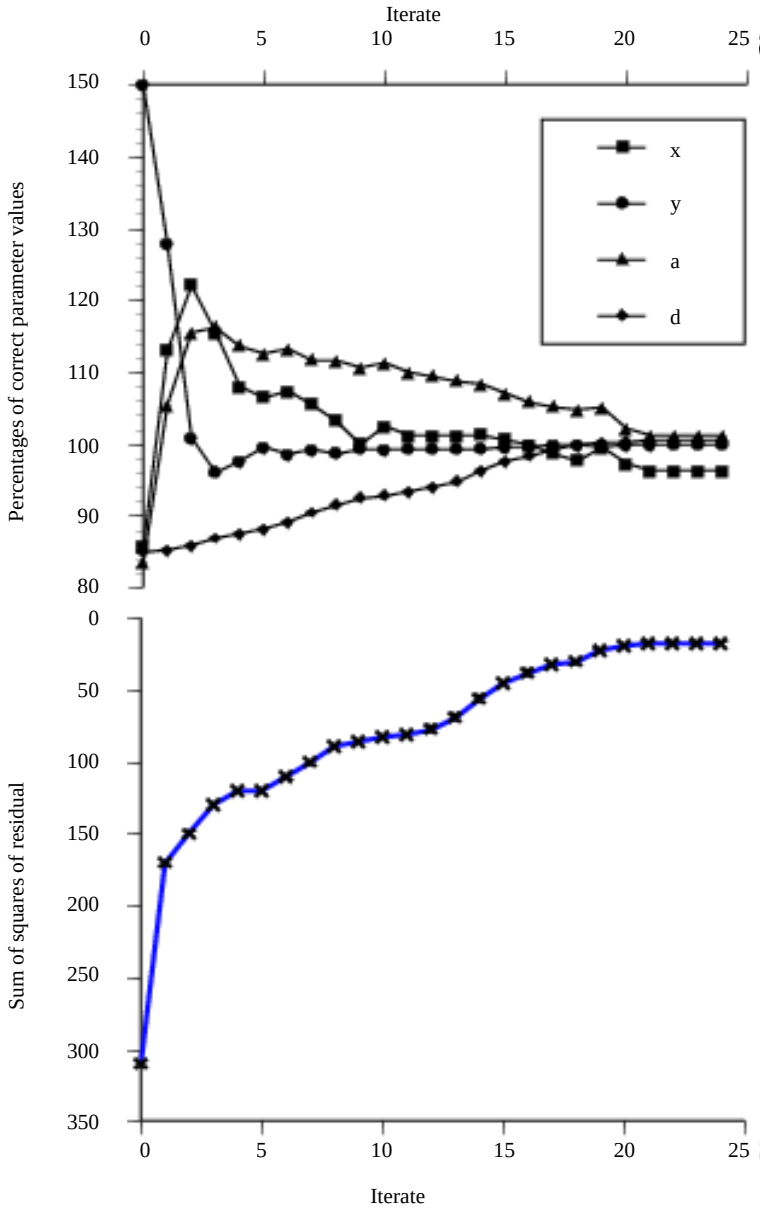

Figure 10. Optimization as in **Figure 7**, performed with asympt. probe model on data generated by corresponding integral solution (non-zero residual probl.).

Figure 11 present the result of the optimization on the situation of an unangled *P* probe with a penny-shaped crack parallel to the scanning surface. The problem with overestimation of the depth parameter at the second iteratation is also present for this situation. Even though this effect is more pronounced in this case, the true minimizer is already found at the 10:th iterate.

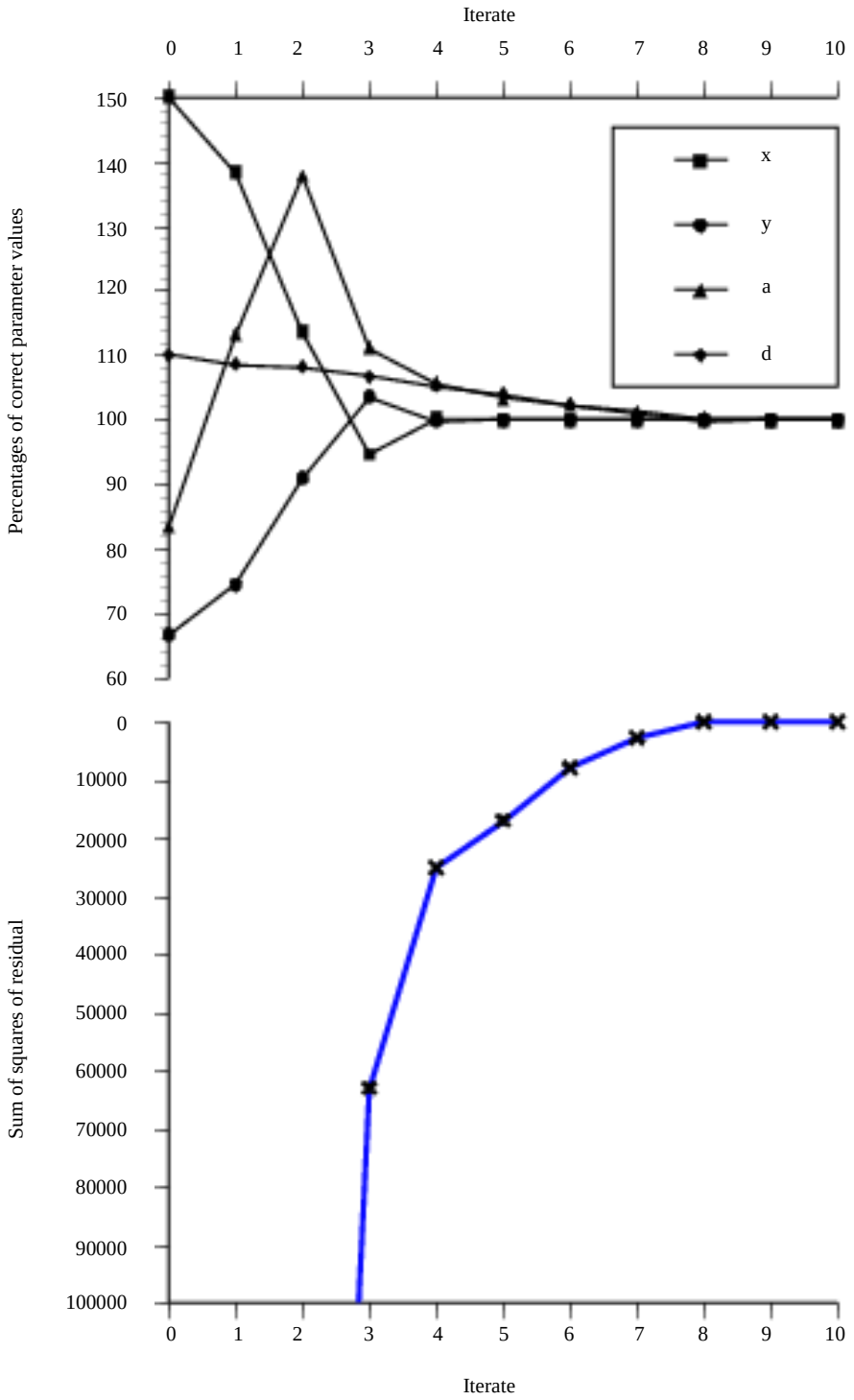

Figure 11. Optimization on situation 3*B* based on information from 50 freq. and 6 × 6 geometrical points ($m = 1800$).

In **Figures 12-15**, the type of defect is altered to a spherical cavity and scanned by an unangled *P* probe. For this situation the dependence between depth and diameter are even more obvious since the maximum signal response is dependent on the distance represented by the difference between these two. The asymptotic probe model is used for data in **Figure 12** while the numerical integrated solution is data in **Figures 13-15**. The non-zero residual problem in **Figures 13-15** reduces the rate of convergence in terms of iteration as expected but the optimization actually becomes more insensitive to deviations from the "true" value in the initial guess of the size. At the minimum a cavity two percentages larger and oriented two percentages less in depth than that used to generate the data is found.

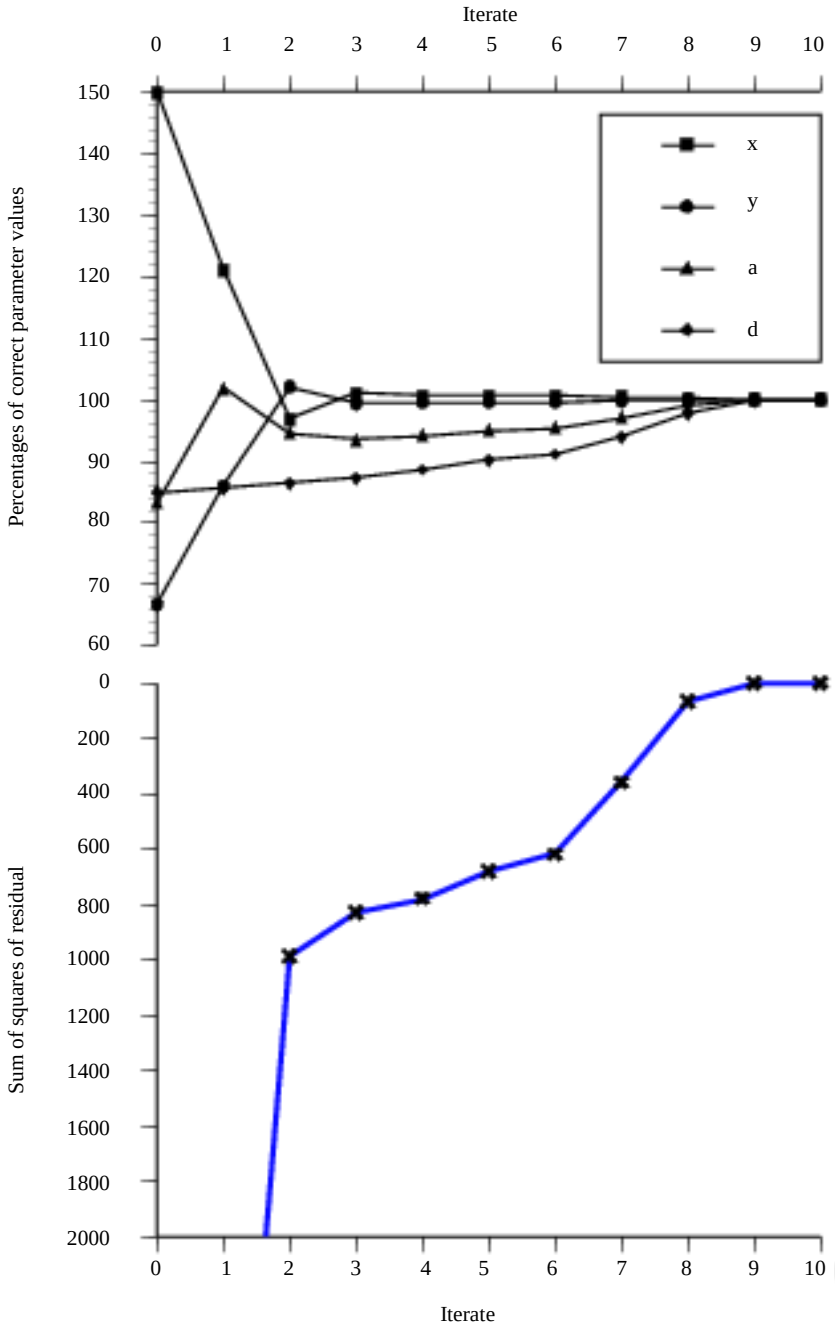

Figure 12. Optimization on situation 3*A* based on information from 50 freq. and 6 × 6 geometrical points (m = 1800).

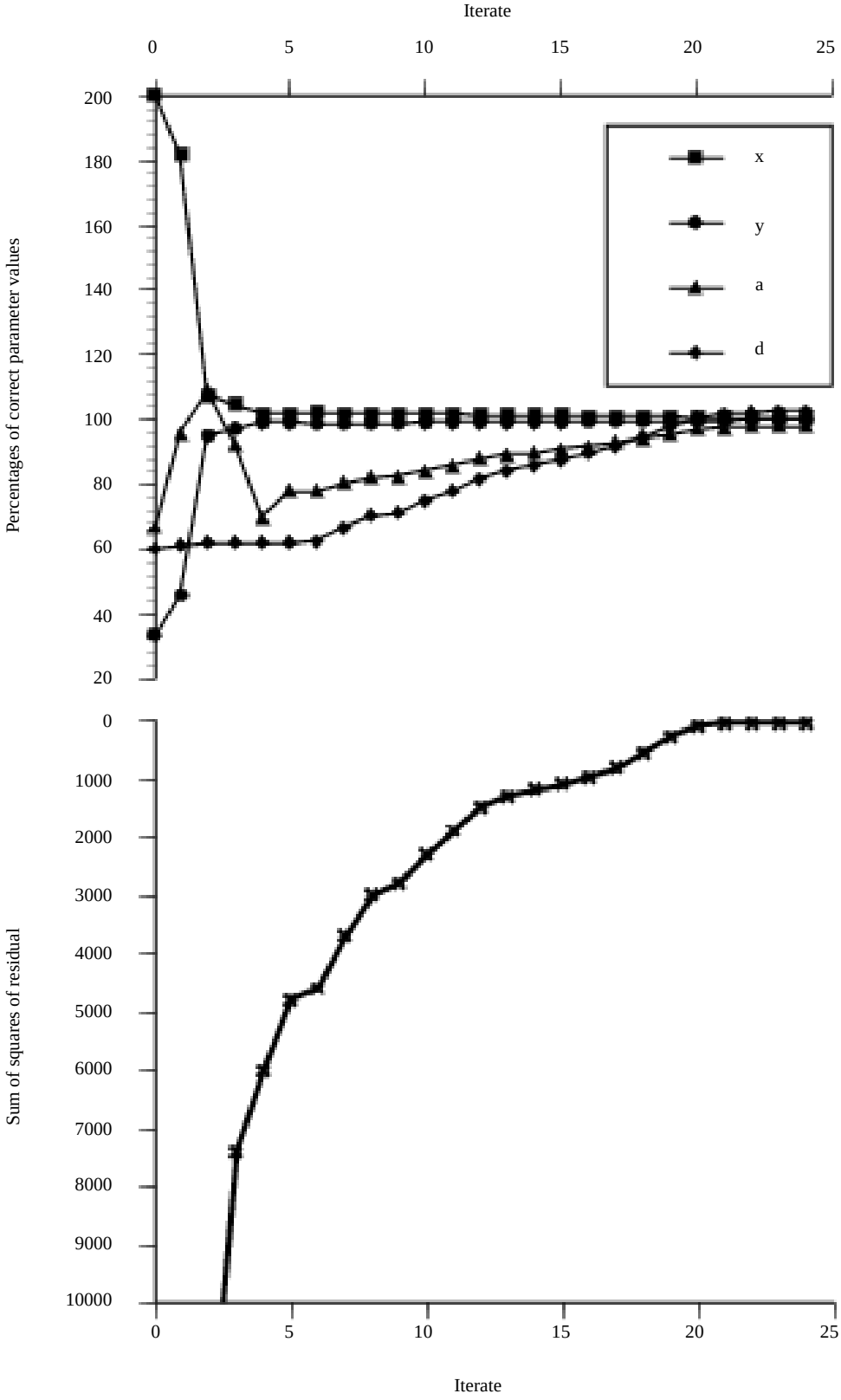

Figure 13. Optimization as in **Figure 12**, performed with asympt. probe model generated by corresponding integral solution (non-zero residual probl.).

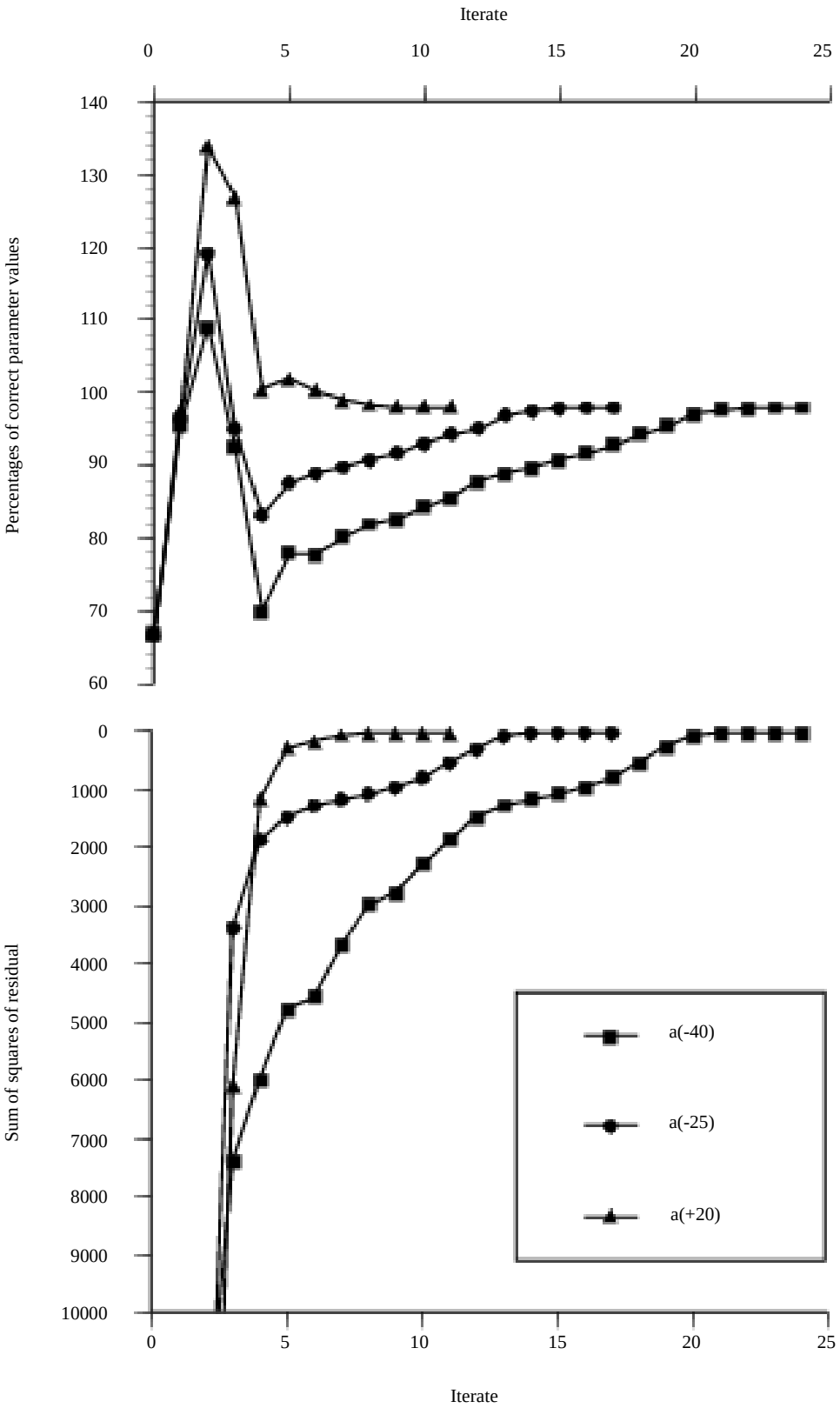

Figure 14. The depth variation when optimization is performed as in **Figure 13** and for three initial guess of defect diameter.

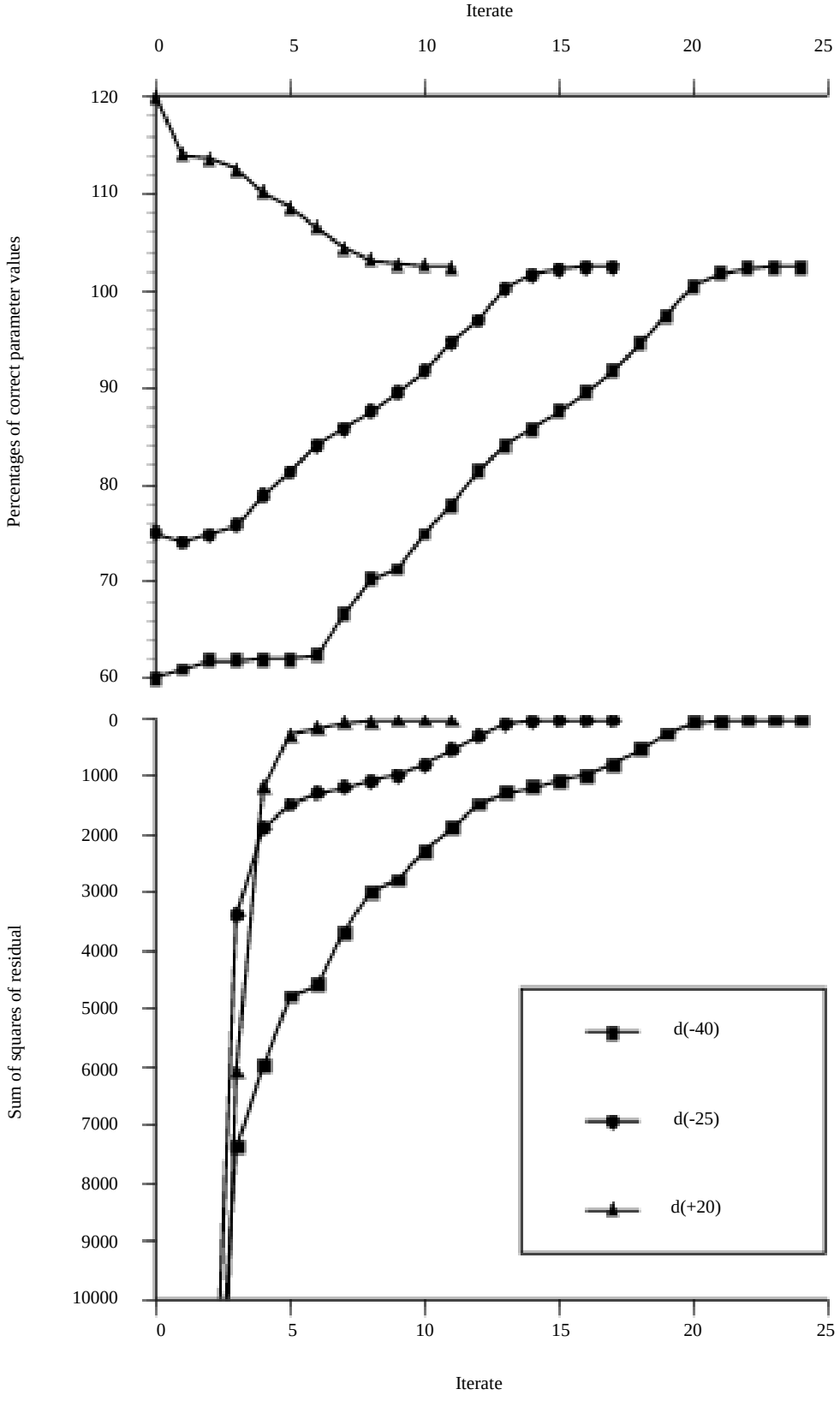

Figure 15. The diameter variation when optimization is performed as in **Figure 13** and **Figure 14**.

5. Concluding Remarks

In the preceding sections, we have studied a numerical inverse solution to the non-destructive testing situation. The method we have used to achieve this has been the application of an optimization technique on a model of the ultrasonic inspection situation. If the inverse algorithm, described in previous sections, is to be used together with experimental NDT data a more general $\boldsymbol{T}$ matrix has to be implemented. Such as the $\boldsymbol{T}$ matrix for an elliptic or rectangular crack, oriented by three Euler angles, increases the number of parameters to eight which call for improvement of the convergence. One conclusion that can be made from the numerical section is that there is a distinct difference between global parameters compared with local (*i.e.* 3*A*/3*B*: *a* and *d*, 3C: *x*, *a* and *d*), in terms of convergence.

References

[1] Boström, A. and Wirdelius, H. (1995) *The Journal of the Acoustical Society of America*, **97**, 2836-2848. http://dx.doi.org/10.1121/1.411850

[2] Wirdelius, H. (2007) Experimental Validation of the UTDefect Simulation Software. 6*th International Conference on NDE in Relation to Structural Integrity for Nuclear and Pressurized Components*, Budapest, 8-10 October 2007, 9 p.

[3] Persson, G. and Wirdelius, H. (2010) *AIP Conference Proceedings*, **1211**, 2125-2132. http://dx.doi.org/10.1063/1.3362392

[4] Bates, R.H.T., Smith, V.A. and Murch, R.D. (1991) *Physics Reports*, **201**, 185-277. http://dx.doi.org/10.1016/0370-1573(91)90026-I

[5] Guillaume, H., Lhémery, A., Calmon, P. and Lasserre, F. (2005) *Ultrasonics*, **43**, 619-628. http://dx.doi.org/10.1016/j.ultras.2005.03.006

[6] Mayer, K., Marklein, R., Langenberg, K.J. and Kreutter, T. (1990) *Ultrasonics*, **28**, 241-255. http://dx.doi.org/10.1016/0041-624X(90)90091-2

[7] Marklein, R., Langenberg, K.J., Mayer, K., Miao, J., Shlivinski, A., Zimmer, A., Müller, W., Schmitz, V., Kohl, C. and Mletzko, U. (2005) *Advances in Radio Science*, **3**, 167-174. http://dx.doi.org/10.5194/ars-3-167-2005

[8] Degtyar, A.D. and Rokhlin, S.I. (1997) *The Journal of the Acoustical Society of America*, **102**, 3458-3466. http://dx.doi.org/10.1121/1.419588

[9] Castaings, M., Hosten, B. and Kundu, T. (2000) *NDT & E International*, **33**, 377-392. http://dx.doi.org/10.1016/S0963-8695(00)00004-9

[10] Hosten, B. and Castaings, M. (2008) *Composites Part A*: *Applied Science and Manufacturing*, **39**, 1054-1058.

[11] Björkberg, J. and Kristensson, G. (1997) *Progress in Electromagnetics Research*, **15**, 141-164. http://dx.doi.org/10.2528/PIER95081800

[12] Wirdelius, H. (1992) *Journal of Nondestructive Evaluation*, **11**, 29-39. http://dx.doi.org/10.1007/BF00566015

[13] Boström, A. and Eriksson, A.S. (1993) *Proceedings of the Royal Society of London A*, **443**, 183-201. http://dx.doi.org/10.1098/rspa.1993.0139

[14] Dennis, J.E. and Schnabel, R.B. (1983) Numerical Methods for Unconstrained Optimization and Nonlinear Equations. Prentice-Hall, Englewoods Cliffs.

[15] Boström, A., Kristensson, G. and Ström, S. (1991) Transformation Properties of Plane, Spherical and Cylindrical Scalar and Vector Wave Functions. In: Varadan, V.K., Varadan, V.V. and Lakhtakia, A., Eds., Vol. 1, *Field Representations and Introduction to Scattering*, North Holland, Amsterdam, 165-210.

[16] Auld, B.A. (1979) *Wave Motion*, **1**, 3-10. http://dx.doi.org/10.1016/0165-2125(79)90020-9

[17] Colton, D. and Kress, R. (1992) Inverse Acoustic and Electromagnetic Scattering Theory. Springer-Verlag, New York. http://dx.doi.org/10.1007/978-3-662-02835-3

Call for Papers

Journal of Modern Physics

ISSN Print: 2153-1196 ISSN Online: 2153-120X
http://www.scirp.org/journal/jmp

Journal of Modern Physics **(JMP)** is an international journal dedicated to the latest advancement of modern physics. The goal of this journal is to provide a platform for scientists and academicians all over the world to promote, share, and discuss various new issues and developments in different areas of modern physics.

Editor-in-Chief

Prof. Yang-Hui He City University, UK

Executive Editor-in-Chief

Prof. Marko Markov Research International, Buffalo Office, USA

Subject Coverage

Journal of Modern Physics publishes original papers including but not limited to the following fields:

Biophysics and Medical Physics
Complex Systems Physics
Computational Physics
Condensed Matter Physics
Cosmology and Early Universe
Earth and Planetary Sciences
General Relativity
High Energy Astrophysics
High Energy/Accelerator Physics
Instrumentation and Measurement
Interdisciplinary Physics
Materials Sciences and Technology
Mathematical Physics
Mechanical Response of Solids and Structures
New Materials: Micro and Nano-Mechanics and Homogeneization
Non-Equilibrium Thermodynamics and Statistical Mechanics
Nuclear Science and Engineering
Optics
Physics of Nanostructures
Plasma Physics
Quantum Mechanical Developments
Quantum Theory
Relativistic Astrophysics
String Theory
Superconducting Physics
Theoretical High Energy Physics
Thermology

We are also interested in: 1) Short Reports—2-5 page papers where an author can either present an idea with theoretical background but has not yet completed the research needed for a complete paper or preliminary data; 2) Book Reviews—Comments and critiques.

Notes for Intending Authors

Submitted papers should not have been previously published nor be currently under consideration for publication elsewhere. Paper submission will be handled electronically through the website. All papers are refereed through a peer review process. For more details about the submissions, please access the website.

Website and E-Mail

http://www.scirp.org/journal/jmp **E-mail: jmp@scirp.org**

What is SCIRP?

Scientific Research Publishing (SCIRP) is one of the largest Open Access journal publishers. It is currently publishing more than 200 open access, online, peer-reviewed journals covering a wide range of academic disciplines. SCIRP serves the worldwide academic communities and contributes to the progress and application of science with its publication.

What is Open Access?

All original research papers published by SCIRP are made freely and permanently accessible online immediately upon publication. To be able to provide open access journals, SCIRP defrays operation costs from authors and subscription charges only for its printed version. Open access publishing allows an immediate, worldwide, barrier-free, open access to the full text of research papers, which is in the best interests of the scientific community.

- High visibility for maximum global exposure with open access publishing model
- Rigorous peer review of research papers
- Prompt faster publication with less cost
- Guaranteed targeted, multidisciplinary audience

Scientific Research

Website: http://www.scirp.org

Subscription: sub@scirp.org

Advertisement: service@scirp.org